STRESS-DIFFUSION INTERACTION DURING OXIDE SCALE GROWTH ON METALLIC ALLOYS

A Dissertation
Presented to
The Academic Faculty

by

Honggang Zhou

In Partial Fulfillment
of the Requirements for the Degree
Doctor of Philosophy in the
School of Mechanical Engineering

Georgia Institute of Technology
August 2010

STRESS-DIFFUSION INTERACTION DURING OXIDE SCALE GROWTH ON METALLIC ALLOYS

Approved by:

Dr. Mohammed Cherkaoui, Co-Advisor
School of Mechanical Engineering
Georgia Institute of Technology

Dr. Jianmin Qu, Co-Advisor
School of Mechanical Engineering
Georgia Institute of Technology

Dr. Ting Zhu
School of Mechanical Engineering
Georgia Institute of Technology

Dr. Thomas H. Sanders, Jr.
School of Material Science and Engineering
Georgia Institute of Technology

Dr. Esteban P. Busso
Centre des Materiaux
Mines ParisTech

Date Approved: May 14, 2010

ACKNOWLEDGEMENTS

For this dissertation to see the light there are many people who have contributed generously and affectionately. I am indebted to Dr. Mohammed Cherkaoui, my advisor, and the chairman of my dissertation committee. His diligence, friendship and support as a mentor have been invaluable. I deeply appreciate the freedom he has allowed me to define my own topic and sharing his knowledge in research. I am also grateful to Dr. Jianmin Qu, my co-advisor, and the co-chair of my dissertation committee, for being a good critic of my thoughts and approaches. I really thank him for his guidance.

Many thanks also go to the members of my reading committee, Dr. Esteban P. Busso, Dr. Thomas H. Sanders, Jr., and Dr. Ting Zhu for reading the draft and providing advice for the completeness of this dissertation.

I am also thankful to all my friends. In particular, I would like to thank Dr. Narasimhan Swaminathan for his help on the development of FORTRAN UEL code and shearing with me many literatures. I am also grateful to Mr. Yuan Zhong for useful discussion on topics of Fracture Mechanics and Plasticity. I would also like to thank my office mates and colleagues, Mr. Ryan Austin, Dr. Laurent Capolungo, Mr. Yifan Gao, Mr. Shan Huang, Dr. Janine Johnson, Mr. Jason Mayeur, Mr. Jin Song for their friendships and supports.

Lastly, I like to thank my parents, Mr. Shouhe Zhou and Mrs. Shuyun Ding, and my fiancée, Ms. Yu Cao for their constant moral support, their love and understanding. For them, the whole endeavor becomes less arduous and more worthwhile.

TABLE OF CONTENTS

LIST OF TABLES

LIST OF FIGURES

SUMMARY

When a metallic alloy is placed in an oxygen environment, oxide scale may be formed on the metal surface. The continuous growth of such oxide scale is enabled by the diffusion of various ionic species in the scale layer primarily driven by the gradient of chemical potentials of these ionic species. In addition, the molar volume of oxide is typically greater than that of the base metal. Consequently, mechanical stresses are generated in the oxide scale. Such mechanical stress, in return, may affect the diffusion of ionic species resulting in different oxide growth kinetics. Such interaction between ionic diffusion and mechanical stresses and its effect on oxide scale growth have not been studied.

The goal of this thesis is to develop a systematic model for oxide scale growth that takes into account the diffusion-stress interaction. To achieve this goal, the coupled equations based on continuum formulas for diffusion and stresses are developed in first part of this study. The chemical potentials are defined as a stress dependent function. The variation of stress can therefore change the diffusion force, which is the gradient of chemical potentials, to affect the ionic species distribution and consequently have effects on the oxidation kinetics. The model is used to investigate several important aspects of oxidation including scale growth kinetics, stress distribution in the oxide scale, void formation near the metal/oxide interface, and initiation of oxide scale spallation.

The reactive element effect (REE) during oxidation of reactive element doped alloy is extensively studied in this study using the developed stress-diffusion interaction

model. The key information, such as the modification effects of reactive element upon the diffusion properties of ionic species in oxide scale are quantitatively accessed for yttrium doped Cr alloy. Finite element method was used through a User Element subroutine for ABAQUS to solve the fully coupled stress-diffusion equations in 2D domains with accounting for both elastic and inelastic deformations. The REEs are comprehensively investigated by studying the effects of yttrium on interfacial delamination driving force, energy release rate (G), oxide-alloy interface morphology, and defect diffusion.

The outcomes of this study give (1) a deeper understanding of how stresses affect the oxidation, (2) a model to simulate oxide scale growth, and (3) design guidelines on rare earth element doping for improving oxidation resistance. The results of this work elucidate the impact and importance of stress-diffusion coupling on oxidation kinetics and mechanical reliability.

CHAPTER 1 INTRODUCTION

1.1 Background

Metallic alloys have been widely used in engineering areas due to their properties of high mechanical strength, good thermal and electrical conductivity, as well as relatively low cost. For example, the use of metallic interconnects instead of ceramic interconnects has became a general trend in solid oxide fuel cells. However, when alloys serve in high-temperature and high-oxygen-partial-pressure environments oxide scale formation on such alloys is common. Huge stresses can be generated during oxide growth and can become the driving force for delamination of the less-dense oxide from the surface of the alloys. Cyclic spallation and healing of the oxide scale will severely contaminate the alloys. First, cyclic generation of oxide partially consumes the alloys and hence constantly reduces the volume or crossection areas of the alloy components. Besides, spallation of oxide scale will induce potential defects in the alloys and the extension of these defects could severely affect the reliability of these alloys.

Because of these problems, alloy oxidation of alloy has drawn tremendous attentions in the past decades. Topics such as restraining oxidation and protecting oxide scale from spallation are still active research areas. Intensive studies on alloy oxidation have been undertaken by various researchers in the past several decades. It is well understood that the growth of the oxide is due to the formation of oxide inside or on the surface of the scale. This growth is believed to be controlled by the coupling

of species diffusion and the stress field accompanying the formation of the oxide. However, although numerous papers have been published upon experimental and theoretical studies of oxidation, few models considering stress dependence have been proposed to date. The motivation of this research is to gain deeper understanding of the stress-diffusion coupling mechanism during alloy oxidation and its significant effects on oxidation kinetics. The primary object will be realized by proposing a model capable of depicting the stress field in oxide scale as well as its impact on scale growth.

1.2 Research Objectives

In this study, we will focus on the stress-diffusion interaction during the oxidation progress of metallic alloys and we will develop a thorough understanding of the oxidation mechanism behind the phenomenon. The expected outcomes of this study include (1) a model to simulate oxide scale growth with deeper understanding of how stresses affect oxidation, (2) design guidelines on reactive element doping for improving oxidation resistance, and (3) analyses of the reliability behavior of oxide-alloy interfaces with pre-existing defects.

The first objective is to investigate the mechanism of stress-diffusion interactions during the oxidation of alloys. There is general agreement that the stresses are generated due to the diffusion-controlled oxide growth; and stresses, either from self expansion or externally origins, will change the diffusion driving forces. However, there is less deep understanding of the characteristics of the mutual

interaction between the stresses and the diffusion of species. There has not been a model to describe this two way coupling phenomenon, nor are there any quantitative explanations of how this coupling affects the oxidation kinetics as well as the delamination between oxide and alloy. This study is conducted to understand and solve these problems at a quantitative level.

This study starts with the investigation of the stress dependence of ionic chemical potentials. A general model is developed to predict the oxidation kinetics of an alloy by considering of two-way coupling between stress and diffusion. Then the model is implemented to study a one–dimensional case for validation, and a two-dimensional implementation of this model is carried out to study the alloy depletion at the oxide-alloy interface and the initiation of interfacial voids.

The second objective is to understand the so-called reactive element effect (REE), i.e. to understand the role that reactive elements perform in improving oxidation resistance. Many experimental results [1-5] have pointed out that the REE is due to the blocking effect that reactive elements create at oxide grain boundaries. However, their conclusions are only based on the phenomena and speculations from the corresponding cases. Limited modeling studies have related the REE to certain material properties from experimental measurements, such as ionic diffusivities. However, there has not been a quantitative evaluation of the REE on oxidation kinetics by modeling the relation between kinetics and the content of reactive elements in alloys. In this study, the quantitative relation between the diffusivities of ions and the activities of the reactive element (yttrium) has been derived for the first

time and has been incorporated with the previously derived thermodynamic model accounting for the stress-diffusion interaction in the oxidation of alloys. Quantitative analyses of the role of REE on the decrease of the interfacial spallation driving force, as well as the increase of the interfacial adherence are conducted.

Last but not least, the third objective of this study is to comprehensively understand the impact REE on oxidation kinetics and the reliability of oxide-alloy interfaces. Two-dimensional simulations are performed for two kinds of examples: a case with a pre-existing interfacial crack and a comprehensive case with various effects observed. In limited cases of study on oxidation of alloys [1-3], the behavior of alloys is assumed to be elastic. However, at high temperature alloys have more or less shown inelastic behaviors, especially when the alloy sustains a high level of stresses. A deformation plasticity constitutive relation is adopted in the pre-existing interfacial crack case to account for alloy plasticity. The size-effect uses a homogenized continuum model to represent the polycrystalline oxide in order to study the size effect of the oxide grain on oxidation kinetics as well as the interfacial adherence between alloy and oxide. In this study the interfacial delamination driving forces are evaluated for both cases.

1.3 Organization of this Dissertation

This thesis is organized into six chapters.

Chapter 1 first gives background information related to this study, then the objectives of this study and the organization of this dissertation are also presented.

In chapter 2, we review the relevant studies that have been published before or recently on high temperature oxidation of alloys. Topics covered include the stress-diffusion interaction, modeling work of alloy oxidation, oxidation of Fe-Cr alloys, the reactive element effect (REE) on alloy oxidation, interfacial fracture during oxidation, as well as the creep of alloy during oxidation.

The majority of this dissertation is from chapter 3 to chapter 5. These can be divided into two parts. The first part is chapter 3, which involves the understanding of oxidation mechanism and failure mechanism. The second part includes chapters 4 and 5, which describes the role of REE on material performance improvement.

In chapter 3, a stress-diffusion interaction model is established for the oxidation process of binary alloys. The interfacial failure mechanisms of scale on alloy are also investigated.

In chapter 4, the reactive element effect (REE) on the modification of cation diffusivity in oxide scale is modeled. The consequent improvement of the interfacial resistance of the material is illustrated in this chapter.

In chapter 5, the stress-diffusion interaction model is extended to include the inelastic deformation of the substrate alloy. This model is implemented first to study the propagation driving force of an interfacial crack along the oxide-alloy interface after steady state has been reached when the alloy experiences deformation plasticity. It is then used to study the creep effect on the overall kinetics and mechanical performance of the material during the oxidation process. In both of these studies, the

reactive element effects are intensively studied.

In chapter 6, the dissertation is summarized and highlighted. Further work related to the study is also proposed.

CHAPTER 2 LITERATURE REVIEW

2.1 A Brief Overview of High Temperature Corrosion of Alloys

As the science and technology of establishing the constituent components and structure for functional performance, the design and processing of alloy materials has been used to supply innovative materials for the engineering requirements. One of the important categories of engineering alloys is designed to supply mechanical strengths in high temperature environments.

The needed properties may vary based on different application environments. For example, gas turbines require materials to provide operating efficiency, durability and increasing thrust; on the other hand, the alloy interconnects for solid oxide fuel cells provide not only good mechanical properties as the cell stack, but they also provide high electronic conductivity for current collecting as well as thermal stability. Of all of these properties, corrosion resistance is the most fundamental and important property in alloys. The performance standard of high temperature alloys in long time service is usually based on the corrosion resistance of the alloy and the interaction between corrosion and mechanical properties of alloys. Studies have been intensively conducted on the oxidation behaviors in relevant environments to reach a quantitative understanding of the corrosion behavior for reliable design. More and more material behaviors, such as creep behavior of alloy, have been involved in the comprehensive understanding of high temperature corrosion in alloys.

2.2 Introduction to the Stress-Diffusion Interaction

2.2.1 Diffusion Controlled Oxide Formation

At high temperature, oxide scale is semiconductor depends on the oxygen partial pressure. Young et al. [4] studied Cr_2O_3 produced at different pressures in the atmospheres in the temperature range from 1000 to 1800 K. At low oxygen partial pressures n-type semiconductor behavior is observed, while the material is p-type semiconductor at high oxygen partial pressures. At most working conditions, high oxygen partial pressure is expected. In this p-type semiconductor case, it is believed that the rate of oxidation is controlled by the ionic conductivity.

Generally, the continuous growth of an oxide scale is enabled by the transport of various ionic species in the scale layer. A generally schematic illustration of the usual mechanism for diffusion in a growing scale is shown in figure 2.1. The growth of NiO films by thermal oxidation of Ni [5] can be considered as a typical example. For Cr_2O_3, The situation is less obvious than for NiO, though the growth mechanisms are identical. The reason is that chromia is a barrier to the outward diffusion of species in these alloys.

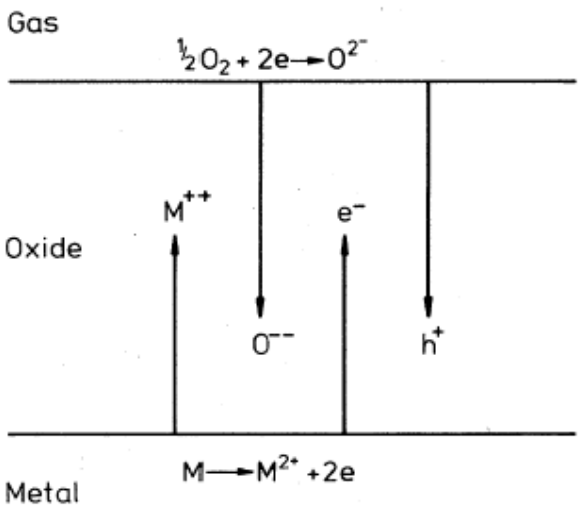

Figure 2.1 General schematic illustration of the usual mechanism for diffusion

Reproduced from Atkinson, 1985 [6]

It has been appreciated that although a film may be mainly growing by the outward transport of cations, there will be a small contribution from oxygen moving inwards. For example, Tsai's work [7], established that chromia scale growth occurs through oxygen/chromium counter diffusion. Rhines and Wolf [8] also propose that the metal-oxygen counterflow would give rise to oxide growth. The position of the oxidation generation provides further evidence of the diffusion controlled oxidation. For example, oxygen diffusion was slower than chromium diffusion by about 3 orders of magnitude [9], as a consequence of this difference, most of the chromium oxide formation within the oxide scale is near the oxide/gas interface.

2.2.2 Stresses in Oxide Scale

High-temperature oxidation of metals and alloys always involves the development of mechanical stresses. These stresses have important effects on oxidation, particularly on oxidation kinetics, species diffusion rate, even scale spallation or detachment. Several sources of stress need to be considered in the scale.

Thermal stresses are induced by changes in environmental temperature and differences in the thermal expansion coefficients of the scale and the substrate. Thermal expansion mismatch is often reported as the main origin for stresses in the scales observed at room temperature. Stress measurements on NiCr alloy oxidized in air at $800\,^{o}C$ [10] and $900\,^{o}C$ [11] reported residual high compressive stress at room temperature, ranging from 1.5 to 3 GPa. Huntz [11-12] performed oxidation of Ni based alloys at $900\,^{o}C$ and obtained consistent results on the thermal stresses in the oxide scale. Mougin et al. [13] derived a thermal expansion coefficient of $10.75\times10^{-6}K^{-1}$ for a 1.5 μm-thick chromia scale by using an in-situ measurement technique at $750\,^{o}C$. Though this value is larger than values generally reported (in the range of 5.7-9.6 $\times10^{-6}K^{-1}$), it provides evidence that the thermal stresses caused by mismatch of thermal expansion coefficients are considerable.

Stresses may also result from oxidation production and scale growth. Lateral compressive growth strain has been reported by many recent studies [13-15]. Other than obtaining the thermal expansion coefficients of chromia scale, Mougin et al. [13] has also identified compressive growth stresses in the chromia scale after 2000 minutes of oxidation. The compressive stress was observed reaching nearly 2GPa

which is ten times greater than the measured thermal stresses. The internal oxide formation was believed to lead to this significant compressive stress. Oxidation compressive growth strain has also been found in oxidation of other frequently used alloys, such as aluminum alloys. Tolpygo et al. [15] investigated the formation of alumina at high temperature. The results showed that lateral growth strain depended on time/scale thickness. Further conclusions that the lateral growth strain was determined by oxygen and aluminum ions supplied by diffusion and available for the reaction within the scale had also been derived based on experiments.

Additionally, the oxide scales are subjected to stresses induced by other external mechanical loads. Among these three sources of in-scale stresses, stresses during oxidation have recently drawn the most concern, especially those stresses developed under isothermal oxidation. Although limited progress has been achieved in modeling this stress system, many observations and discussions have been undertaken. Publications have provided some information about the mechanisms of intrinsic growth stress up to several decades ago [16]. Some consensus has been reached concerning the origins of the residual stresses in metal (alloy)-oxide systems, which include epitaxy relationships between the metal substrate and oxide scale [17], the Pilling and Bedworth ratio (PBR) of conversion from metal into scale [18-19], oxygen incorporation in the substrate or the reaction composition of oxygen and metal, and the influence of vacancies generated during oxidation and compositional changes in scale.

Epitaxial relationships depend on the differences between an oxide scale and

its substrate lattices. So-called epitaxial stresses will be induced when these difference exist. They are either compressive or tensile according to the epitaxy relationships. The epitaxial stresses are only important for thin films in which stresses reach their maximum at the scale/substrate interface and decrease to their minimum at the surface of the scale.

The Pilling and Bedworth Ratio [18-19] (PBR, the ratio of the oxide molar volume to that of the metal which gives the oxide) is commonly considered to be responsible for the generation of stresses during scale growth. The expression of PBR is usually in the form of

$$\text{PBR} = \frac{V_{ox}}{V_m}, \tag{2.1}$$

where V_{ox} is the molar volume of oxide, and V_m is the molar volume of substrate metal atom. In case of isotropic materials, the volumetric deformation defined by PBR is [12]

$$\varepsilon_v = \left[\left(\text{PBR} \right)^{1/3} - 1 \right]. \tag{2.2}$$

When the PBR is not unity, for example when it is, greater than 1, stresses would be expected at some constraint places in the oxide scale as well as those in the substrate, e.g. compressive stresses at those parts in the scale close to the scale/substrate interface, and tensile stresses at places in the substrate close to the interface. Huntz [12] emphasized that PBR is an important origin of stresses in scale growth by preferential anionic diffusion. At the scale/gas surface, due to the absence of geometrical effects, such stresses may not be critical, while at the scale/metal interface the stresses may be quite large [6]. According to Table 2.1, the PBR of Cr_2O_3

is larger than unity. Therefore, compressive stresses are expected in chromia.

Table 2.1 Physical parameter characterizing Cr_2O_3 forming system.

Scale	PBR	E_m (GPa)	E_{ox} (GPa)	v_m	v_{ox}
Cr_2O_3	2.07 [12]	268 [20] 279 [21]	335 [12]	0.333 [21]	0.262 [12]

Some experimental [22] results exhibit that during the growth of Cr_2O_3 scale, the stresses that are generated are mostly tensile rather than compressive. This result indicates that PBR may not be the critical parameter responsible for the growth of stress. However, most experimental results show that outward cation diffusion is the dominant diffusion in chromia scale. Therefore, at the outermost part of the scale there may be tensile stresses, but at least in the innermost part, the part closest to the scale/metal interface, compressive stresses must be found.

This mechanism is still under exploration according to some recent studies [23-24] on chromia which indicate that the predominant transport process is still ambiguous. Based on these results, the diffusion coefficient of anions (oxygen ion) and cations (chromium ion) are of the same order. Another result, reported by Sabioni et al. [25] exhibits that the diffusion of oxygen is even faster than that of metal ions. Oxygen incorporation in substrate or reaction composition of oxygen and metal also introduces stresses in the scale. Internal oxidation usually occurs at grain boundaries

and induces mostly compressive stress at the scale/substrate interface. This is basically the mechanism of predominant anionic diffusion during oxidation. For cationic diffusion, this mechanism also can be used to account for stress growth after the steady state of cationic diffusion has been reached. Experimental results only demonstrate the stress growth cases for the anionic diffusion mechanism. Bull [3] performed an oxidation experiment on a Y-doped FeCrAl alloy at 1000 ^{o}C. The anionic diffusion dominates in the oxide scale. A stress of magnitude 1.75 GPa is reported after the first few hours' oxidation.

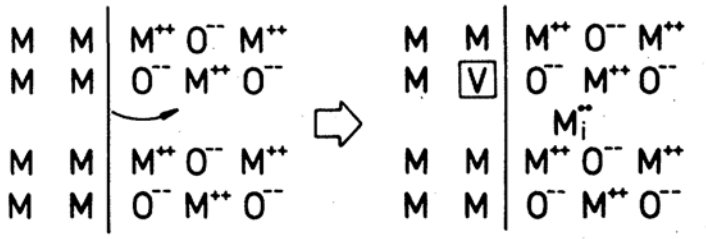

(a) Vacancy generation at scale/metal interface

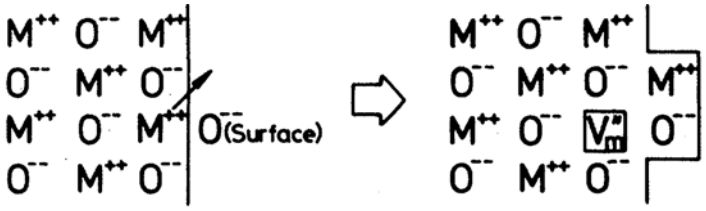

(b) Vacancy generation at scale/gas surface

Figure 2.2 An illustration of the possible reaction for vacancy generation during oxidation a) the generation of a vacancy at scale/metal interface, b) the generation of a vacancy at scale/gas surface reproduced from Atkinson, 1985 [6]

Other than anionic inward diffusion, there have been various proposals

regarding the influence of vacancies on stress generation. Vacancies may be generated at the scale/gas surface and scale/metal interface during oxidation. For cationic diffusion of predominant oxidation, a schematic illustration (Figure 2.2) of vacancy generation during oxidation was proposed by Atkinson [6]. Evidence [26] demonstrated that vacancies were generated at the metal/oxide interface during high temperature oxidation of Fe-Cr alloys. From vacancy-dislocation interactions, it would be necessary to obtain appreciable strains [27]. Under most circumstances, the vacancies accumulate at the scale/metal interface and may nucleate as voids. In some cases, the vacancies will migrate into the metal substrate due to the jump of metal atoms. These parts of vacancies may precipitate as voids at the metal grain boundaries [28]. It has been suggested that such vacancies' generation/annihilation mechanism is the origin of the creep processes in the oxide/metal system [29] that relieve growth stresses a few hours after the oxidation has started [3].

Compositional changes in the scale have also been considered as a source of stress. Yearian et al. [30] have shown that a change from a $(Cr, Fe)_2O_3$ structure to an $(Fe,Cr)_3O_4$ stucture would certainly entail a volume expansion with an associated compressive stress.

2.2.3 Stress Dependent Ionic Diffusion

From the previous two sections, two important factors in the oxidation process can be summarized: 1) the oxide scale is always subjected to various stresses, such as oxidation induced stress, as its thickness increases; 2) the oxidation kinetics

depends on the ionic diffusion inside the scale; any variation in the diffusion will change the rate and position of the scale growth. It is obvious that those two factors are not independent of each other. For example, as the result of ionic diffusion increasing, fast accumulation of oxide scale will induce bigger oxide deformations and hence possibly generate stresses, and studies [7, 16, 19, 23-24, 31] have provided evidence about this one way dependence. On the other hand, the reverse dependence, the impact of stresses on diffusion and oxidation kinetics, has been theoretically studied since the 1970's [32-33]. Though limited, stress dependence of diffusion has also been observed. When the oxide of Al film forms a strong, dense layer with compressive stress, this oxide layer serves effectively as a passivation layer to inhibit the grain boundary diffusion of ions [34-35]. On the contrary, when the stresses relax almost completely large diffusion flow occurs.

It is believed that the driving forces of ionic species diffusion in oxide scale are the gradients of chemical potential. In a previous study of ionic diffusion in solid electronic conductors [36], the electrochemical potential has been modified to account for the effect of mechanical field quantities on electrochemical fields. Similarly, modification of the chemical potential can be exploited to solve for stress dependent diffusion.

2.3 Modeling Work of Alloy Oxidation

2.3.1 Modeling of Diffusion and Estimation of Effective Diffusivity in Polycrystalline Solids

The modeling of diffusion in polycrystalline solids such as polycrystalline oxides mostly falls in to two parts based on the diffusion mechanism: diffusion inside the grains and diffusion along the grain boundaries. Species transport at the grain boundary due to thermodynamic origins is much faster than that inside the bulk. For example, in chromia (Cr_2O_3) [7] the difference between respective diffusivities is several orders of magnitude at the oxidation conditions. Some researchers model the grain boundary and bulk as separate diffusion paths. In their modeling of polycrystalline oxidation, Krishnamurthy and Srolovitz [37] governed the transport of ions in grain boundary and bulk using two separate diffusion equations with consideration of different diffusivities and geometric diffusion paths. Beyond their work, the diffusion in bulk vanishes in [2] where only the grain boundary contribution to ion transport is considered to govern the diffusion.

Some other researchers focus on the geometric study of polycrystalline solids to obtain an effective diffusivity over the whole of a solid under some homogeneous rules. An early model for diffusion through a crystalline structure was established by Fisher, who considered a semi-infinite solid with a single fast diffusing grain boundary embedded in a bulk of much lower diffusivity [38]. Many subsequent studies [39-40] examined the same basic geometry with less restrictive boundary conditions. The simplest geometry for polycrystalline diffusion that can be captured is

a system of parallel grain boundaries, such as a columnar structure. This geometry was adopted in many studies [41-43] that focus on diffusion through polycrystalline films, and it has been concluded that a bulk containing parallel grain boundaries behaves like a homogeneous diffusing system with an effective diffusivity D_{eff} .

More recently, with the rapid evolving of computer technology, many simulation methodologies have been employed in the study of oxide grain boundaries, e.g. molecular dynamics [44], Monte Carlo method [45] and ab initio calculation [46]. The molecular dynamics (MD) technique follows the laws of classical mechanics, and most notably Newton's second law. It thus tracks actual forces on the atoms as well as their trajectories while they migrate. The diffusion coefficient along the grain boundaries can be determined by averaging the trajectories generated as the defects migrate in the simulation. One very important advantage of this technique is that the atoms in the simulation will move in ways close to what the atoms would follow in real substances. Therefore, the results of a simulation would probably demonstrate the relevant diffusion mechanisms.

Suzuki and Minshin [47] present the methodology for diffusivity in a grain boundary at low temperature (less than 1000 degrees C): The multi-body potentials describing the interatomic interaction, such as Born-Mayer-Huggins (BMH) potential [48] and these based on the embedded-atom method (EAM) [49], are first constructed by fitting to both experimental and first-principles data [50-52]. Following the construction of interatomic potentials, GBs are created by standard geometric constructions and their initial state structures are determined by molecular

static calculations including both local atomic displacements and rigid translations of the grains [47]. Either a vacancy [53] or a doping ion [46] is created at various positions inside the GB, and its walk along the grain boundary is simulated by running molecular dynamics (MD). To obtain the diffusivity, a long MD simulation is carried out first to reach the defect equilibrium. Another MD run then follows, during which all defect jumps are followed and the relevant trajectory information is saved for mean square displacement (MSD) [46, 53-54] analysis.

2.3.2 Oxidation Models and Stress-Diffusion Interaction

Most models [1-2, 29, 37, 55-58] that have been proposed to date are based on experimental observations and understanding of their physical origins. Some examples include transformation strains that come from the differences in molar volume between metals and their oxides (i.e. the epitaxial relations) [8], dilatational strains induced by metal self-diffusion atomic flux [29] driven by gradients of the chemical potentials of the alloy, chemical strains of non-stoichiometric origin caused by the oxygen insertion in the metal lattice [2], etc.

In the work of Clarke [55], the lateral strain of oxide scale is considered to be induced by the climbing edge dislocation, with Burgers vector components parallel to the oxide/alloy interface. Substantively, this is equivalent to the assumption that oxide scale grows under concurrent inward oxygen and outward cation diffusions along grain boundaries, since the cations and anions are trapped at the core of the dislocations and diffuse as the dislocation climbs. In this model, lateral growth of the

oxide is constrained by the underlying alloy such that a growth stress is generated. One problem with this model is its assumption that only a negligible portion of the ions that diffuse across the scale contribute to the lateral growth strain. This will exclude the stress-diffusion coupling and therefore result predictions can not be accurate. Other than Clarke's model, a stress growth mechanism based upon annihilation of cation vacancies at the scale/metal interface and the accompanying climb of interface misfit dislocations into the metal has been proposed by Pieraggi and Papp [17]. This mechanism predicts the development of compressive stresses in the oxide at the scale/metal interface.

The mechanism of inward oxygen diffusion through a grain boundary and the resultant oxide formation along the grain boundary is applied in the model of Limarga et al. [2]. In a steady-state configuration, the average growth stress is analyzed under two scenarios: Linear stress distribution and uniform stress along the vertical oxide grain boundary. Though the origin of the stress is not specified, this study introduced the stress dependence to the chemical potential of species *s* (*s* represents the specified species, e.g. oxygen) by an empirical relation from [59-60],

$$\mu_s(z) = X_o(z)\exp\left[\frac{\sigma_b(z)V_p}{kT}\right], \tag{2.3}$$

where X_o is the oxygen vacancy concentration, z is the distance from the free surface, σ_b is the compressive stress in the grain boundary, V_p, k and T are the molar volume of the oxide, Boltzmann's constant, and temperature, respectively.

Recent models [2, 37, 55] are more or less based on the Rhines and Wolf model [8], which states that new oxide formation along grain boundaries lying

perpendicular to the alloy/scale interface is a main source of lateral strain. In order for this theory to be consistent, the main hypothesis used is that the oxide scale is thin compared to the metallic substrate, and the scale adheres to the substrate. Thus the oxide is constrained against lateral expansion, which in turn provides a source of intrinsic growth stress. For simplicity in modeling polycrystalline diffusion as well as scale growth, the models assume that a single grain traverses the oxide film, so that grain boundaries are constituted parallel to each other and perpendicular to both interfaces (scale/alloy interface and scale/gas interface) of the scale. A more general model describing the stress distribution in growing polycrystalline oxide films is presented by Krishnamurthy and Srolovitz [37]. The idea of Rhines and Wolf is followed in their study. The grain boundaries serve both as a high diffusivity area and as an oxide growth site. The distribution of Cauchy form oxide stresses, coupled with diffusion of species within the oxide scale, is described

As in all models encountered so far, oxidation is more or less controlled by ionic diffusion across the oxide scale through various mechanisms. Though in some studies the diffusion is thought to be unaffected by the stresses, the importance of the stress-diffusion interaction in modeling the oxidation process has been gradually appreciated by the researchers. The chemical potentials of the mobile components (atoms or ions) in solids were first applied for driven force (gradients of chemical potentials) of diffusion in an inhomogenously stressed solid by Li et al. [61]. The concept of chemical potential, which is also named after diffusion potential [62], was established on a thermodynamic point of view in [32]. Based on Moutier’s theorem

[63], the chemical potential depends on stresses as well as their impacts on the migration barrier for the mobility of drifting components. For example, when new oxide is generated in the oxide grain boundary, the migration volume is associated with the oxide volumetric strains; therefore, the diffusion is correspondingly associated with the elastic energy. The relations between chemical potential, stress, strain, etc. are given as a Maxwell's type expression from [33]. For an oxide scale with a compound in the form of MO, the stress dependent diffusion potential for the ions in the lattices can be given as,

$$\mu_s\left(c_s,\sigma\right)=\mu_s\left(c_s,0\right)-V^m\eta_{ij}^s\sigma_{ij}-\frac{V^m}{2}s_{ijkl}^s\sigma_{kl}\sigma_{ij} \tag{2.4}$$

where,

$\mu_s\left(c_s,0\right)$ is the stress independent chemical potential,

V^m is the molar volume of the oxide at natural state,

σ_{ij} is the Cauchy stress tensor,

$\eta_{ij}=\partial\varepsilon_{ij}^s/\partial c_s$ are the coefficients of chemical expansion,

ε_{ij}^s are the strains due to compositional change of defect species *s*,

$s_{ijkl}^s=\partial S_{ijkl}/\partial c_s$ is the change in elastic compliance due to change in concentration of the defect species,

S_{ijkl} is the elastic compliance of oxide scale

c_s is the mole fraction of the species *s*.

Among all the previous modeling studies, the species mass flux is related to the chemical potential through a classical phenomenological equation:

$$J_s = -\frac{D_s c_s}{RT}\nabla \mu_s \tag{2.5}$$

where D_s is the diffusivity of species *s* in the oxide and *R* is the universal gas constant. In the proposed research the diffusion potential in equation (2.4) is only a special case of the more general diffusion potential that is derived in this study based on continuum thermodynamics. The motivation behind the development of an alternative stress dependent diffusion potential is that, the Eshelby stress tensor should appear as the elastic contribution to the driving force for diffusion [64] and not the Cauchy stress. Only under conditions of self-stressed diffusion, where non-stoichiometry is the only source of stress, can equation (2.4) apply.

2.4 Oxidation of Fe-Cr Alloys

Chromium-based alloys are attractive with stable oxides, but are relatively costly to fabricate. Compared to chromium-based alloys, iron-based alloys have advantages in terms of high ductility, good workability and low cost [65]. By far, iron-based alloys, especially Fe-Cr based alloy, e.g. Crofer 22 APU, are the most attractive metallic interconnect material for SOFCs. Due to the aforementioned advantages, Fe-Cr alloys may be very good candidates for metallic interconnects. To give a better understanding of the oxidation performance and oxide scale growth mechanism, some Fe-Cr oxidation related issues are presented in the following part.

The oxidation kinetics and the morphology of the scales generated during oxidation of Fe-Cr alloys have been the subject of numerous papers. Reviews with considerable details are given by Wood and his colleagues [66-67]. For alloys

containing less than 13% Cr under oxidation conditions of 1000 °C, out layers of Fe_2O_3 and Fe_3O_4 and a inner iron-Cr-O compound approximately in the form of $Fe_{(2-x)}Cr_xO_4$ were observed [68]. Lai et al. [69] showed that if the chromium concentration in the alloy is very low, FeO doped with chromium is the stable oxide phase in contact with the alloy instead of the iron-chromium spinel.

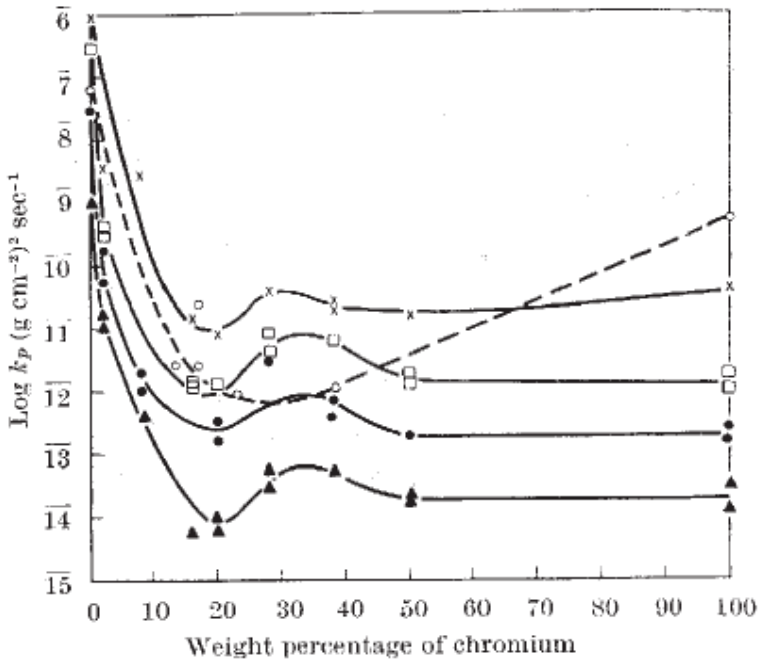

Figure 2.3 "Parabolic rate constants for oxidation of iron-chromium alloys, ×, 950 ºC; □, 850 ºC, ●, 750 ºC, ▲, 650 ºC, ○, 900 ºC " Reproduced from Footner et al., 2004 [70]

When the chromium contents are in the range of 14-20%, very complex scale formations are observed [30, 71]. Instead of a monolayer of stable Cr_2O_3, the chromia layer first forms along with iron-rich oxides overlaid with the metal. As the chromium component in the alloy is depleted right at the interface between the scale and

substrate, the stratified scale shows a structure similar to that in the oxidation of lower chromium component alloy (below 13 wt %). A change in kinetics from parabolic growth rate to linear rate is observed associated with this process.

To form a stable oxide layer to establish reasonable resistance to hot corrosion, an optimum critical weight percent of chromium in alloys is needed. In a recent review paper of Yang et al. [72], this value is evaluated as 18-19 wt %. This conclusion was justified by Footner et al. [70]. In their work, the kinetics of oxidation of Fe-Cr alloys with Cr content in the principal range of 0-50% is examined. Some of their results are shown in figure 2.3, from which, it is clear that the minimum oxidation rate at each temperature locates at about 18-20 wt % Cr. It also can be seen that the initial addition of chromium to iron results in a large decrease in the rate of reaction. This change is due to the elimination of iron oxide in the scale and the appearance of higher density chromia. At higher weight percent, e.g. 20-25% [26], on all Fe-Cr alloys a protective, continuous chromic oxide scale forms. After that, an interesting phenomenon can be observed that the reaction rate increases with the chromium content until reaching a maximum at about 30 wt % Cr. With the use of a scanning electron microscope, Howes [26] verified that the outward diffusion of chromium is involved in the oxidation mechanism for high chromium content alloys.

2.5 Reactive Element Effect (REE) on Alloy Oxidation

Since the 1940s, people have found that the addition of thin layers of surface dopants or coatings of reactive elements such as yttrium [73-74], ruthenium [75],

neodymium [76-77], praseodymium [77], lithium [78], erbium [79] can change the growth mechanism of the oxide scale, effectively improving the adhesion of oxide and decreasing the rate of growth. Polman et al.[80] summarized the beneficial effect of reactive element as: (1) The amount of chromium, necessary to form a continuous chromia layer, can be reduced (2) the overall oxidation rate is decreased (3) the oxide scale is more adherent and less oxide spallation occurs.

Thinner and denser oxide scales have been observed for the reactive-element doped alloy. These differences in morphology could be explained by selective oxidation of the protective oxide forming element [77]. Some believe this is presumably because of the larger ionic radii of reactive elements, which may be mainly segregated at the grain boundary of oxide scale [72]. Advanced experimental analytical techniques such as secondary ion mass spectrometry (SIMS) expedited the process on understanding the origins of reactive element effects. It has been suggested that when a reactive element such as yttrium presents in the chromia layer [7] : (1) yttrium is segregated out of the oxide grains and stays along grain boundaries, oxide surfaces and alloy-oxide interfaces; (2) The segregated yttrium acts as a barrier at the grain boundaries such that the outward diffusion of cations is drastically suppressed. To date, only a few studies have attempted to quantitatively model reactive element effects. Based on the classic Fick's first law, Liu et al. [81] establish a 1-D model for growth of Yttrium doped $\alpha - Al_2O_3$ by relating the oxidation kinetics to inward oxygen diffusion and oxide grain coarsening. More recently, Nijdam et al. [31] proposed a 2-D model to describe the growth kinetics of protective oxide scale

containing reactive element oxide inclusions. For a given reactive element content, their model can calculate the alloy grain size, the size of reactive elements containing intermetallic precipitates in the alloy, the parabolic rate constant of the protective scale, the size and distribution of the inclusions in the scale as well as the total oxide scale kinetics.

2.6 Interfacial Fracture

Interfacial imperfections commonly exist between the oxide scales and the alloys during the oxidation process. The dissimilarity of material properties between alloys and oxides leads to complex interfacial fracture problems. To protect the oxide scale, it is pertinent to understand the mechanism of interfacial failure between such biomaterial interfaces. Unlike crack propagation in homogenous media, propagation of interfacial cracks takes place in a mixed mode which is a combination of the commonly known failure mode type I and type II.

For a plane interface crack between two different elastic isotropic materials, extending the regime of linear elastic fracture mechanics (LEFM) gives good results on failure analysis. Williams [82] was the first to perform interfacial crack analysis. An asymptotic analysis on the open-crack-tip elastic fields was carried out in that study. When the distance from the crack tip r is approaching zero, the stress singularity is of the order of r^{ξ} with $\xi = -1/2 + i\varsigma$, where $i = \sqrt{-1}$ and

$$\varsigma = \frac{1}{2\pi} \ln\left[\frac{1-\beta}{1+\beta}\right]. \tag{2.6}$$

The nondimensional Dundur's parameters [83] are defined as

$$\alpha = \frac{\mu_1\left(\kappa_2+1\right)-\mu_2\left(\kappa_1+1\right)}{\mu_1\left(\kappa_2+1\right)+\mu_2\left(\kappa_1+1\right)}$$
$$\beta = \frac{\mu_1\left(\kappa_2-1\right)-\mu_2\left(\kappa_1-1\right)}{\mu_1\left(\kappa_2+1\right)+\mu_2\left(\kappa_1+1\right)} \tag{2.7}$$

where $\mu_i\ (i=1,2)$ is the shear modulus, $\kappa_i = 3-4\nu_i$ for plane strain and $\kappa_i = \left(3-\nu_i\right)/\left(1+\nu_i\right)$ with $\nu_i\ (i=1,2)$ being the Poisson's ratio of the respective materials. The oscillatory region was estimated by Erdogan [84] who analyzed the cracks in a nonhomogenous plane and found that the region is proportional to the crack length with a ratio around the order of 10^{-6}. Rice and Sih [85] obtained a Green's function solution for a finite interfacial crack ($2a$) and gave the complex stress intensity factor as [85-86]

$$K = K_1 + iK_2 = T\left(\pi a\right)^{1/2}\left\{\left[\cos\left(\varsigma\log 2a\right)+2\varsigma\sin\left(\varsigma\log 2a\right)\right] - i\left[\sin\left(\varsigma\log 2a\right)+2\varsigma\cos\left(\varsigma\log 2a\right)\right]\right\}/\cosh\pi\varsigma \tag{2.8}$$

where T is the applied tension field. When a crack is along the interface between two materials, the stresses singular field directly ahead of the crack tip is [87-88]

$$\sigma_{22} + i\sigma_{12} = \frac{K}{\sqrt{2\pi r}} r^{i\varsigma} \tag{2.9}$$

where σ_{22} is the tensile and σ_{12} is the shear stress component.

Since the oscillation solution is derived from the extension of LEFM, it is invalid to for elastic-plastic interfacial crack situation. The work on elastic-plastic interfacial cracks was initialed by Shih and Asaro [89]. In their numerical study on cracks lying along the interface between elastic-plastic bimaterials, they found that the cracks open smoothly. This demonstrates a big difference between this study and the elastic case since the characteristic oscillation solution was not observed. A new

phase angle [89-90] is used to parameterize the elastic-plastic fields.

For a preexisting interfacial crack, an important issue is to determine its extending criteria. For elastic-plastic materials, those criteria are mostly based on change of energy. The energy release rate G [91], defined as the energy dissipation when a crack extends a unit area, is the criterion that is mostly used. For elastic-plastic materials, the energy release rate can either be estimated by the J integral [92-93], or it can simply be calculated by its definition. For elastic materials, the virtual crack closure technique (VCCT) is usually used. A detailed review of this approach can be found in [94]

2.7 Voiding and Creep Effect during Oxidation

As a consequence of high temperature oxygen attack, oxide formation and substantial void generation at oxide-alloy interface have been observed [26-27]. Selective oxidation has been addressed in various studies on mechanism of voiding at oxide-alloy interface. In the work of Kadiri et al. [95], they extended the idea of Suo [29] that the dislocation climbing compensates the Kirkendall effect. According to their works, the generation of interfacial voids is a combination of atoms' interflow and the resultant tensile stresses. On the other hand, the experimental observation of Howes [26] showed that the voids were generated as the result of metal atom depletion at the alloy grain boundaries right below to the oxide scale.

Mutual interaction between creep of materials and oxidation processes is another phenomenon that is observed in high temperature oxidizing environments.

During alloy's oxidation process, stresses of thermal and chemical origins at the GPa level have been observed in alloys and act as the driving force for creep. Most of the studies were carried out for the purposes of testing the oxidation impact on creep properties of alloys. A typical procedure is to compare the creep responses between samples in an oxidizing environment and those in a protective atmosphere. For example, Matsuda et al. [96] showed that oxide significantly reduced the creep rate of 6061 Al matrix composites. On the contrary, a different conclusion was obtained from the work of Lee [97], which states that the creep rates of Cu-Cr alloy samples exposed in air are higher than those tested in vacuum. Only a few studies have put their focus on the effects of creep on oxidation of alloys. By means of deflection tests and modeling, Huntz et al. [98] made an attempt on stress analysis during oxidation of Ni-20Cr and concluded that the initially developed in-plane stresses are reduced with increasing exposure time as a result of creep relaxation. Tolpygo and Clarke [15] studied the competition between the increase of oxidation induced stresses and creep induced stress relaxation in oxidation of Fe-Cr-Al alloy. They concluded that at the beginning of oxidation the lateral-growth strain is larger than the creep strains in either phase while at the latter stages the relaxation processes prevail leading to a gradual decrease of stresses.

CHAPTER 3 STRESS-OXIDATION INTERACTION IN SELECTIVE OXIDATION OF FE-CR ALLOY WITH ELASTIC DEFORMATION

3.1 Introduction

In this chapter, we focus on modeling a fully coupled stress-oxidation interaction. The work will follow closely the approach of Krishnamurthy and Srolovitz [37] with some notable differences. In our approach, the equations are formulated and solved in the Eulerian framework. One of the advantages of the Eulerian formulation is that it allows the oxide lattice to "flow" upward; avoiding the complexity of computing the velocities of metal-scale and scale-air interfaces and it greatly simplifies the equations and their numerical solution. Another important difference is the use of a fully coupled theory [36] relating chemical reaction and mechanical stress, namely, not only does oxidation induces stress, but in return stress also affects the rate of oxidation. Furthermore, in this fully coupled theory, not only the hydrostatic stress, but also the deviatoric stress needs to be considered. Details of these differences and their consequences will be explained later in this chapter.

To develop our model, a binary alloy (16% wt Fe-Cr) is used as a model material. It will be seen from the derivation that the general approach presented here is applicable to a wide range of alloys. Following this introduction, the second section

of this chapter presents the model of stress-oxidation interaction. Immediately after the second section, in the third section, a one-dimensional example will be given to show how the interactions affect the oxidation kinetics and the distribution of ionic species. In the last part of this chapter, the model will then be applied to a more general two-dimension implementation to study the depletion of alloy at scale-alloy interface.

3.2 Derivation of Stress-Oxidation Interaction Model

3.2.1 Model Synopsis and Assumptions Used

Consider a Fe-Cr binary alloy exposed to an oxygen gas environment (e.g., air) with a given oxygen partial pressure at high temperature. From experiments [99-100], it is reasonable to assume that at temperatures over 800^{o}C the only oxidation product forming a scale layer on the alloy surface is Cr_2O_3. Observations from experiments [99-101] give two different scale morphologies for oxidation of Fe-Cr alloys at different temperature regions. At relative low temperature (less than 500 ^{o}C) [101] a layer of Fe_2O_3 exists on the top of the oxide film. While for relatively high temperature oxidation (higher than 800 ^{o}C) [99-100], Fe_2O_3 is observed in the early scenario of oxidation, Cr_2O_3 is the only component of the oxide film at steady state. The very initial stage of the oxidation process, which includes numerous different physical and chemical processes, is extremely complicated. To date, no consistent agreement on the mechanisms of formation of the very first layer of oxide has been obtained. To avoid such complexity, in what follows we model the

oxidation process only after an infinitesimally thin scale layer had already formed. For simplicity, we assume that the initial scale layer is Cr_2O_3 with a perfect (defect free) lattice structure.

When such a metal-oxide system is further exposed to a given oxygen partial pressure at elevated temperature, a layer of atomic oxygen will be adsorbed to the scale surface [6]. According to Cabrera and Mott [102], the adsorbed oxygen layer is atomic. These oxygen atoms are then ionized by capturing the free electr ons in the scale layer. At the same time, oxidation-favored Cr atoms in the binary alloy are converted to ions at the metal/scale interface. Consequently, counter diffusion occurs, namely, both oxygen anion O'' at the gas-scale interface and the chromium cation Cr^{III} at the metal-scale interface will diffuse into the scale layer driven by electrochemical potentials across the scale layer. When two Cr^{III} meet with three O'', an oxidation reaction may take place to form a molecule of Cr_2O_3. Depending on the rates of diffusion of these reactive ions, new oxide may form near the metal-scale interface, the gas-scale interface or within the scale layer. Once formed, the Cr_2O_3 lattice is assumed to be non-diffusible, although it can be transported due to the subsequently created new Cr_2O_3 sites.

As discussed in chapter 2, the diffusion paths and the mechanism of internal oxidation in polycrystalline oxides may be rather complex, and the locations of new oxide within the existing scale layer may vary depending on the material system. Nevertheless, the effective diffusivities of the diffusing ions can be used to account for both grain boundary and lattice diffusion by assuming that the scale layer is a homogeneous continuum. Clearly, such a continuum assumption also

conveniently homogenizes the internal oxidation, namely, new Cr_2O_3 sites can be created anywhere within the oxide layer.

In the Cr_2O_3 scale, $Cr^{\cdots}$ cations diffuse much faster than Fe ions [23, 103]. Therefore, it is assumed that the diffusion of Fe in the scale layer is neglected. Furthermore, we assume that O ions do not diffuse into the metal. Therefore, in our model, the metal-scale interface is physically identified as the division of regions without Fe and without O, respectively.

At the metal-scale interface, Cr atoms in the metal alloy are striped of their electrons, and the resulting $Cr^{\cdots}$ cations jump across the metal-scale interface into the scale layer driven by the electrochemical potential. This leaves behind Cr vacancies in the metal alloy near the metal-scale interface. The higher Cr vacancy concentration near the metal-scale interface compels Cr atomic diffusion in the metal alloy toward the interface. Although the metal substrate is assumed to be infinitely thick so that the supply of Cr is infinite, from experiments [99, 101] which indicate that local (near interface on the metal side) Cr depletion occurs, we can see that the rate of converting Cr atoms into $Cr^{\cdots}$ cations is faster than that of Cr atomic diffusion in the metal alloy.

The decreasing Cr (or increasing Cr vacancy) concentration in the metal near the scale-metal interface typically generates tensile stress in the metal. In addition, internal oxidation increases the volume of the oxide scale not only in the thickness direction, but also in the plane of the scale layer. The latter induces additional stress in the scale and the metal substrate.

A key element of the current model is the stress-dependent chemical potentials for the various species involved. Such stress-dependent chemical

potentials affect the oxidation process in two aspects. First, they introduce the stress into the diffusion equations so the fluxes are stress-dependent as well. Second, they bring the stress into the total free energy of the system, which controls the rate of oxidation/reduction reaction. Without the influence of stress, the rate of chemical reaction is dictated solely by the concentrations of reactants and products only. When mechanical stress is involved, the elastic strain energy becomes a part of the total free energy. A chemical reaction can take place only if the total free energy is to be reduced. In other word, even if a chemical reaction reduces the total chemical energy, it may not take place unless the amount of reduction in chemical energy is more than the increase in mechanical (strain) energy.

Having described the basic framework of the model, we proceed to derive the appropriate governing equations and boundary/initial conditions.

3.2.2 Governing Equations

Shown in Figure 3.1 is a schematic of the metal-scale-oxygen structure, where a Cartesian spatial (Eulerian) coordinate system x_i (i = 1, 2, 3) has been introduced so that the metal-scale interface is located at $x_3 = 0$. During the entire oxidation process, this coordinate system is treated as a reference frame fixed to the metal-oxide interface. All the governing equations and boundary conditions will be presented in this Eulerian coordinate system.

When writing the field quantities related to deformation such as strain and stress, it is often convenient to introduce the Lagrangian reference frame X_i (i = 1, 2, 3). We assume that X_i coincide with x_i initially at t = 0. The two coordinates are related by

$$\mathbf{x} = \mathbf{X} + \mathbf{U}(\mathbf{X}, t) \quad \text{or} \quad \mathbf{X} = \mathbf{x} - \mathbf{U}(\mathbf{X}(\mathbf{x}), t) = \mathbf{x} - u(\mathbf{x}, t), \tag{3.1}$$

where $\mathbf{U}(\mathbf{X}, t)$ is the particle displacement of the particle $\mathbf{X}$, while $u(\mathbf{x}, t)$ can be interpreted as the displacement of the particle instantaneously located at $\mathbf{x}$.

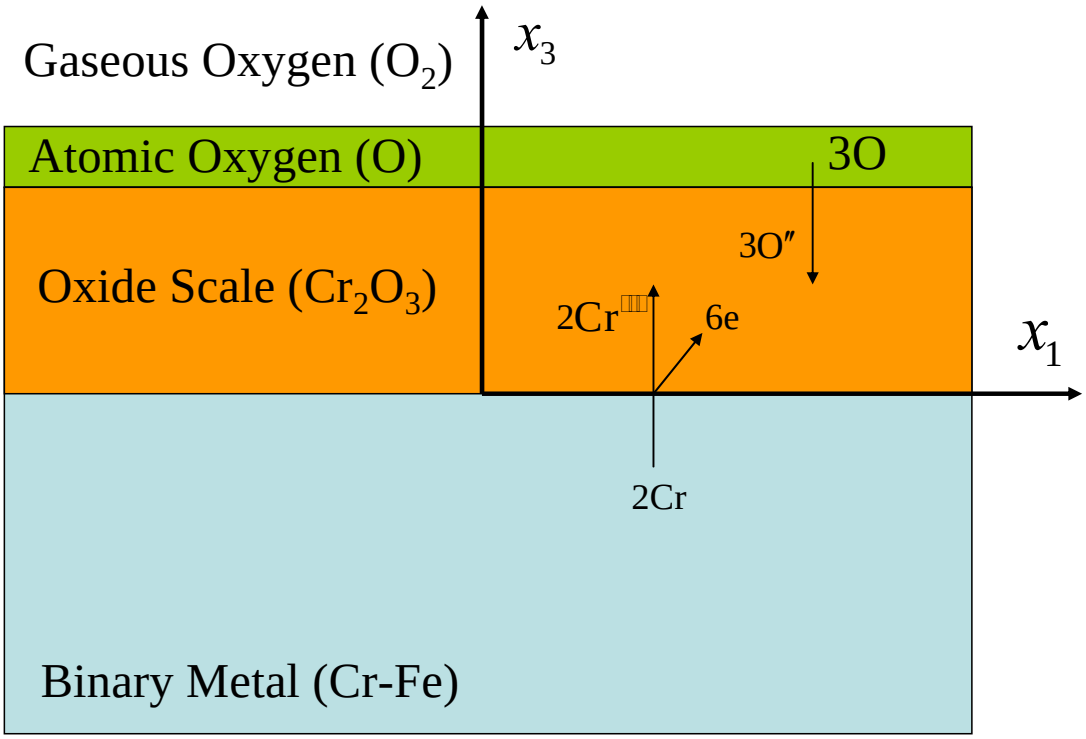

Figure 3.1 Schematic of the metal-oxide-gas structure (not to scale).

Kinematic Equations

The total deformation gradient tensor $\mathbf{F}$ is related to the displacement vector $\mathbf{U}(\mathbf{X}, t)$ through

$$\mathbf{F} = \mathbf{F}^e\mathbf{F}^c = \mathbf{I} + \nabla_X \mathbf{U} \quad , \quad \text{or} \quad \mathbf{F}^{-1} = (\mathbf{F}^e\mathbf{F}^c)^{-1} = \mathbf{I} - \nabla \mathbf{u} \quad . \tag{3.2}$$

The eigentransformation due to compositional change is given by

$$\mathbf{F}^c = \left(J^c\right)^{1/3}\mathbf{I} = \sqrt{1+2\sum_s \eta_s \Delta c_s}\,\mathbf{I} \quad . \tag{3.3}$$

where η_s is the coefficients of compositional expansion (CCE) and Δc_s is the deviation of molar fraction of c_s from its stoichiometric composition [36].

For the oxidation problem considered here, there are several species in the scale layer $0 \le x_3 \le h$ that may change their compositions. They are, respectively, $Cr^{\cdots}$ (s = Cr), O'' (s = O) and Cr_2O_3 (s = p), due to the formation of oxide from $Cr^{\cdots}$ and O''. For Cr_2O_3, we have $\eta_p = (2+3)/3 = 5/3$, while $\eta_{Cr^{\cdots}}$ and η_O can be measured experimentally or computed using molecular dynamic simulations [104]. In the metal ($x_3 < 0$), the chromium atom (s = Cr(a)) is the only independent diffusible species.

It then follows from the second of (3.2) that

$$\mathbf{F}^e = (\mathbf{I} - \nabla \mathbf{u})^{-1} \cdot \left(\mathbf{F}^c\right)^{-1} = \frac{(\mathbf{I} - \nabla \mathbf{u})^{-1}}{\sqrt{1+2\sum_s \eta_s \Delta c_s}} \quad , \tag{3.4}$$

$$\mathbf{E}^e = \frac{1}{2}\left[\left(\mathbf{F}^e\right)^T \mathbf{F}^e - \mathbf{I}\right] = \frac{1}{2}\left[\frac{1}{1+2\sum_s \eta_s \Delta c_s}\left[(\mathbf{I} - \nabla \mathbf{u})^{-1}\right]^T (\mathbf{I} - \nabla \mathbf{u})^{-1} - \mathbf{I}\right] \quad . \tag{3.5}$$

Kinetic Equations

The mechanical stresses in both the oxide scale and the metal substrate must satisfy the equilibrium equations. In terms of the first Piola-Kirchhoff stress tensor, the equilibrium equations can be written as

$$\nabla_X \cdot \boldsymbol{\sigma}^0 = \left(\nabla_x \cdot \boldsymbol{\sigma}^0\right) : \mathbf{F} = 0 \quad , \tag{3.6}$$

where the first gradient operator is with respect to the Lagrangian coordinates **X** and

the second one is with respect to the spatial coordinates **x** as indicated by the subscript. Making use of the Hooke's law, one can express the first Piola-Kirchhoff stress tensor in term of the deformation gradients,

$$\boldsymbol{\sigma}^0 = \left(\mathbf{C} : \mathbf{E}^e\right) \cdot \mathbf{F}^T \quad , \tag{3.7}$$

where **C** is the elastic stiffness tensor. In this study, it is assumed that **C** is independent of Δc_s .

Stress-Dependent Chemical Potential

Strictly speaking, electrochemical potentials should be used for the oxidation process. However, if local electroneutrality is assumed (as is done here), the diffusion process can be described using the chemical potential alone [36]. For most insulating and semi-conducting ceramics, local electroneutrality is an excellent assumption throughout the film, except for thin surface layers of a few nanometers [1, 105]. The stress-dependent chemical potential for a species *s* in ionic solids has been derived in [36],

$$\mu_s = \mu_s^0 + RT \ln c_s + V_s^m \tau_s \quad , \tag{3.8}$$

where μ_s^0 is the chemical potential of species *s* at some reference state, R and T are the universal gas constant and temperature, respectively, V_s^m is the molar volume of species *s* in its nature (stress-free stoichiometric state). The last term in (3.8) is the stress-dependent part of the chemical potential derived in [36]. If one assumes that the elastic stiffness tensor is independent of concentration, then τ_s reduces to

$$\tau_s = \eta_s \left(\frac{3}{2} \mathbf{E}^e : \mathbf{C} : \mathbf{E}^e - \frac{1}{J^c} \mathrm{tr}[\mathbf{F} \cdot \boldsymbol{\sigma}^0] \right) \quad , \tag{3.9}$$

where $J^c = \left\| \mathbf{F}^c \right\|$ is the Jacobian of the deformation gradient tensor, and $\mathbf{E}^e$ is the elastic strain given by (3.5).

Oxidation-Reduction Reaction in the Scale Layer ($0 \le x_3 \le h$)

During oxidation, every two $Cr^{\cdots}$ and three O'' will form a chromium oxide (chromina) molecule Cr_2O_3, or vice versa, i.e.,

$$2Cr^{\cdots} + 3O'' = Cr_2O_3 \quad . \tag{3.10}$$

Statistically speaking, both oxidation (forward) and reduction (backward) reactions may take place simultaneously. When the forward reaction is more favorable, there is a net increase of the product (Cr_2O_3). The newly formed oxide creates new lattice sites leading to scale growth. This is possible if and only if the forward reaction decreases the total free energy, i.e.,

$$dG = d\mu_p - 2d\mu_{\mathrm{Cr}} - 3d\mu_{\mathrm{O}} < 0 , \tag{3.11}$$

where μ_{Cr}, μ_{O} and μ_p are, respectively, the chemical potentials of $Cr^{\cdots}$, O'' and the product Cr_2O_3. Clearly, chemical equilibrium is achieved when $dG = 0$.

It follows from the chemical equation (3.10) that the rate of forward reaction is given by $k_f c_{\mathrm{Cr}}^2 c_{\mathrm{O}}^3$, and the rate of backward reaction is given by $k_b c_p$, where k_f and k_b are the reaction rate constants of the forward and backward reactions, respectively. Therefore, the net rate of increase of the product is given by

$$R_p = k_f c_{\mathrm{Cr}}^2 c_{\mathrm{O}}^3 - k_b c_p .$$

At chemical equilibrium, the net rate should be zero.

Since the chemical potentials are stress-dependent, it can be easily

shown that the reaction rate constants k_f and k_b are stress-dependent,

$$k_f = k_f^0 \exp\left[-\frac{V_p^m \tau_p}{RT}\right] \quad , \quad k_b = k_b^0 \exp\left[-\frac{2V_{\mathrm{Cr}}^m \tau_{\mathrm{Cr}} + 3V_{\mathrm{O}}^m \tau_{\mathrm{O}}}{RT}\right] \quad , \tag{3.13}$$

where k_f^0 and k_b^0 are, respectively, the forward and backward reaction rate constants when there is no mechanical stress.

Diffusion and Fluxes

In the scale layer ($0 \le x_3 \le h$), it is assumed that the oxide (product) does not diffuse, although its lattice may still move (convection) due to internal oxidation. The diffusion fluxes of $\mathrm{Cr}^{\cdots}$ and O'' are related to their chemical potentials through

$$\mathbf{J}_s = -\frac{D_s c_s}{RT} \nabla \mu_s , \qquad \text{for } s = \text{Cr and O} \tag{3.14}$$

where ∇ is the gradient operator with respect to the spatial coordinates **x**, and D_s is the effective diffusivity of specie *s* in the oxide scale. Substitution of (3.8) into (3.14) yields,

$$\mathbf{J}_s = -\frac{D_s c_s}{RT}\left[RT\frac{\nabla c_s}{c_s} + V_s^m \nabla \tau_s\right], \quad \text{for } s = \text{Cr and O} \tag{3.15}$$

Similarly, in the metal substrate ($x_3 < 0$), the diffusion flux of chromium is given by

$$\mathbf{J}_{\mathrm{Cr}(a)} = -\frac{D_{\mathrm{Cr}(a)} c_{\mathrm{Cr}(a)}}{RT}\left[RT\frac{\nabla c_{\mathrm{Cr}(a)}}{c_{\mathrm{Cr}(a)}} + V_{\mathrm{Cr}(a)}^m \nabla \tau_{\mathrm{Cr}(a)}\right] \quad , \tag{3.16}$$

where $D_{\mathrm{Cr}(a)}$ is the diffusivity of atoms in the metal alloy.

It is to be noted that the mass diffusion and fluxes discussed above are the mass motion relative to a background lattice. In the scale layer, this background lattice is the Cr_2O_3 lattice already formed. In the metal substrate, this background lattice is the original Fe-Cr lattice.

Continuity Equation

When new oxide is created near the scale-metal interface, or internally within the scale layer, the existing Cr_2O_3 lattice will need move to accommodate the new lattice sites. Therefore, the motion of a diffusible species in the oxide scale consists of both diffusion relative to the background lattice and the transport of the background lattice itself. This situation is called convective diffusion [106]. The continuity equation in a fixed coordinate (Eulerian description) system for the product is thus given by

$$\frac{\partial c_p}{\partial t} = R_p - \nabla \cdot \left(c_p \mathbf{v} \right) \quad . \tag{3.17}$$

where R_p is the net rate of oxide generation given by (3.12), and $\mathbf{v} = \mathbf{v}(\mathbf{x}, t) = \partial \mathbf{u}(\mathbf{x}, t) / \partial t$ is the spatial velocity distribution given as a function of time t and the Eulerian coordinates $\mathbf{x}$. The left hand side of (3.17) is the change of product concentration. It equals the rate of product generation plus the net flow (convection) due to the transport of the existing background lattice. This convective term is necessary because convection may also change the concentration locally at a fixed spatial location. The inclusion of this convective term in (3.17) is one of the major differences between the present model and that of [37].

For the diffusing ions, the mass transport due to diffusion needs to be included in the continuity equation. Thus, the continuity equations for $Cr^{\cdot\cdot\cdot}$ and

O'' become

$$\frac{\partial c_{\mathrm{Cr}}}{\partial t} = -2R_p - \nabla \cdot \mathbf{J}_{\mathrm{Cr}} - \nabla \cdot \left(c_{\mathrm{Cr}} \mathbf{v} \right), \tag{3.18}$$

and

$$\frac{\partial c_{\mathrm{O}}}{\partial t} = -3R_p - \nabla \cdot \mathbf{J}_{\mathrm{O}} - \nabla \cdot \left(c_{\mathrm{O}} \mathbf{v} \right). \tag{3.19}$$

In other words, the time-rate of change of the ion concentration equals to the local consumption ($-2R_p$ for $Cr^{\cdots}$ and $-3R_p$ for O''), plus the diffusion and plus the convection.

In the metal substrate, the only contribution to the local rate of change of Cr concentration comes from diffusion. Thus, the continuity equation becomes

$$\frac{\partial c_{\mathrm{Cr}(a)}}{\partial t} = -\nabla \cdot \mathbf{J}_{\mathrm{Cr}(a)} \quad . \tag{3.20}$$

Boundary Value Problem

Consider the oxide scale first. It follows from (3.2) - (3.5) that $\boldsymbol{\sigma}^0$, $\mathbf{F}^e$, $\mathbf{F}^c$ and $\mathbf{E}^e$ can be expressed in terms of six unknown scalar functions $\mathbf{u}(\mathbf{x},t)$ and $c_s(\mathbf{x},t)$ for s = Cr, O and p. Making use of these relationships in continuity conditions (3.17) - (3.19) and the kinetic condition (3.6) yields six partial differential equations for the six unknown scalar functions $\mathbf{u}(\mathbf{x},t)$ and $c_s(\mathbf{x},t)$ (s = Cr, O and p).

Similarly, in the metal substrate, it follows from (3.16), (3.20), (3.7), and (3.5) that $\boldsymbol{\sigma}^0$, $\mathbf{F}^e$, $\mathbf{F}^c$ and $\mathbf{E}^e$ can be expressed in terms of four unknown scalar functions $\mathbf{u}(\mathbf{x},t)$ and $c_{\mathrm{Cr}(a)}(\mathbf{x},t)$. Making use of these relationships in

continuity condition (3.20) and the kinetic condition (3.6) yields four partial differential equations for the four unknown scalar functions $\mathbf{u}(\mathbf{x},t)$ and $c_{\mathrm{Cr}(a)}(\mathbf{x},t)$.

With proper continuity conditions at the scale-air and metal-scale interfaces, and proper boundary conditions on the sides of the structure depicted in Figure 3.1, these partial differential equations formulate a boundary value problem that can be solved to obtain the deformation, stresses and the defect concentration throughout the scale layer and the metal substrate, as well as the oxidation kinetics.

3.3. One-Dimensional Examples

To illustrate the utility of the model formulated above and to reveal certain fundamental features of the model predictions, we present some numerical examples in this section. To this end, we assume that all the material properties are independent of the ion concentration. Also, the scale layer and the metal substrate are assumed to be linear elastic and isotropic solids with E_n and ν_n being the elastic constants for the oxide (n = 1) and the metal (n = 2). Furthermore, it is assumed that the elastic constants are independent of the defect concentration. This is valid for case of the dilute concentration.

3.3.1. Normalization

Next, we assume that the boundary conditions on the vertical sides are such that the total width of the sample as shown in Figure 3.1 remains the same, and the scale grows in the vertical (x_3) direction only. Consequently, $u_1 = u_2 = 0$, $u_3 = u_3(x_3,t)$ and $c_s = c_s(x_3,t)$. Therefore, the problem becomes effectively a one-dimensional one in which all the quantities depend on the vertical coordinate x_3

only.

To facilitate the numerical solutions, we introduce a length scale $\lambda = \sqrt{D_{\mathrm{Cr}} / k_f^0}$ and a time scale $\tau = 1/k_f^0$. The non-dimensional time, spatial coordinate and displacement can then be defined as,

$$\hat{x}_3 = \frac{x_3}{\lambda}, \qquad \hat{u} = \frac{u}{\lambda}, \qquad , \quad \hat{t} = \frac{t}{\tau} \quad . \tag{3.21}$$

One advantage of such normalization is that the governing equations and boundary conditions become independent of k_f^0 when written in terms the above non-dimensional variables.

3.3.2 Governing Equations in 1-D

For the specific one-dimensional problem considered in this section, it is easy to see that in both the scale layer and the metal substrate, the only non-zero stress components are $\sigma_{11}^0 = \sigma_{22}^0$. This leads to

$$\frac{\partial \hat{u}_3}{\partial \hat{x}_3} = \frac{1+\nu_1}{1-\nu_1} \sum_k \eta_k \Delta c_k \, . \tag{3.22}$$

Consequently, in the scale layer, the continuity equations (3.17) - (3.19) become

$$\begin{aligned} \frac{\partial c_{\mathrm{Cr}}}{\partial \hat{t}} &= -2 c_{\mathrm{Cr}}^2 c_{\mathrm{O}}^3 \exp\left(-\hat{\eta}_p \sum_s \eta_s \Delta c_s \right) \\ &\quad + \frac{\partial^2 c_{\mathrm{Cr}}}{\partial \hat{x}_3^2} + \hat{\eta}_{\mathrm{Cr}} \frac{\partial}{\partial \hat{x}_3} \left[c_{\mathrm{Cr}} \sum_s \eta_s \frac{\partial c_s}{\partial \hat{x}_3} \right] - \frac{\partial}{\partial \hat{x}_3} \left(c_{\mathrm{Cr}} \frac{\partial \hat{u}_3}{\partial \hat{t}} \right) \end{aligned} \quad , \tag{3.23}$$

$$\frac{\partial c_{\mathrm{O}}}{\partial \hat{t}} = -3c_{\mathrm{Cr}}^2 c_{\mathrm{O}}^3 \exp\left(-\hat{\eta}_p \sum_s \eta_s \Delta c_s\right)$$
$$+ \frac{D_{\mathrm{O}}}{D_{\mathrm{Cr}}} \frac{\partial^2 c_{\mathrm{O}}}{\partial \hat{x}_3^2} + \hat{\eta}_{\mathrm{O}} \frac{D_{\mathrm{O}}}{D_{\mathrm{Cr}}} \frac{\partial}{\partial \hat{x}_3}\left[c_{\mathrm{O}} \sum_s \eta_s \frac{\partial c_s}{\partial \hat{x}_3}\right] - \frac{\partial}{\partial \hat{x}_3}\left(c_{\mathrm{O}} \frac{\partial \hat{u}_3}{\partial \hat{t}}\right), \tag{3.24}$$

$$\frac{\partial c_p}{\partial \hat{t}} = c_{\mathrm{Cr}}^2 c_{\mathrm{O}}^3 \exp\left(-\hat{\eta}_p \sum_s \eta_s \Delta c_s\right) - \frac{\partial}{\partial \hat{x}_3}\left(c_p \frac{\partial \hat{u}_3}{\partial \hat{t}}\right), \tag{3.25}$$

where

$$\hat{\eta}_s = \frac{2V_s^m E_1 \eta_s}{RT(1-\nu_1)} \tag{3.26}$$

measures the coupling between stress and diffusion.

Furthermore, it follows from (3.7) and (3.9) that the non-zero stress components in the scale layer are

$$\sigma_{11}^0 = \sigma_{22}^0 = -\frac{E_1}{1-\nu_1} \sum_s \eta_s \Delta c_s \quad , \tag{3.27}$$

and the stress-dependent part of the chemical potential is

$$\tau_s = \frac{2E_1 \eta_s}{1-\nu_1} \sum_k \eta_k \Delta c_k \quad . \tag{3.28}$$

In the metal substrate, the continuity equation (3.20) becomes

$$\frac{\partial c_{\mathrm{Cr}(a)}}{\partial \hat{t}} = \frac{D_{\mathrm{Cr}(a)}}{D_{\mathrm{Cr}}} \frac{\partial^2 c_{\mathrm{Cr}(a)}}{\partial \hat{x}_3^2} + \hat{\eta}_{\mathrm{Cr}(a)} \frac{D_{\mathrm{Cr}(a)}}{D_{\mathrm{Cr}}} \frac{\partial}{\partial \hat{x}_3}\left[c_{\mathrm{Cr}(a)} \eta_{\mathrm{Cr}(a)} \frac{\partial c_{\mathrm{Cr}(a)}}{\partial \hat{x}_3}\right] \quad . \tag{3.29}$$

The non-zero stress components in the metal substrate are

$$\sigma_{11}^0 = \sigma_{22}^0 = -\frac{E_2}{1-\nu_2} \eta_{\mathrm{Cr}(a)} \Delta c_{\mathrm{Cr}(a)} \quad . \tag{3.30}$$

And the corresponding stress-dependent part of the chemical potential is

$$\tau_{\mathrm{Cr}(a)} = \frac{2E_2\eta_{\mathrm{Cr}(a)}}{1-\nu_2}\eta_{\mathrm{Cr}(a)}\Delta c_{\mathrm{Cr}(a)} \quad . \tag{3.31}$$

It can be easily seen that the above stress fields automatically satisfy the equilibrium equation (3.6).

3.3.3 Boundary Conditions

In addition to the governing equations above, interface conditions need to be specified. In the structure shown in Figure 3.1, there are two interfaces, the metal-scale interface and the scale-air interface. At these interfaces, the following conditions must be satisfied: (a) mass flux continuity of each species, (b) continuity of chemical potential of each species for adsorption and ionization reaction, respectively, (c) continuity of displacement and (e) continuity of traction. These conditions are described below.

Metal-Scale Interface ($x_3 = 0$)

At the metal-scale interface, ionization of Cr atoms is assumed to be an equilibrium process. Thus, continuity of chemical potentials must hold between $\mathrm{Cr}^{\square\square}$ ions and Cr atoms, i.e.

$$\frac{\mu^0_{\mathrm{Cr}(a)} - \mu^0_{\mathrm{Cr}}}{RT} + \ln\frac{c_{\mathrm{Cr}(a)}}{c_{\mathrm{Cr}}} = \hat{\eta}_{\mathrm{Cr}}\sum_k \eta_k \Delta c_k - \hat{\eta}_{\mathrm{Cr}(a)}\eta_{\mathrm{Cr}(a)}\Delta c_{\mathrm{Cr}(a)} \quad . \tag{3.32}$$

Conservation of mass for Cr across the interface leads to

$$\frac{\partial c_{\mathrm{Cr}(a)}}{\partial \hat{x}_3} + \hat{\eta}_{\mathrm{Cr}(a)}\left[c_{\mathrm{Cr}(a)}\eta_{\mathrm{Cr}(a)}\frac{\partial c_{\mathrm{Cr}(a)}}{\partial \hat{x}_3}\right] = \frac{D_{\mathrm{Cr}}}{D_{\mathrm{Cr}(a)}}\frac{\partial c_{\mathrm{Cr}}}{\partial \hat{x}_3} + \hat{\eta}_{\mathrm{Cr}}\frac{D_{\mathrm{Cr}}}{D_{\mathrm{Cr}(a)}}\left[c_{\mathrm{Cr}}\sum_s \eta_s \frac{\partial c_s}{\partial \hat{x}_3}\right] \quad . \tag{3.33}$$

Furthermore, per the assumption that no O'' can cross the interface into the metal, the O'' flux must cease at the interface, i.e.,

$$\frac{\partial c_{\mathrm{O}}}{\partial \hat{x}_3} + \hat{\eta}_{\mathrm{O}} \left[c_{\mathrm{O}} \sum_s \eta_s \frac{\partial c_s}{\partial \hat{x}_3} \right] = 0 \quad . \tag{3.34}$$

Finally, traction continuity is automatically satisfied by the choice of stress components, and the continuity of displacement leads to

$$\hat{u}_3\big|_{\hat{x}_3=0^+} = \hat{u}_3\big|_{\hat{x}_3=0^-} \quad . \tag{3.35}$$

At the Scale-Air Interface ($\hat{x}_3 = h/\lambda$)

At the scale-air interface, equilibrium condition is assumed for ionization of oxygen (in the air), i.e.,

$$\frac{1}{2RT}\mu^0_{\mathrm{O}_2} + \ln P^{1/2}_{\mathrm{O}_2} = \frac{\mu^0_{\mathrm{O}}}{RT} + \ln c_{\mathrm{O}} + \hat{\eta}_{\mathrm{O}} \sum_k \eta_k \Delta c_k \quad . \tag{3.36}$$

where $\mu^0_{\mathrm{O}_2}$ is the standard chemical potential of oxygen gas and P_{O_2} is the oxygen partial pressure in the air. Note that *h* is not known a priori. It is a function of time that needs to be solved. In addition, since the $\mathrm{Cr}^{\square\square}$ ions cannot leave the scale, their flux must follow the Stefan [107] condition at the scale-air interface, i.e.,

$$\frac{\partial c_{\mathrm{Cr}}}{\partial \hat{x}_3} + \hat{\eta}_{\mathrm{Cr}} \left[c_{\mathrm{Cr}} \sum_s \eta_s \frac{\partial c_s}{\partial \hat{x}_3} \right] = -c_{\mathrm{Cr}} \frac{d\hat{u}_3}{d\hat{t}} \quad . \tag{3.37}$$

Furthermore, it is assumed that, in comparison with the stresses in the scale layer, the atmosphere pressure is negligible in typical applications. Thus, the scale-air interface can be viewed as a traction free surface which is satisfied by the choice of the stress components.

An additional condition needed is $c_{Cr(a)} = C$ as $x_3 \to -\infty$.

3.3.4. Numerical Solution Procedure

The governing equations are solved by a finite-difference method. A very thin initial scale thickness $h(t)\big|_{t=0} = h_0 = 20\,\text{nm}$ is assumed initially. The material properties of 16% (wt) Fe-Cr alloy and its oxide used in the numerical simulation are listed in Table 3.1. Oxygen partial pressure is set to be 0.3 atm at the air-oxide interface. Furthermore, it is assumed that once the oxide is formed, it is stable and no reduction takes place. This means that the backward reaction rate constant $k_b^0 = 0$.

By substituting (3.22) into (3.23) – (3.25) and (3.29) to eliminate u_3, we arrive at four partial differential equations with four unknown functions. They are c_{Cr}, c_{O}, c_p in the oxide scale and $c_{\text{Cr}(a)}$ in the metal. These four equations were solved by an explicit finite-difference method. The time step used is $\Delta t = 1\,\text{sec}$. The initial scale layer of thickness h_0 was first divided evenly into n = 3 elements with n + 1 = 4 nodes across the thickness. At $t = 0$, all the quantities c_{Cr}, c_{O}, c_p are known throughout the initial scale layer, and $c_{\text{Cr}(a)}$ is known throughout the metal. Equations (3.23) – (3.25) and (3.29) can then be integrated with respect to time to obtain the values of c_{Cr}, c_{O}, c_p and $c_{\text{Cr}(a)}$ at the next time step, $t = \Delta t$. The integration constants are determined by the initial and boundary conditions. Once the values of c_{Cr}, c_{O}, c_p are known for $t = \Delta t$, the displacement $u_3(x,t)$ can be obtained from (3.22). Consequently, the scale thickness at $t = \Delta t$ is given by $h_1 = h_0 + u_3(h_0, \Delta t)$. The above process can then be repeated *N* times to obtain the solutions at any desired time, $t = N\Delta t$.

3.3.5. Results and Discussion

The scale thickness is plotted as the solid line in Figure 3.2. The triangle symbols in Figure 3.2 are the experimental results by Kurokawa et al. [108]. For comparison purpose, numerical results without accounting for the stress-diffusion interaction are also plotted in the same figure as the dotted line. It is seen that neglecting the stress-diffusion interaction overestimates the scale thickness, particularly over the longer time period. This is because the compressive stress developed in the scale layer can significantly reduce the diffusion of ions, thus slowing down the scale growth.

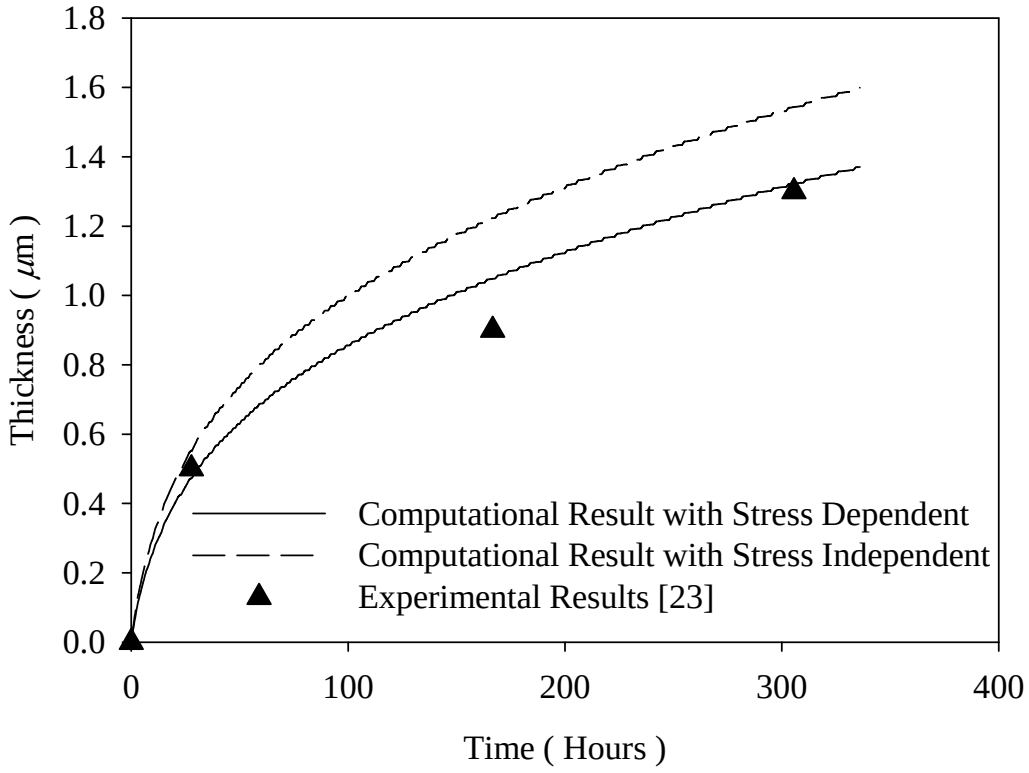

Figure 3.2 Oxidation kinetics profile of 16% (wt) Cr alloy.

Table 3.1 Material properties of 16% Fe-Cr alloy and its oxide

Chromia properties	Symbol	Value
Chemical expansion coefficient	η_{Cr}	0.05
	η_O	0.02
	η_p	5/3
Diffusivity of Chromium ion	D_{Cr}	5.8×10^{-13} cm^2/s
Diffusivity of Oxygen ion	D_O	3.0×10^{-15} cm^2/s
Temperature	T	1073 K
Young's modulus	E	250 GPa
Poisson's coefficient	v	0.27
Molar volume	V^m_p	2.92×10^{-5} m^3/mol
16% (wt) Fe-Cr alloy properties	Symbol	Value
Chemical expansion coefficient	$\eta_{\mathrm{Cr}(a)}$	0.05
Diffusivity of Chromium atom	$D_{\mathrm{Cr}(a)}$	2.86×10^{-15} cm^2/s In Grain Volume
		1.57×10^{-13} cm^2/s In Grain Boundary
		6×10^{-15} cm^2/s Effective
Young's modulus	E	162.3 GPa
Poisson's coefficient	v	0.29

Shown in Figure 3.3 is the stress distribution across the thickness of the scale layer at four different oxidation times. The thickness is measured from the metal-scale interface. The right end of the curves indicates the thickness of the scale when the stress distribution is measured. It is seen that spatially the maximum (compressive) stress occurs at the metal-scale interface, and the stress decreases gradually with distance from the interface. Very near the air-scale interface, the stress decreases abruptly.

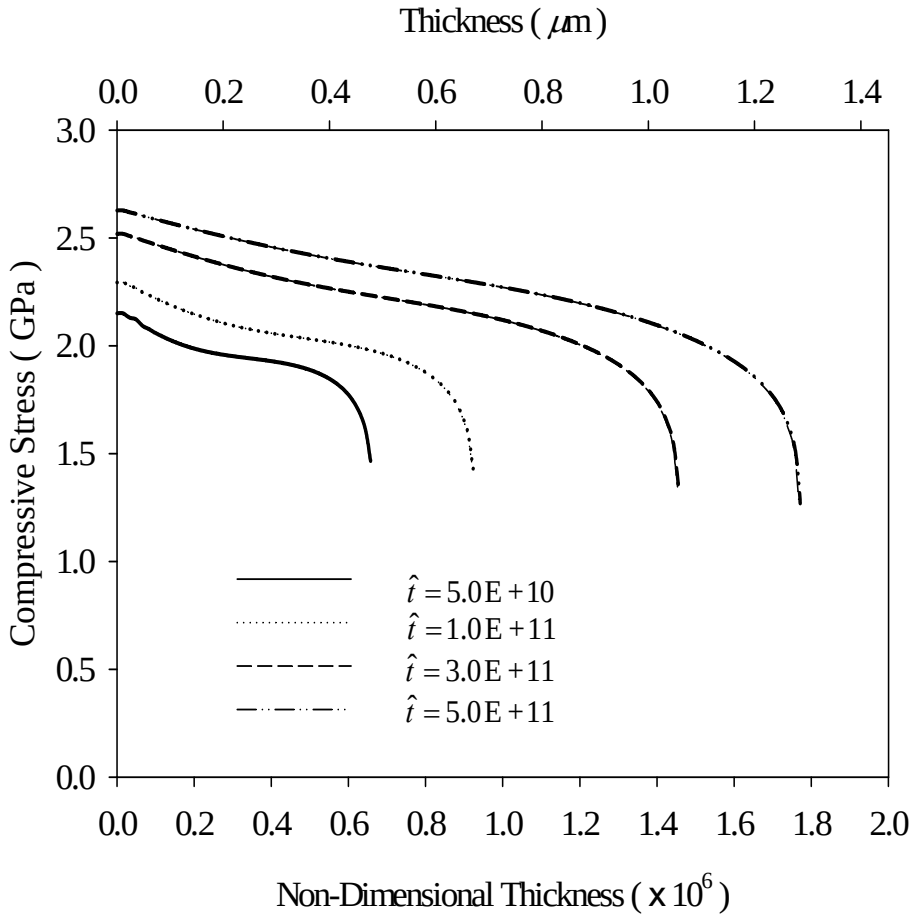

Figure 3.3 Stress Distribution along scale thickness at different times.

The temporal evolution of the stress at several different locations within the scale layer is shown in Figure 3.4. It is seen that the compressive stress increases with time, and eventually saturates. For the example considered here, the maximum saturated compressive stress is about 2.6GPa, occurring on the scale side of the metal-scale interface. Interestingly, the newly formed oxide starts with zero stress, increases very quickly within a few minutes to a somewhat saturated value. This is because when new oxide just formed, it is not fully dense yet. There is still

room for adding more oxide before compressive stresses are fully developed. Once the density reaches a threshold value, stress will remain relatively constant. This result contradicts that of [1] where the numerical results seem to indicate that the stress at any point in the scale layer keeps increasing without bound.

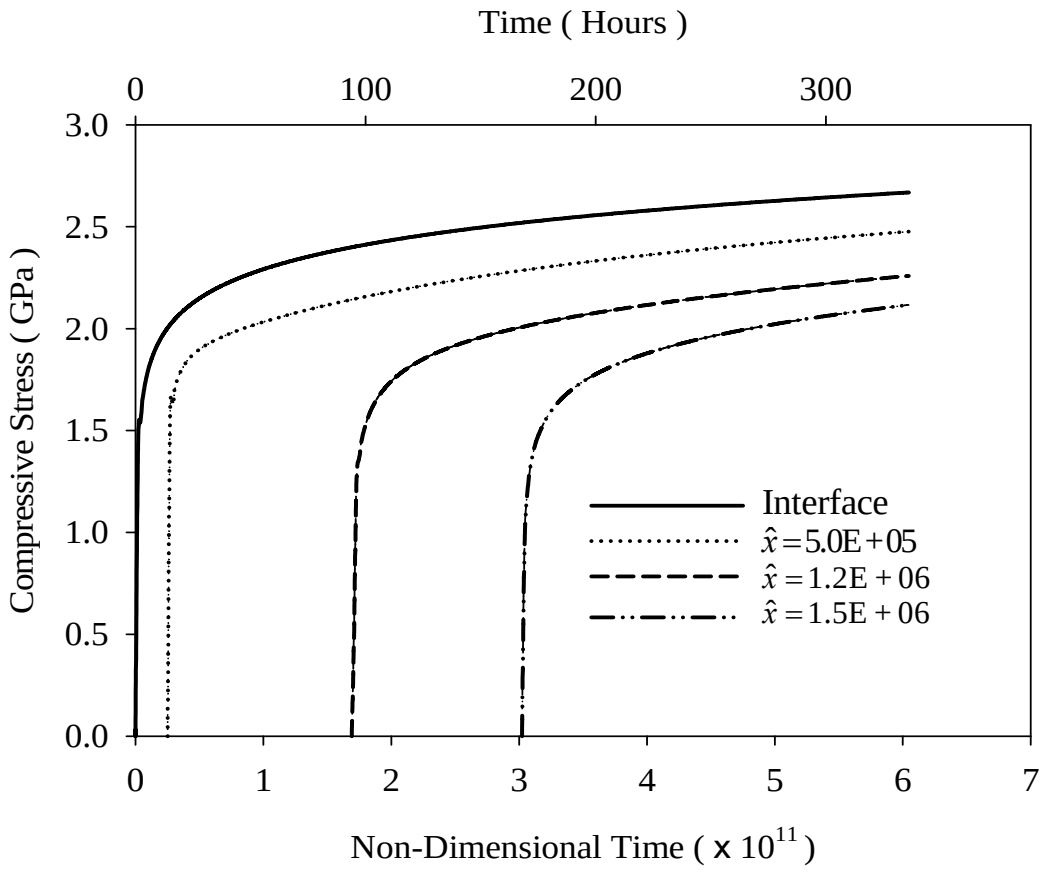

Figure 3.4 Stress evolution over time at different locations within the scale layer.

To further illustrate the oxidation kinetics, the stress-dependent oxidation rate constant k_f as given by the first of (3.13) is plotted in Figure 3.5 at four different locations in the scale. As expected, at a given location, the oxidation rate starts at a higher value and decreases very quickly to almost zero. This is

consistent with the stress distribution shown in Figure 3.4, i.e., compressive stress in the oxide grows rapidly to prohibit further internal oxidation. Consequently, new oxide grows primarily on the air-scale interface, which is consistent with the experimental observation [109] that Cr ion diffusion is predominant in the oxide layer for Fe-Cr alloys. In fact, if new oxide is formed primarily on the air-scale interface, there must be strong upward diffusion of Cr ions. This can also be seen from the Cr ion distribution across the scale thickness as shown in Figure 3.6. Because of the prescribed constant supply of Cr atoms at the metal substrate, the concentration of Cr ion in the scale layer near the scale-metal interface is the highest and remains constant, $c_{\mathrm{Cr}} \approx 0.018$. Cr ion concentration is the lowest near the air-scale interface, and continuously decreases with time.

On the other hand, the oxygen ion concentration is the lowest ($c_{\mathrm{O}} \approx 0.012$) at the scale-metal interface, and remains almost constant for about 1/3 of the scale thickness, as shown in Figure 3.7. It then increases quickly towards the air-scale interface and reaches the prescribed $c_{\mathrm{O}} = 0.025$, a value dictated by the prescribed oxygen partial pressure $P_{\mathrm{O}_2} = 0.3$ and (3.36).

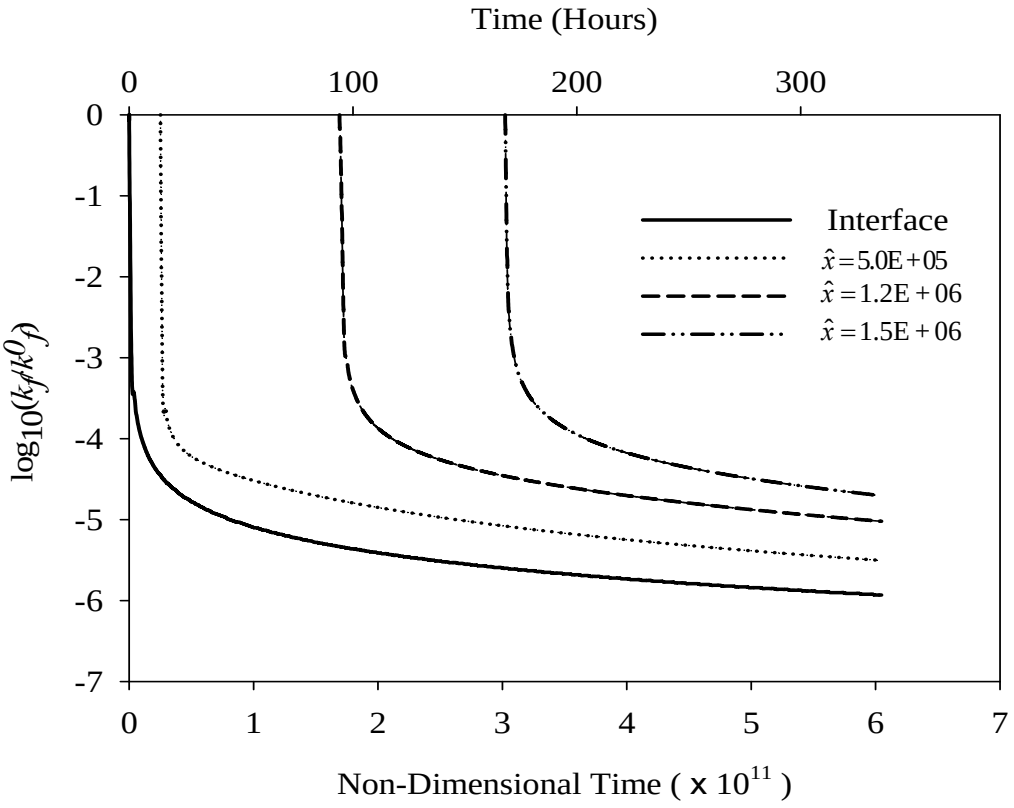

Figure 3.5 Oxidation reaction rate constant (normalized) versus time at different locations within the scale layer.

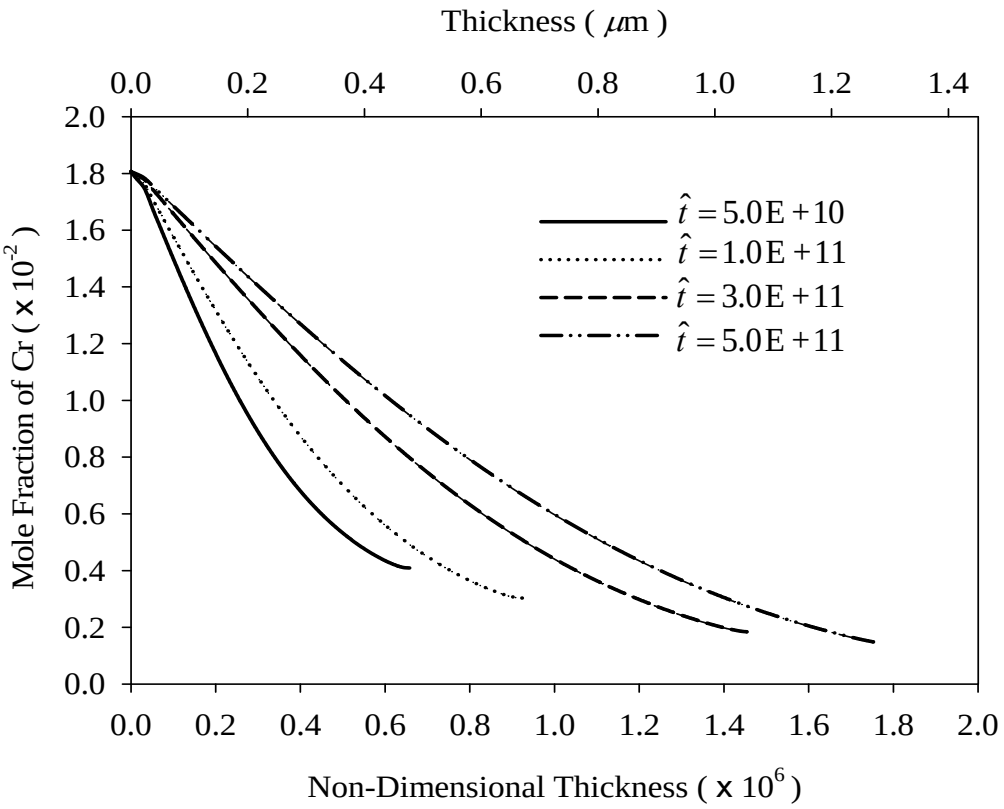

Figure 3.6 Distribution of Cr ion across the scale thickness at different times.

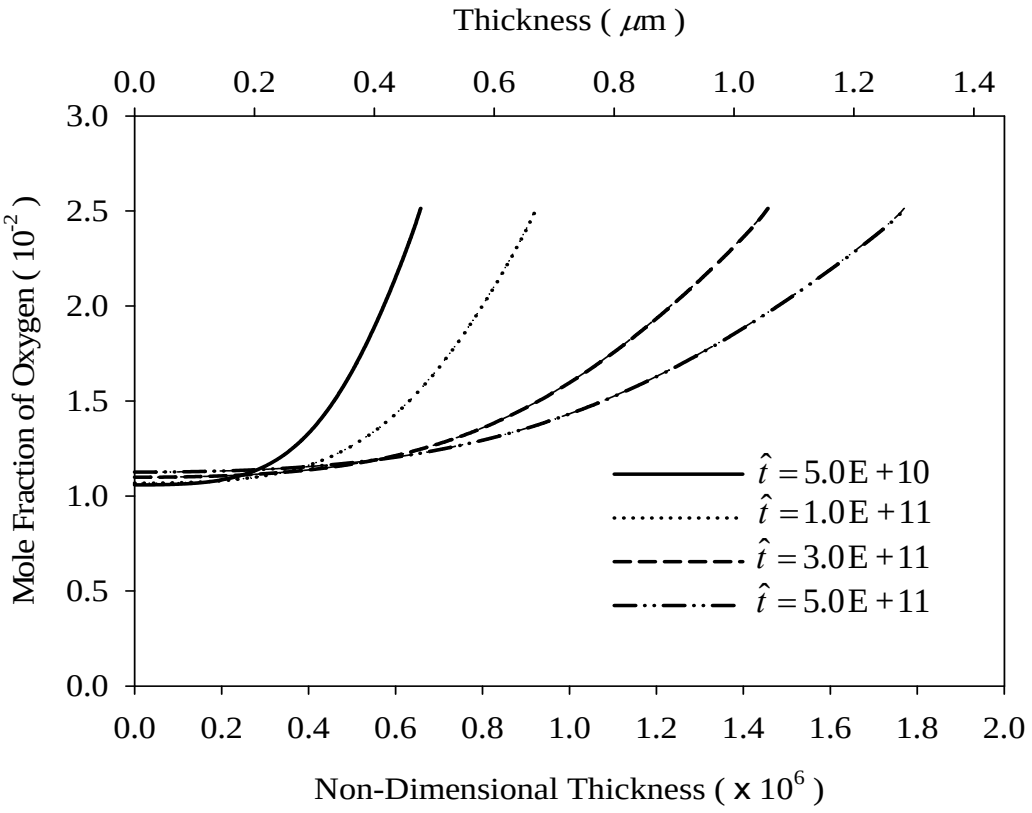

Figure 3.7 Distribution of O ion across the scale thickness at different times.

To further understand the oxidation kinetics, the upward motion velocity of the oxide lattice $\hat{u}_3(\hat{x}_3,\hat{t})$ is plotted in Figure 3.8 across the scale-layer thickness at different times. It is seen that after about 100 hours, the oxide lattice over much of the scale-layer no longer moves upward anymore. In other words, the convective motion of the lattice due to internal oxidation is significant only very near the air-scale interface. This also implies that internal oxidation eventually becomes insignificant over long time oxidation, and the growth of new oxide is primarily at the air-scale interface. The oxidation is thus controlled primarily by the upward diffusion of Cr ions across the scale-layer, and the kinetics becomes parabolic. This

is further verified by plotting the parabolic rate constant $k_p = \hat{h}^2/\hat{t}$, see Figure 3.9. It is seen that the kinetics is not parabolic in the early stage of oxidation.

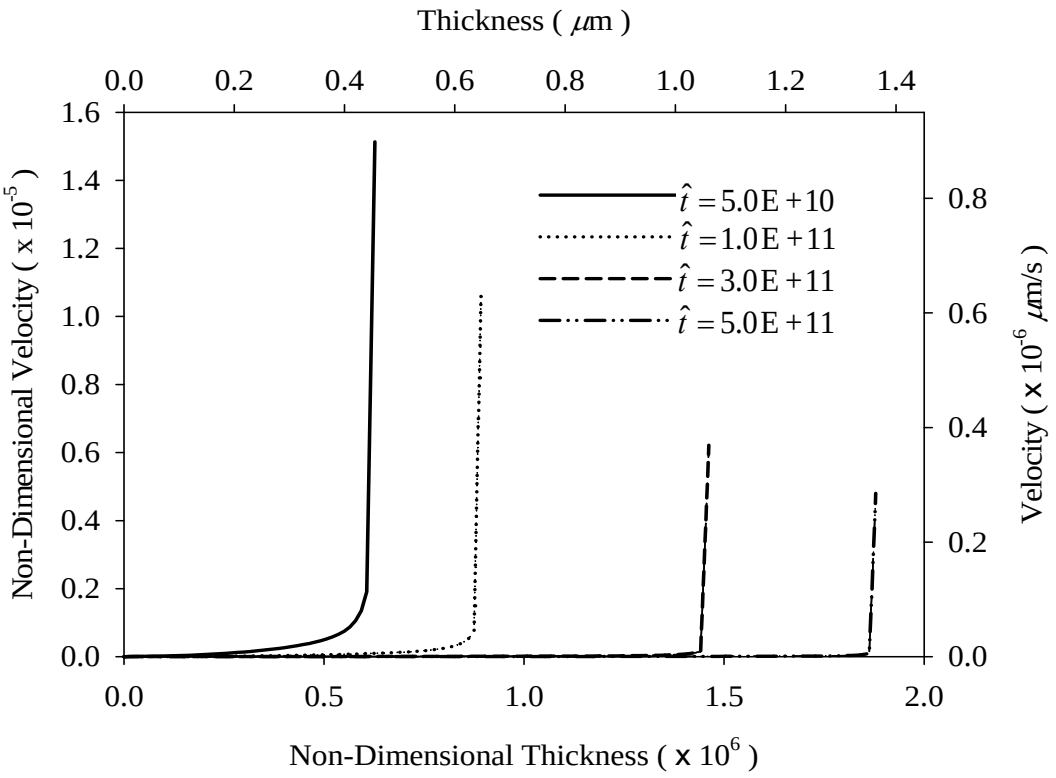

Figure 3.8 Distribution of oxide velocity across the scale thickness at different times.

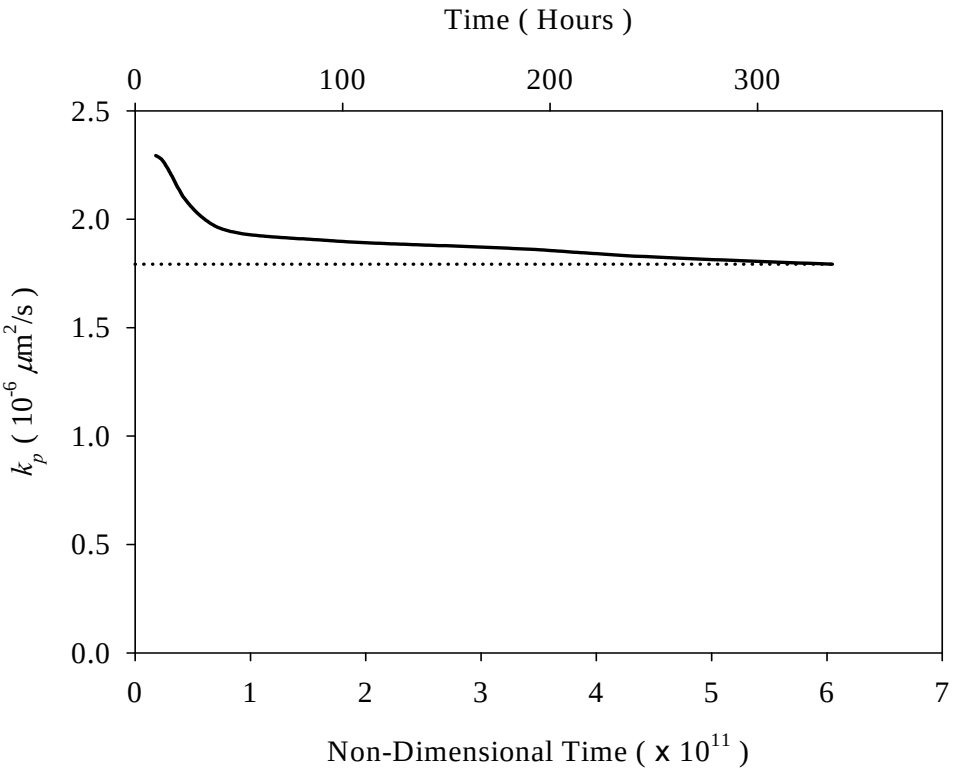

Figure 3.9 The evolution of k_p over time

3.4 Finite Element Analysis of Oxidation Induced Metal Depletion at Oxide-Metal Interface

In this section, we aim to apply the stress-diffusion coupled model in 2-D geometry with specific interest in metal depletion at alloy grain boundaries and their adjacent stress distribution during the selective oxidation of Fe-Cr alloys. Spallation of the protective oxide layer is associated with metal depletion effects [26, 99, 110] at the oxide layer/alloy interfaces. Seo et. al. [99] observed a Cr-depletion zone in their study on selective oxidation of Fe-Cr alloy in pure oxygen, and concluded that the transport of Cr in the oxide film contributes to the formation of a

Cr-depletion zone. A deeper observation at the metal oxide interface made by Howes [26] shows that the most severe depletions occur at the grain boundaries (Figure 3.10). Modeling the solute depletion process usually employs solving the diffusion equations through the sample volume. Since depletion is the only modeling object, the stress profile around the interface is not included. On the other hand the aforementioned residual stress models are all for 1-D geometry and did not consider a possible metal depletion effect. Therefore, this 2-D implementation is necessary for understanding the coupled stress-oxidation phenomenon.

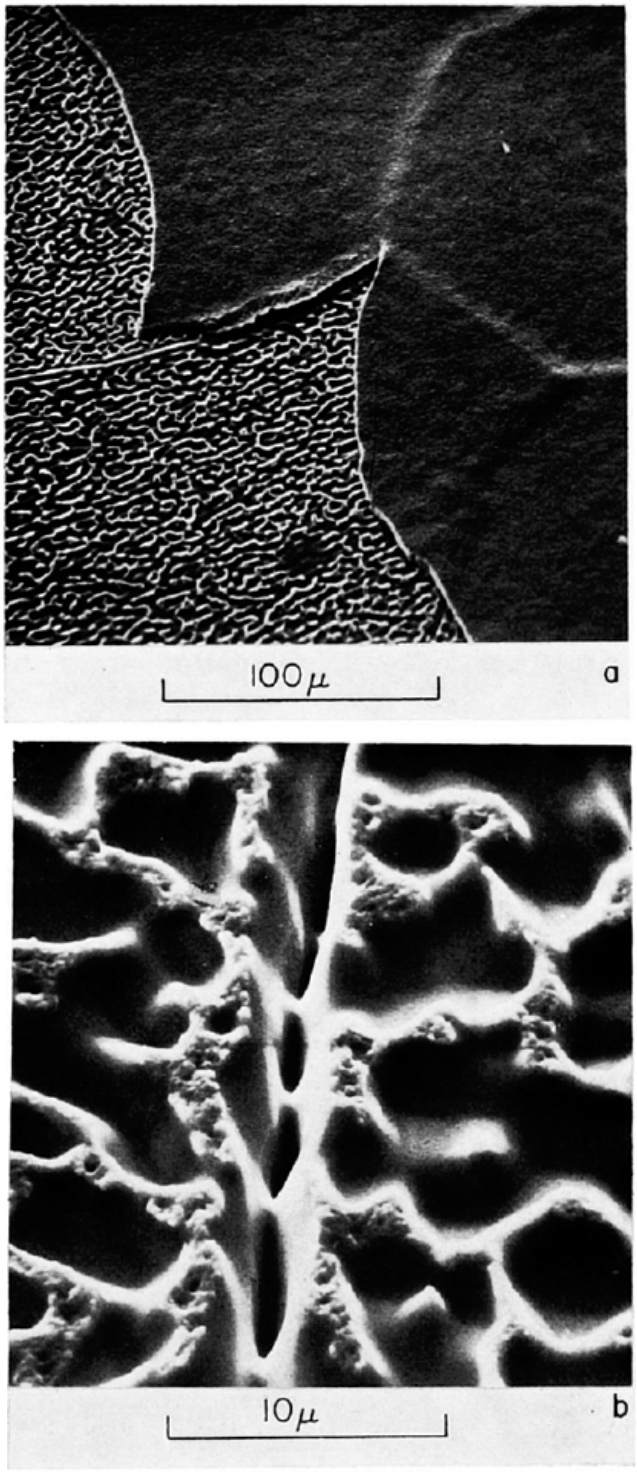

Figure 3.10 a) Oxide and the alloy surface after partial spalling. b) Sorrugated alloy surface and the crevasses formed at a grain boundary [26].

3.4.1 Voronoi Tessellation

Voronoi tessellation is a well established method to represent polycrystalline solid models. In a Voronoi tessellation space, 'seed points' (represented by P_i) are randomly distributed in space (3D) or in a plane (2D). All other points in the space that are close to a 'seed point' than to any other 'seed points' are grouped as a region which defines the Voronoi tessellation. For 2D space, Voronoi tessellation divides the space into an array of convex, space filling polygon. The mathematical description of Voronoi tessellation is given as

$$\mathbf{V}_i = \left\{ x_i : d\left(x_i, P_i\right) \le d\left(x_i, P_j\right); i \ne j; i, j = 1, 2, 3 \cdots\cdots n \right\} \tag{3.38}$$

where $\mathbf{V}_i$ represents a grain set, x_i denotes a random point in the space, $d\left(x_i, P_i\right)$ is the distance between P_i and x_i, and n represents the total number of points in the space.

The greatest advantage of Voronoi tessellation is that it has been extensively used to characterize the grain aggregation, grain boundary phenomena. Kumar and Kurtz [111] used a 3D Voronoi tessellation to calculate the effective thermal expansion coefficient of polycrystalline materials. Microscopic based macroscopic material behavior modeling with Voronoi tessellation is not only limited in this, but also in creep fracture [112], constitutive relations [113-114] and electrical conductance [115] and many other areas. On the other hand, Voronoi tessellation has also been used for research on local phenomena, especially those at grain boundaries. For example, Kamaya and Itakura [116] generated a 3D polycrystalline body with Voronoi tessellation to study intergranular crack initiation and propagation, as well as

the stress concentration around the cracks.

It merits notice that Voronoi tessellation is used to describe polycrystalline solids is under the following assumptions [117]:

1. Grain growth starts at all points P_i in a finite set of nuclei $\mathbf{V}_i$ (referred to as 'seed point') at the same time. The nuclei are fixed at their spatial position during the growth process, i.e. they do not move.
2. Isotropic and uniform grain growth. Particularly, the velocity of the grain growth is assumed to be equal in
   (a) all grains and
   (b) all directions.
3. Grain growth in a direction stops as two grain boundaries contact each other, i.e. there is no grain overlapping. The growth process stops, if there is no further grain growth in any direction in any grain.
4. There are no voids, i.e. the entire volume is populated by grains.

3.4.2 Governing Equation for Polycrystalline Fe-Cr Alloy with Oxide

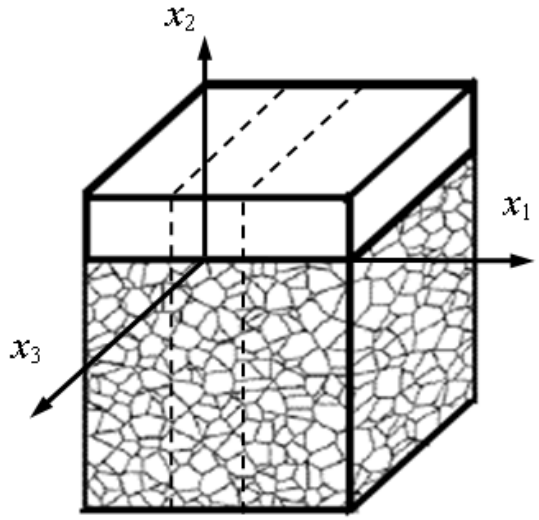

(a)

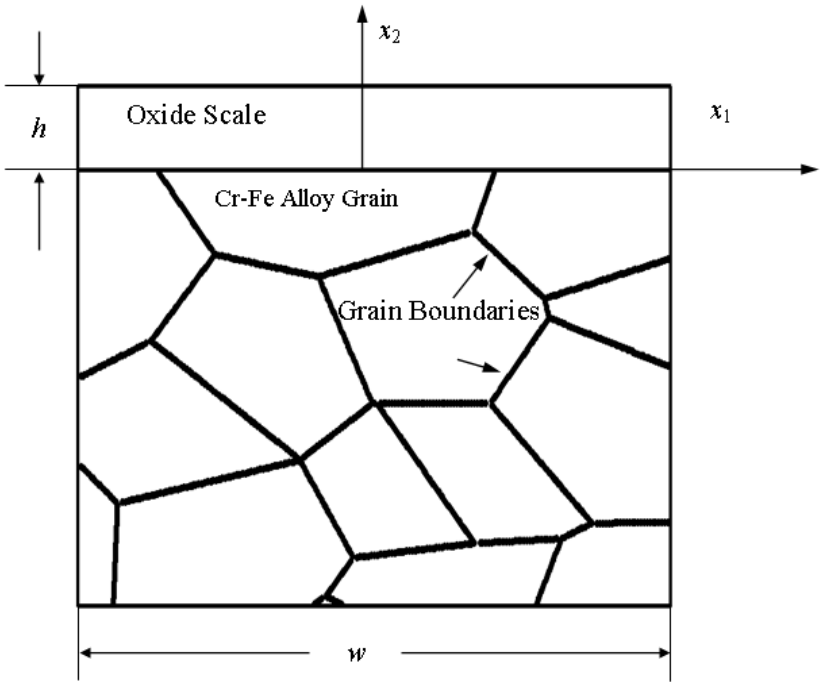

(b)

Figure 3.11 a) 3D Structure of polycrystalline alloy carrying a layer of oxide.b) 2D Structure of polycrystalline alloy carrying a layer of oxide.

Figure 3.11 (a) illustrates the geometry of a polycrystalline alloy carrying an initial Cr_2O_3 at its top surface. The 2D model (Figure 3.11 (b)) studied in this section is a piece of sample cut between the dashed line as shown in Figure 3.11 (a). The oxide scale is assumed to be homogeneous and isotropic with an initial thickness. Both figures are only for illustration purpose and are not to scale.

Interfacial voiding in the alloy is an ineluctable phenomenon accompanying the selective oxidation process from the very beginning. However, it might take a relatively long time of oxidation for the voids to grow to a size such that they could become harmful to the oxide-alloy adherence, such as spallation. In this study, we assume that a steady state of oxidation has been reached before voiding becomes harmful at oxide/alloy interface. So we only focus on steady state oxidation in this study. It should be noted here that steady state oxidation does not imply time independence. For oxidation kinetics, steady state means that the relationship between oxide thickness and time obeys the parabolic law, this has been well acknowledged since Wagner [118].

Even though it was assumed that oxide formation can occur all over the oxide, the 1-D example in section 3.3 shows that when oxidation kinetics reaches steady state, the oxide only forms at the surface (oxide/oxygen phase boundary), which, is consistent with the assumption of many classical approaches [81, 107, 118-119]. Based on this result, we assume that chemical equilibrium is established between reactants (cations and anions) and product (oxide) inside the oxide bulk. Therefore, below the reaction active surface, there is no dramatic strain increase due

to increase of lattice sites in the oxide. Hence, the small deformation assumption can be applied to the model in section 3.1 instead of the finite deformation in order to reduce the calculation complexities.

From [119], the deformation and defect concentration throughout the oxide scale layer and alloy substrate can be solved from the corresponding governing partial differential equations with proper continuity conditions. For the two dimensional model in the current study, the equilibrium equations

$$\begin{aligned} \frac{\partial \sigma_{11}}{\partial x_1} + \frac{\partial \sigma_{12}}{\partial x_2} = 0, \\ \frac{\partial \sigma_{21}}{\partial x_2} + \frac{\partial \sigma_{22}}{\partial x_1} = 0, \end{aligned} \tag{3.39}$$

have to be satisfied both in the oxide and in the alloy substrate. The mass continuity equations for Cr and O ions in the oxide scale are given as

$$\begin{aligned} \frac{\partial c_{\mathrm{Cr}}}{\partial t} &= D_{Cr}\left[\frac{\partial}{\partial x_1}\left(\frac{\partial c_{Cr}}{\partial x_1} + c_{Cr}\frac{V_{Cr}^m}{RT}\frac{\partial \tau_{Cr}}{\partial x_1}\right) + \frac{\partial}{\partial x_2}\left(\frac{\partial c_{Cr}}{\partial x_2} + c_{Cr}\frac{V_{Cr}^m}{RT}\frac{\partial \tau_{Cr}}{\partial x_2}\right)\right], \\ \frac{\partial c_{\mathrm{O}}}{\partial t} &= D_{O}\left[\frac{\partial}{\partial x_1}\left(\frac{\partial c_{O}}{\partial x_1} + c_{O}\frac{V_{O}^m}{RT}\frac{\partial \tau_{O}}{\partial x_1}\right) + \frac{\partial}{\partial x_2}\left(\frac{\partial c_{O}}{\partial x_2} + c_{O}\frac{V_{O}^m}{RT}\frac{\partial \tau_{O}}{\partial x_2}\right)\right], \end{aligned} \tag{3.40}$$

and for Cr atoms in the alloy substrate

$$\begin{aligned} \frac{\partial c_{\mathrm{Cr(a)}}}{\partial t} = D_{Cr(a)}\Bigg[&\frac{\partial}{\partial x_1}\left(\frac{\partial c_{Cr(a)}}{\partial x_1} + c_{Cr(a)}\frac{V_{Cr(a)}^m}{RT}\frac{\partial \tau_{Cr(a)}}{\partial x_1}\right) \\ &+ \frac{\partial}{\partial x_2}\left(\frac{\partial c_{Cr(a)}}{\partial x_2} + c_{Cr(a)}\frac{V_{Cr(a)}^m}{RT}\frac{\partial \tau_{Cr(a)}}{\partial x_2}\right)\Bigg], \end{aligned} \tag{3.41}$$

where D_s is the diffusivity of species s in corresponding diffusion media (s =Cr, O in oxide, s=$\mathrm{Cr_{(a)}}$ in alloy).

With the chemical reaction equilibrium assumption, we have

$$d\mu_p - 2d\mu_{\mathrm{Cr}} - 3d\mu_{\mathrm{O}} = 0, \tag{3.42}$$

where μ_{Cr}, μ_{O} and μ_p are, respectively, the chemical potentials of Cr and O ion, as well the product Cr_2O_3

Since the alloy grains and grain boundaries are randomly distributed and oriented, the material we studied in the model is assumed to be isotropic. So the non-zero stress and elastic strain components are given as

$$\begin{aligned}
\sigma_{11} &= \frac{E}{(1+\nu)(1-2\nu)}\left[(1-\nu)\left(\frac{\partial u_1}{\partial x_1}-\sum_s \eta_s \Delta c_s\right)+\nu\left(\frac{\partial u_2}{\partial x_2}-2\sum_s \eta_s \Delta c_s\right)\right],\\
\sigma_{22} &= \frac{E}{(1+\nu)(1-2\nu)}\left[(1-\nu)\left(\frac{\partial u_2}{\partial x_2}-\sum_s \eta_s \Delta c_s\right)+\nu\left(\frac{\partial u_1}{\partial x_1}-2\sum_s \eta_s \Delta c_s\right)\right],\\
\sigma_{33} &= \frac{E}{(1+\nu)(1-2\nu)}\left[(1-\nu)\left(-\sum_s \eta_s \Delta c_s\right)+\nu\left(\frac{\partial u_2}{\partial x_2}-\sum_s \eta_s \Delta c_s\right)\right.\\
&\qquad \left.+\nu\left(\frac{\partial u_1}{\partial x_1}-\sum_s \eta_s \Delta c_s\right)\right],\\
\sigma_{12} &= \frac{E}{2(1+\nu)}\left(\frac{\partial u_1}{\partial x_2}+\frac{\partial u_2}{\partial x_1}\right)
\end{aligned} \tag{3.43}$$

and

$$\begin{aligned}
\varepsilon_{11}^E &= \frac{\partial u_1}{\partial x_1}-\sum_s \eta_s \Delta c_s,\\
\varepsilon_{22}^E &= \frac{\partial u_1}{\partial x_2}-\sum_s \eta_s \Delta c_s,\\
\varepsilon_{33}^E &= -\sum_s \eta_s \Delta c_s,\\
\varepsilon_{12}^E &= \frac{1}{2}\left(\frac{\partial u_1}{\partial x_2}+\frac{\partial u_2}{\partial x_1}\right).
\end{aligned} \tag{3.44}$$

In addition to the governing equations above, interface conditions need to be specified. In the structure shown in Figure 3.11 (b), there are two interfaces, the metal-scale interface and the scale-air interface. At these interfaces, the following conditions must be satisfied: (a) mass flux continuity of each species, (b) continuity of chemical potential of each species for the adsorption and ionization reaction, respectively, (c) continuity of displacement and (e) continuity of traction.

These conditions are described below.

Metal-Scale Interface ($x_2 = 0$)

At the metal-scale interface, the ionization of Cr atoms is assumed to be an equilibrium process. Thus, the continuity of chemical potentials must hold between Cr ions and Cr atoms, i.e.

$$\frac{\mu^0_{\mathrm{Cr}(a)} - \mu^0_{\mathrm{Cr}}}{RT} + \ln\frac{c_{\mathrm{Cr}(a)}}{c_{\mathrm{Cr}}} = \frac{V^m_{Cr}\tau_{Cr} - V^m_{Cr(a)}\tau_{Cr(a)}}{RT} . \tag{3.45}$$

Conservation of mass for Cr across the interface leads to

$$\frac{\partial c_{\mathrm{Cr}(a)}}{\partial x_2} + \frac{V^m_{Cr(a)}c_{\mathrm{Cr}(a)}}{RT}\frac{\partial \tau_{Cr(a)}}{\partial x_2} = \frac{D_{\mathrm{Cr}}}{D_{\mathrm{Cr}(a)}}\left[\frac{\partial c_{\mathrm{Cr}}}{\partial x_2} + \frac{V^m_{Cr}c_{\mathrm{Cr}}}{RT}\frac{\partial \tau_{Cr}}{\partial x_2}\right] . \tag{3.46}$$

Furthermore, per the assumption that no O can cross the interface into the metal

$$\frac{\partial c_O}{\partial x_2} + \frac{V^m_O c_O}{RT}\frac{\partial \tau_O}{\partial x_2} = 0 . \tag{3.47}$$

Finally, traction continuity is automatically satisfied by the choice of stress components, and the continuity of displacement leads to

$$u_1\big|_{x_2=0^+} = u_1\big|_{x_2=0^-}, u_2\big|_{x_2=0^+} = u_2\big|_{x_2=0^-} . \tag{3.48}$$

At the Scale-Air Interface ($x_2 = h$)

At the scale-air interface, an equilibrium condition is assumed for ionization of oxygen (in the air), i.e.,

$$\frac{1}{2RT}\mu^0_{\mathrm{O}_2} + \ln P^{1/2}_{\mathrm{O}_2} = \frac{\mu^0_{\mathrm{O}}}{RT} + \ln c_{\mathrm{O}} + V^m_O\tau_O . \tag{3.49}$$

where $\mu^0_{\mathrm{O}_2}$ is the standard chemical potential of oxygen gas and P_{O_2} is the oxygen

partial pressure in the air. In addition, since the oxide forms at the surface and Cr ions cannot leave the scale, the Cr ion flux causes all to transform to oxide and to follow the Stefan [107] condition at the scale-air interface, i.e.,

$$\frac{V_p^m}{2} D_{Cr} \left(\frac{\partial c_{\mathrm{Cr}}}{\partial x_2} + \frac{V_{Cr}^m c_{\mathrm{Cr}}}{RT} \frac{\partial \tau_{Cr}}{\partial x_2} \right) = -\frac{du_2}{dt} . \tag{3.50}$$

Furthermore, it is assumed that, in comparison with the stresses in the scale layer, the atmospheric pressure is negligible in typical applications. Thus, the scale-air interface can be viewed as a traction free surface which is satisfied by the choice of the stress components.

Inside the alloy far from the interface, $c_{Cr(a)} = C$ as $x_2 \to -\infty$. Additionally, periodic boundaries are applied at the left ($x_1 = -\frac{w}{2}$) and right ($x_1 = \frac{w}{2}$) hand side of the 2D model, i.e.,

$$\begin{aligned} & u_1\big|_{x_1=-\frac{w}{2}} = u_1\big|_{x_1=\frac{w}{2}}, u_2\big|_{x_1=-\frac{w}{2}} = u_2\big|_{x_1=\frac{w}{2}} \\ & c_{Cr}\big|_{x_1=-\frac{w}{2}} = c_{Cr}\big|_{x_1=\frac{w}{2}}, c_O\big|_{x_1=-\frac{w}{2}} = c_O\big|_{x_1=\frac{w}{2}}, c_{Cr(a)}\big|_{x_1=-\frac{w}{2}} = c_{Cr(a)}\big|_{x_1=\frac{w}{2}} \end{aligned} . \tag{3.51}$$

This stress-diffusion coupled model for steady state oxidation of 16 % (wt) Fe-Cr alloy was implemented with a user-defined element subroutine in the commercial finite elements modeling software ABAQUS. The material properties of 16% (wt) Fe-Cr alloy and its oxide used in the numerical simulation are listed in Table 3.1. Oxygen partial pressure is set to be 0.3 atm at the air-oxide interface. Elements in the alloy part are divided into sets of grains and grain boundaries based on the Random Voronoi tessellation diagram. Elements beyond the oxide/alloy interface are grouped into two sets, the oxide and the air, which are separated by the oxide/gas

surface. These elements are prepared with fine mesh and identical thickness in the x_2 direction. The oxide scale surface movement is calculated by integrating equation (3.50). When the displacement at the oxide surface layer exceeds the specified element thickness, the material properties of the upper layer of elements at the air side switch from those for air to those for oxide.

3.4.3. Results and discussion

The results of the oxidation kinetics are shown in Figure 3.12 for the purpose of validating the models. Changes of oxide scale thickness versus normalized sample width at different time are plotted in Figure 3.12 (a). As can be seen, the top surface of oxidation is flat. From the thickness strategy in the last section, this means that the local thickness difference is less than the thickness of an element in the x_2 direction. So we may approximately consider the oxide with a uniform thickness. A comparison the numerical prediction and the experimental results [108] at steady state, given in Figure 3.12 (b), shows that the prediction and the results agree with each other very well, which shows that this model with small deformation assumption is valid.

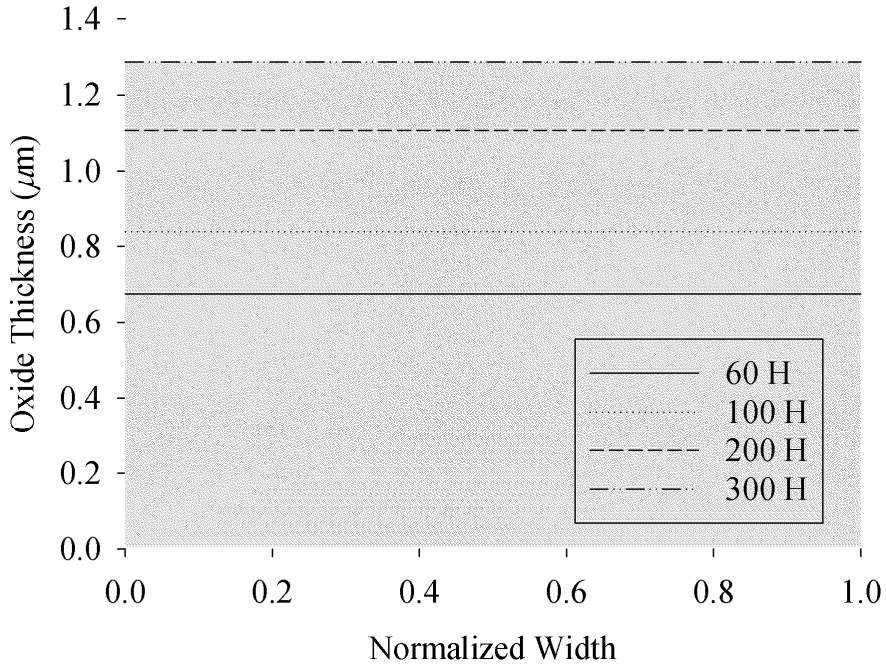

(a)

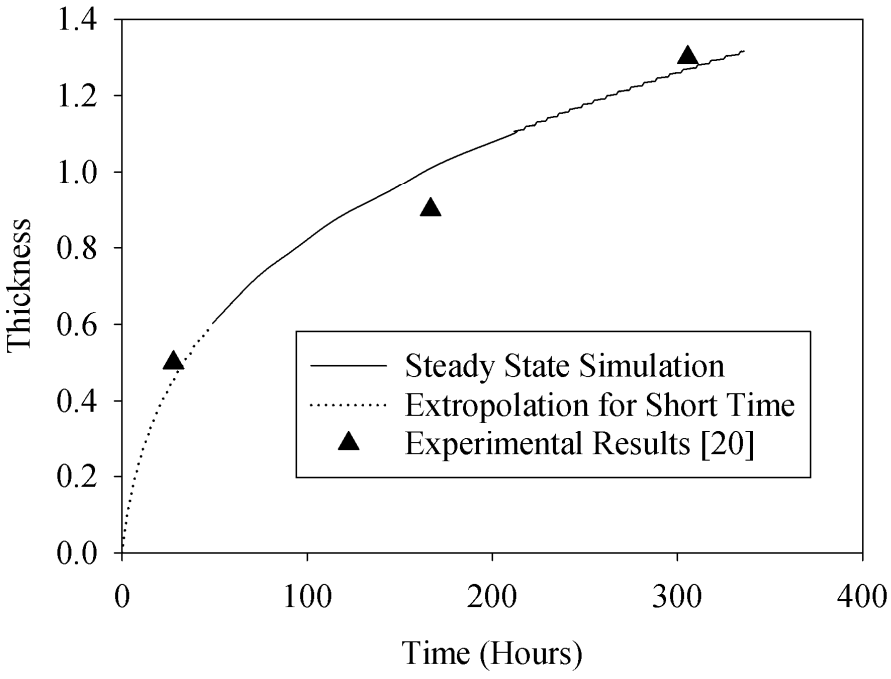

(b)

Figure 3.12 a) Growth of oxide thickness with time in 2D. b) Comparison of growth of oxide between simulation and experiment results.

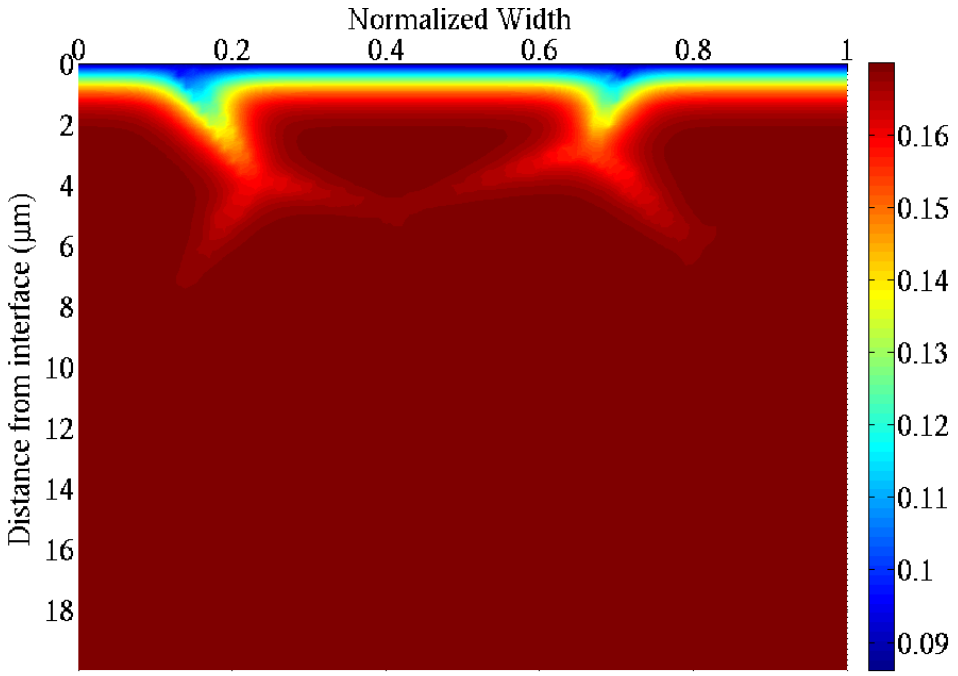

Figure 3.13 Contour of Cr concentration in the alloy after the oxidation time of 200 hours.

Under many circumstances, spallation of Cr_2O_3 scale starts with depletion of the Cr metal oxide/alloy interface. A faster rate of Cr diffusion in the oxide than in the binary alloy is the mechanism to explain this phenomenon. Figure 3.13 shows the contours of Cr concentration in the alloy after the oxidation time of 200 hours. The negative value of the x_2 axis represents the distance below the metal-oxide interface where the coordinate origin is locateed. A decrease in Cr concentration at the alloy side of the interface is observed and the most dramatic change of Cr content is located at the two grain boundary areas. Since the grain

boundary diffusivities are over 2 orders higher than those of the grain bulk, Cr atoms move more easily in grain boundaries. Hence the movements of Cr atoms from alloy grain boundaries leads to lower local concentration. Accordingly, in the oxide, higher Cr ion concentration could be located at the areas adjacent to the alloy grain boundaries (Figure 3.14). Depletion of Cr at the grain not only reduces the local mass density of the alloy, but enables the generation of other lower density products. For example, oxidation of low Cr content Fe-Cr alloy would leave an Fe containing product (e. g. $(Fe,Cr)_3O_4$), which could lead to a loose and incompact oxide layer and which would consequently be easy to peel off and decompose.

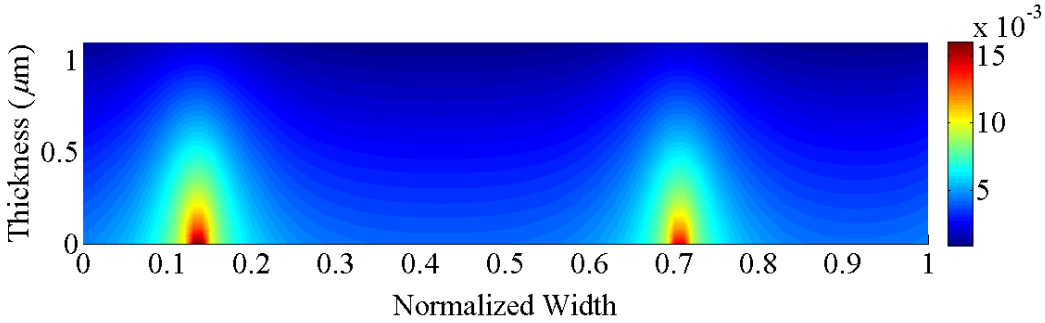

Figure 3.14 Contour of Cr concentration in the oxide after the oxidation time of 200 hours.

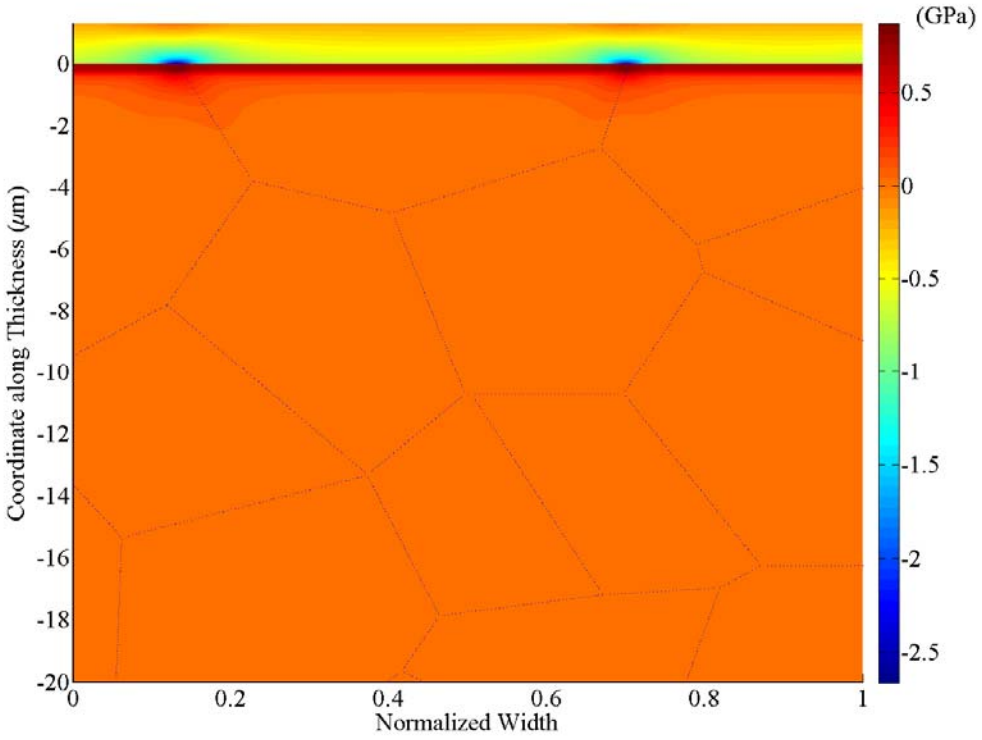

Figure 3.15 Contour of in-plane stress σ_{11} in oxide and alloy after 200 hours of oxidation.

Stresses generated due to changes of species concentration are important driven forces that cause interfacial failure. Figure 3.15 shows the contours of in plane stress σ_{11} in oxide and alloy after 200 hours of oxidation. It can be seen that compressive in-plane stresses are generated in most areas of the oxide and reach their maximum value adjacent to the alloy grain boundary. Relatively high local Cr ion concentrations at these areas allow more product generation under equilibrium conditions and hence induce large deformations and stresses. Another consequence of these local deformations is that tensile deformations are observed right above these

high compressive stress areas. Tensile in-plane stresses are all over the alloy with highest values reached at the grain boundary due to maximum depletion.

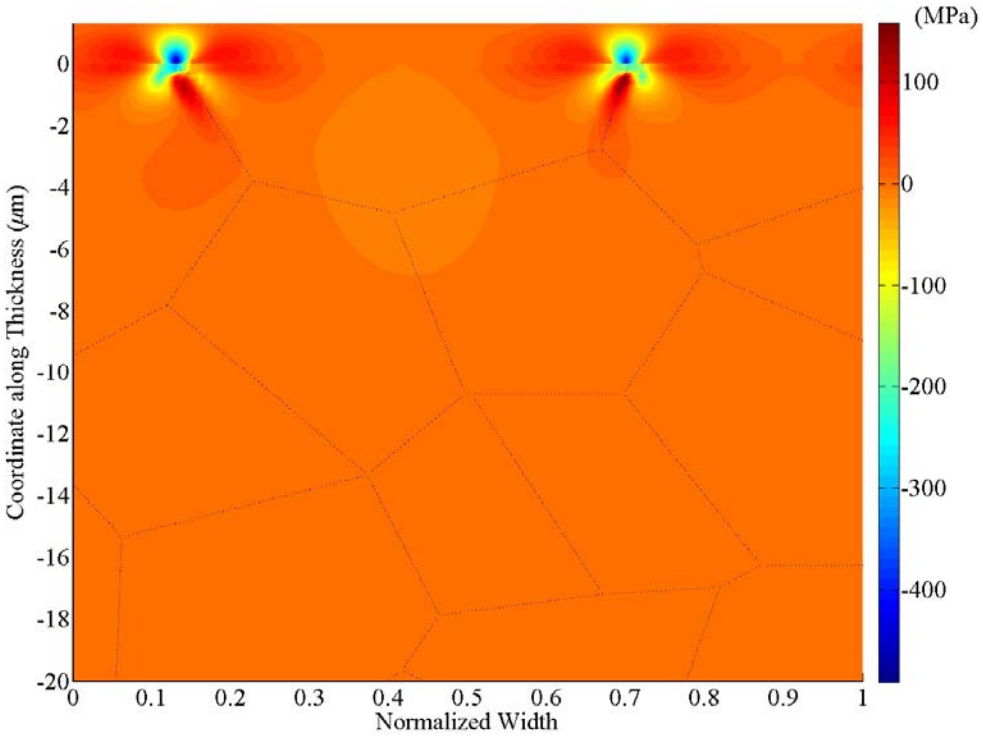

Figure 3.16 Contour of normal stress σ_{22} in oxide and alloy after 200 hours of oxidation.

If spallation is caused by nucleation and propagation of microcracks within the oxide or at the interface, the normal stress σ_{22} could play a critical role. Figure 3.16 shows the normal stresses σ_{22} in oxide and alloy after 100 hours of oxidation. Normal tensile stress of hundred MPa level can be found on both sides of

the high compressive area around the oxide/alloy interface. At the alloy side, both tensile stresses and compressive stresses are found right below the interface.

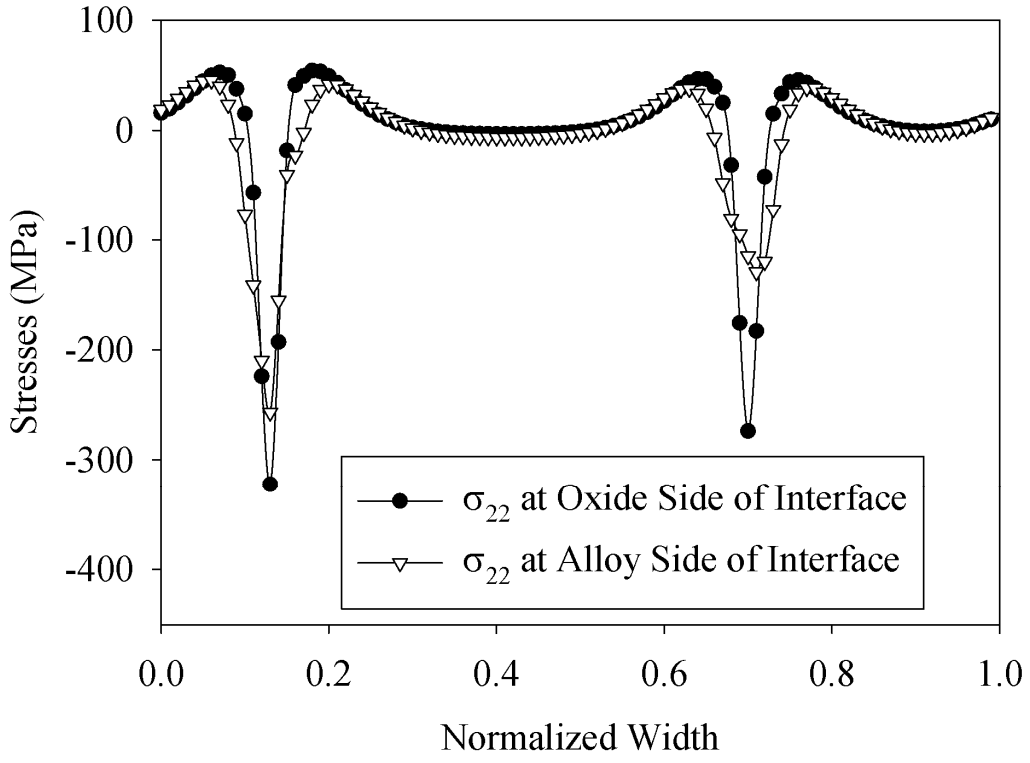

Figure 3.17 Normal Stresses σ_{22} at metal-oxide interface.

The origin for compressive stresses may be the expansion of oxide at the interface, forcing the contacted alloy to deform compressively. Corresponding normal stresses along the oxide/alloy interface are plotted in Figure 3.17 for the purpose of illustration. Even though the tensile stresses are of lower magnitude than the compressive stresses, they affect more interface areas. Once depletion induces voids

and microcracks, these nearby tensile stresses could be the driven forces that assist their propagation. In Figure 3.16, a high tensile-stress concentration can be found at the grain boundaries such that depletion could get expedited there. It has been pointed out [95] that tensile stresses are the causes of void nucleation by triaxiality. Furthermore, high tensile stresses may even induce peel off of the whole grain. This may be one of the answers to the generation of dent areas, including voiding in grain boundaries, along the oxide/alloy interface [26].

The contours of oxygen ion distribution in the oxide are shown in Figure 3.18. The tiny non-uniform distribution in the x_1 direction is believed to be the consequence of the distribution of oxidation induced stresses. An interesting phenomenon is shown in Figure 3.19 which gives the concentration of oxygen ions along the x_1 direction versus different locations along the thickness. The concentration at areas adjacent to alloy grain boundaries increases fast and quickly rises higher than other areas, and accompanying the oxidation process, increases of oxygen ions at these areas switch to a slow rate and eventually lower than those at other areas. Comparing these observations with the stress distribution shown in Figure 3.15 and Figure 3.16, we found that the magnitude of the stress gradient affects the ionic diffusion on stresses, which, is consistent with the conclusions of Stephenson [59].

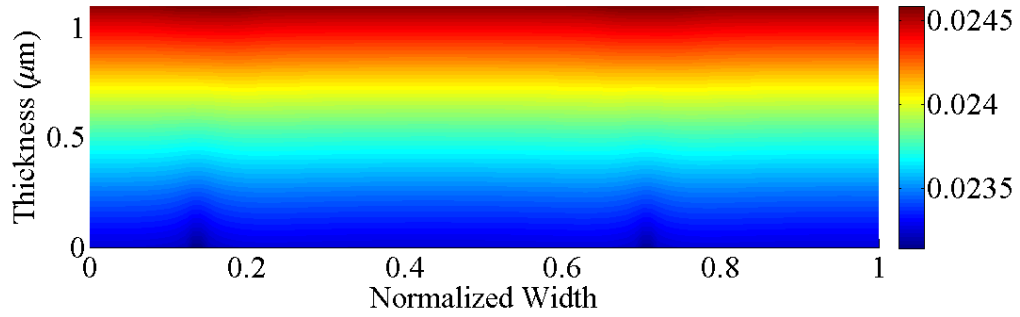

Figure 3.18 Contour of oxygen ion distribution in the oxide.

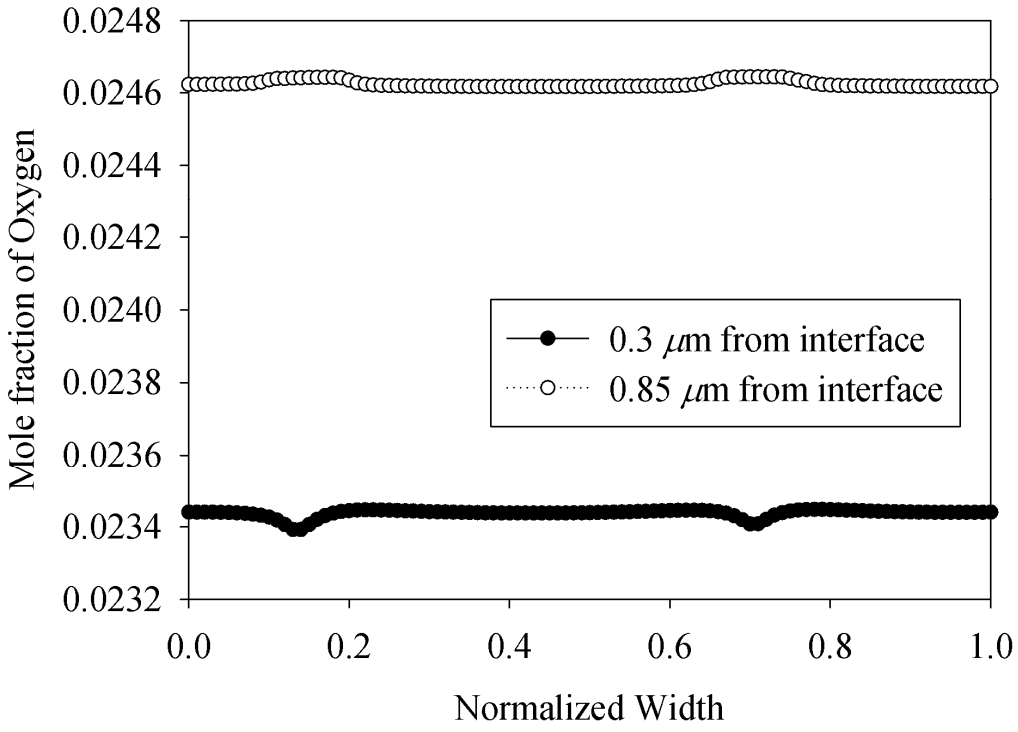

Figure 3.19 the concentration of oxygen ions along x_1 direction versus different locations along thickness.

3.5. Summary

In this chapter, a continuum thermodynamic model is developed to account for stress-diffusion interaction in the oxidation of Fe-Cr alloys. In comparison with other existing models, the present approach is formulated in the Eulerian framework. One of the advantages of the Eulerian formulation is to allow the oxide lattice to "flow" upward, avoiding the complexity of computing the velocities of metal-scale and scale-air interfaces and greatly simplifying the equations and the numerical solution. Another important advance is the use of a fully coupled theory [36] relating chemical reaction and mechanical stress, namely not only does oxidation induce stress, but in return stress also affects the rate of oxidation. In this fully coupled theory, not only the hydrostatic stress, but also the deviatoric stress needs to be considered. The model provides detailed distribution of stresses in the scale layer, as well as concentration distributions of all diffusing species in the system. The model results provide clear insight into the oxidation mechanisms and how the stress affects the diffusion and oxidation process. It is found that the distribution of stress and the concentration of diffusible species can be scaled by the oxidation reaction rate constant. This means that, with proper scaling, the numerical results in the dimensionless form can be used for any value of the reaction rate. It should also be pointed out that, although it is developed based on a Fe-Cr alloy, the present model can be easily extended to many different types of binary alloys.

A 2D finite element implementation of this continuum thermodynamic model in the oxidation of Fe-Cr alloys was presented in this chapter for the understanding of the origin of the interfacial failure. The Voronoi tessellation diagram is employed to reflect the real effect mass diffusion among alloy grains and grain

boundaries. The advantage of the stress-diffusion coupling model is to provide a detailed distribution of stresses, as well as concentration distributions of all diffusing species in the system. Therefore, the presented results provide clear insight into spallation initiating mechanisms and how ionic diffusion affects the stress distributions. The results also confirm the experimental outcomes by predicting the Cr depletion at alloy boundaries right below the metal-oxide interface. As a consequence of this, normal tensile stresses are generated at both the metal-oxide interface and the alloy grain boundaries. It is believed that those stresses are among the important driving forces for oxide spallation.

CHAPTER 4 THE REACTIVE ELEMENT EFFECT ON DIFFUSIVITY MODIFUCATION

4.1 Introduction

Chromia-forming high temperature alloys have been widely used in industrial applications. An industrial thermal treatment for these materials is commonly used to form the corrosion resistant chromia layer outside the alloys in order to protect the alloys from further oxidation. Though the chromia scales protect the alloy well in various corrosion circumstances, failures such as spallation or cracking may occur. On the other hand, numerous experimental results [76, 120-123] have shown that the addition of reactive elements such as yttrium (Y) or cerium (Ce) can remarkably change the oxidation performance of chromia scales. Polman et al.[80] summarized the beneficial effects of reactive elements as: (1) The amount of chromium necessary to form a continuous chromia layer, can be reduced; (2) the overall oxidation rate is decreased; (3) the oxide scale is more adherent and less oxide spallation occurs.

Though the aforementioned effects have been observed since the 1940s, the mechanisms behind the phenomena have been unclear until recent decades. Advanced experimental analytical techniques such as secondary ion mass spectrometry (SIMS) helped to characterize these reactive element effects. It has been suggested that when a reactive element such as yttrium is present in the chromia layer [7] : (1) yttrium is

segregated out of the oxide grains and stays along the grain boundaries, oxide surfaces and alloy-oxide interfaces; (2) The segregated yttrium acts as a barrier at the grain boundaries such that the outward diffusion of cations is drastically suppressed. To data, only a few works have studied the quantitative modeling of reactive element effects. Based on the classic Fick's first law, Liu et al. [81] establish a 1-D model for growth of yttrium doped $\alpha - Al_2O_3$ by relating the oxidation kinetics to inward oxygen diffusion and oxide grain coarsening. More recently, Nijdam et al. [31] proposed a 2-D model to describe the growth kinetics of a protective oxide scale containing reactive element oxide inclusions. For a given reactive element content, their model can calculate the alloy grain size, the size of reactive element containing intermetallic precipitates in the alloy, the parabolic rate constant of the protective scale, the size and distribution of the inclusions in the scale as well as the total oxide scale kinetics. However, all the existing models focus exclusively on the description of the reactive element effect on the oxide scale kinetics; the effects on oxide-scale adhesion and spallation resistance have rarely been discussed at the quantitative level.

On the other hand, residual stresses, especially those of chemical origin [8, 16, 124] are believed to be among the driving forces that cause oxide layer spall off. Some attempts have been made to develop computational models to describe the oxidation-stress interaction process [2, 55, 125]. Most of the existing models are based on the original concept of Rhines and Wolf [8]. Clarke [55] considered the generation of lateral growth strain in response to the counter-diffusion of cations and anions. By neglecting stress relaxation, Clarke showed that the lateral growth strain

rate is proportional to the outward cation flux. Under a steady-state condition, Limarga et al. [2] derived the average growth stress by assuming that inward oxygen diffusion occurs along grain boundaries. Pieraggi and Rapp [120] proposed that the origin of stresses is the presence of misfit dislocation and misorientation dislocation at scale/alloy interface. It is believed that the reactive elements pin the interfacial misfit dislocations to inhibit the cationic controlled kinetics as well as to avoid the growth stresses. In chapter 3, we presented a more general model describing the stress distribution in the oxide scale which formulated a continuum framework to predict the spatial distribution of stress and concentrations within the oxide scale based on the work of Wu [64] and Swaminathan [36]. Wu's work has been extended by El Kadiri [95] with the consideration of alloy plasticity as a realization of the ideas from Pieraggi and Rapp [17]. In all these works, the stresses affect internal oxidation by changing the free energy of the reaction, and they affect diffusion by modifying the chemical potential. These allow the authors to consider how the stress interact with the internal oxidation in a thermodynamically and kinetically consistent manner.

In the present study, a 2-D generalized stress-diffusion coupling model specifically addresses the effects of yttrium on oxide-alloy interfacial spallation driving forces by taking in to account the yttrium-affected Chromium ion diffusivity. In the following paragraphs, the theoretical framework will be first given in section 4.2. Following this, the results from finite element computation as well as discussions will be presented in section 4.3. Finally, conclusions will be given in section 4.4.

4. 2. Theoretical Framework

4.2.1 Model of polycrystalline oxide on Fe-Cr alloy

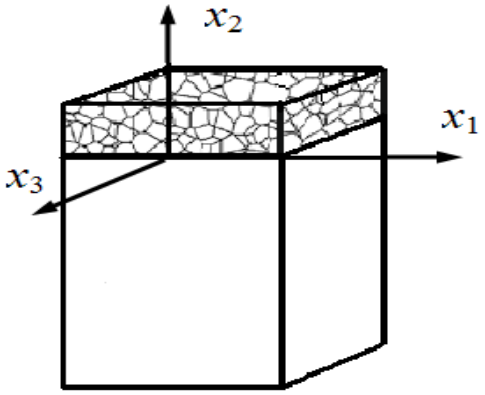

(a)

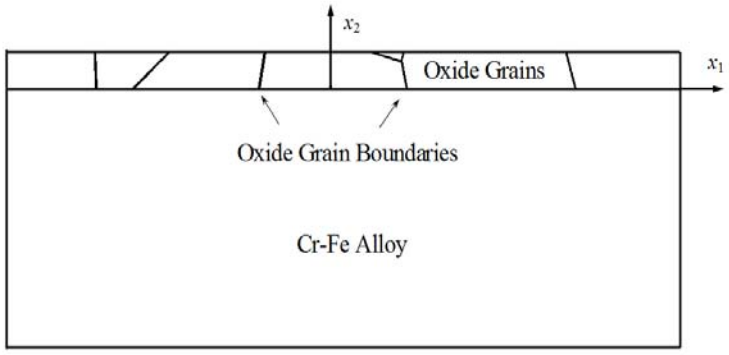

(b)

Figure 4.1 a) 3D Structure of alloy carrying a layer of polycrystalline oxide. b) 2D Structure of alloy carrying a layer of polycrystalline oxide (not to scale).

Figure 4.1 (a) with an x_3 thickness that is considerably large in comparison with the dimensions in the other two directions. The oxide scale is assumed to be homogeneous and isotropic with an initial thickness. Both figures are for illustration

purpose only and are not to scale.

Interfacial voiding in the alloy is an ineluctable phenomenon accompanying the selective oxidation process from the very beginning. However, it takes a relative long time of oxidation for the voids to grow to a size such that they could become harmful to the oxide-alloy adherence, such as spallation. In this study, we assume that a steady state of oxidation has been reached before voiding becomes harmful at oxide/alloy interface. So we only focus on steady state oxidation in this study. It should be noted here that steady state oxidation does not imply time independence. For oxidation kinetics, steady state means that the relationship between oxide thickness and time obeys the parabolic law; this has been well acknowledged since Wagner [118].

Even though it is assumed that oxide formation can occur all over the material, the 1-D example in chapter 3 shows that when oxidation kinetics reaches steady state, the oxide only forms at the surface (oxide/oxygen phase boundary), which is consistent with the assumption of many classical approaches [81, 107, 118]. Based on this result, we assume that a chemical equilibrium is established between reactants (cations and anions) and product (oxide) inside the oxide volume. Therefore, below the reaction active surface, there is no dramatic volume increase in the oxide and alloy. Hence, to reduce the complexities of calculation, the small deformation assumption can be applied to the stress-diffusion interaction model instead of the finite deformation assumption.

From chapter 3, deformation and defect concentration throughout the oxide

scale layer and alloy substrate can be solved from the corresponding governing partial differential equations if the proper continuity boundary conditions are used. For the two dimensional model in the current study, the governing equation used is the same as those listed in section 3.4.2, i.e. equation (3.39)-(3.51).

4.2.2 Impact of yttrium on Cr diffusivity

Experimental evidence [7] has shown that the diffusivities of ionic species have critical roles in the oxidation processes of alloys, and this is also reflected in the current model. For example, in equation (3.50) the scale growth rate is proportional to the diffusivity of Cr ions. It is also well acknowledged that grain boundary areas are short circuits for ionic diffusion. Besides, during growth of the scale, the reactive particles are mostly segregated in the grain boundary areas. Hence the impact of yttrium on the diffusivity of Cr ions mostly occurs there. In this section, the dependence of Cr ion diffusivity on the activity of Y_2O_3 is obtained, mostly focusing on the oxide grain boundary areas.

During the oxidation process of Y-doped alloys, Y_2O_3 is formed at the grain boundaries and further reacts with Cr_2O_3 to form perovskite-type compounds such as $YCrO_3$. The Cr ion is less favorable in $YCrO_3$ and is constrained by the diffusion of yttrium.

The reactions whereby Y_2O_3 dissolves in $YCrO_3$, can be given as

$$Y_2O_3 + \frac{3}{2}O_2 \rightarrow 2V_{Cr}''' + 2Y_{Cr}^{\times} + 6O_O^{\times} + 6h^{\cdot} \qquad (4.1)$$

where the Kroger-Vink notation is adopted. We assume that this reaction reaches equilibrium all over the oxide scale, such that the equilibrium constant $K_{(4.1)}$ is given

as

$$K_{(4.1)} = \frac{\left[V_{Cr}'''\right]^2 \left[Y_{Cr}^{\times}\right]^2 \left[O_O^{\times}\right]^6 \left[h^{\cdot}\right]^6}{a_{Y_2O_3} P_{O_2}^{3/2}} \tag{4.2}$$

where $a_{Y_2O_3}$ is the activity of Y_2O_3. By substituting the electrical neutrality condition

$$3\left[V_{Cr}'''\right] = \left[h^{\cdot}\right] \tag{4.3}$$

into (4.2), we may obtain

$$\left[V_{Cr}'''\right] = \left(\frac{K_{(4.1)}}{3^8 \left[Y_{Cr}^{\times}\right]^2 \left[O_O^{\times}\right]^6}\right)^{1/8} P_{O_2}^{3/16} a_{Y_2O_3}^{1/8}. \tag{4.4}$$

Noting that the variation of the Cr ion is equal to that of the Cr vacancy, as well as that the diffusivities of Cr ion and Cr vacancy are virtually the same, we have

$$D_{Cr}\left(dc_{Cr}\right) = -D_V\left(d\left[V_{Cr}'''\right]\right). \tag{4.5}$$

Integration of equation (4.5) gives

$$D_{Cr}\left(c_{Cr}^0 - c_{Cr}\right) = D_V\left(\left[V_{Cr}'''\right] - 0\right) \tag{4.6}$$

where c_{Cr}^0 is the stoichiometric concentration of Cr in the reaction product. We can immediately have the expression for diffusivity of Cr ions in the grain boundary as

$$D_{Cr} = \frac{D_V}{c_{Cr}^0 - c_{Cr}} \left(\frac{K_{(4.1)}}{3^8 \left[Y_{Cr}^{\times}\right]^2 \left[O_O^{\times}\right]^6}\right)^{1/8} P_{O_2}^{3/16} a_{Y_2O_3}^{1/8}. \tag{4.7}$$

We assume that the diffusivity D_{Cr} is only affected by the yttrium dopant and temperature, and is independent of the chromium ion concentration at the grain boundaries. So here the variation of c_{Cr} in the grain boundary is an average value and

is assumed to be a constant. Hence, $c^d = c^0_{Cr} - c_{Cr}$ is also a constant. A close observation of (4.7) reveals that the part

$$\frac{D_V}{c^d}\left(\frac{\mathrm{K}_{(4.1)}}{3^8\left[\mathrm{Y}^{\times}_{\mathrm{Cr}}\right]^2\left[\mathrm{O}^{\times}_{\mathrm{O}}\right]^6}\right)^{1/8} \tag{4.8}$$

can be grouped together for further convenience. We denote it as C^T, i.e.

$$C^T = \frac{D_V}{c^d}\left(\frac{\mathrm{K}_{(4.1)}}{3^8\left[\mathrm{Y}^{\times}_{\mathrm{Cr}}\right]^2\left[\mathrm{O}^{\times}_{\mathrm{O}}\right]^6}\right)^{1/8}. \tag{4.9}$$

Equation (4.7) is hence given as

$$D_{Cr} = C^T P^{3/16}_{O_2} a^{1/8}_{\mathrm{Y_2O_3}}. \tag{4.10}$$

According to the relation between the parabolic rate constant and the diffusivity of the oxidation rate determining species, and noting that oxidation kinetics is controlled by the grain boundary diffusion, we have

$$k_p = -\frac{f}{RT}\int_{\mu_{Cr(O)}}^{\mu_{Cr(A)}} D_{Cr}\, d\mu_{Cr} \tag{4.11}$$

Substitution of (4.10) into (4.11) leads to

$$k_p = -\frac{f}{RT} C^T P^{3/16}_{O_2}\int_{\mu_{Cr(O)}}^{\mu_{Cr(A)}} a^{1/8}_{\mathrm{Y_2O_3}}\, d\mu_{Cr} \tag{4.12}$$

where the lower and upper integral limits are the chemical potential of the Cr ion at the alloy side and that at the air side of the oxide scale. At the oxide surface, chemical equilibrium for the reaction

$$2\mathrm{Cr} + 3/2\,\mathrm{O_2} \rightarrow \mathrm{Cr_2O_3} \tag{4.13}$$

requires that

$$2\mu_{\mathrm{Cr}} + 3/2\,P_{\mathrm{O_2}} \rightarrow \mu_{\mathrm{Cr_2O_3}}. \tag{4.14}$$

Similarly, the requirement for the reaction

$$Cr_2O_3 + Y_2O_3 \rightarrow 2YCrO_3 \tag{4.15}$$

in oxide leads to

$$\mu_{Cr_2O_3} + \mu_{Y_2O_3} = 2\mu_{YCrO_3} \tag{4.16}$$

Taking derivatives of equations (4.14) and (4.16) with fixed oxygen partial pressure and chemical potential of $YCrO_3$, we have

$$d\mu_{Cr} = 1/2\, d\mu_{Cr_2O_3} = -1/2\, d\mu_{Y_2O_3} = -1/2\left[RTd\left(\ln a_{Y_2O_3}\right) + V^m_{Y_2O_3} d\tau_{Y_2O_3} \right] \tag{4.17}$$

The second term inside the bracket on the right hand side of equation (4.17) is the stress dependent part of the chemical potential of $YCrO_3$. Since the dependence of chromium diffusivity on yttrium content is our primary interest in this study, we ignore the stress impact by eliminating the stress dependent part, i.e., we set

$$d\mu_{Cr} = -1/2\, RTd\left(\ln a_{Y_2O_3}\right) \tag{4.18}$$

After substituting (4.18) into (4.12), we now have

$$\begin{aligned} k_p &= \frac{1}{2} C^T P_{O_2}^{3/16} f \int_{\ln a_{Y_2O_3(O)}}^{\ln a_{Y_2O_3(A)}} a_{Y_2O_3}^{1/8} d\left(\ln a_{Y_2O_3}\right) \\ &= 4C^T P_{O_2}^{3/16} f \left(a_{Y_2O_3(A)}^{1/8} - a_{Y_2O_3(O)}^{1/8} \right) \end{aligned} \tag{4.19}$$

Comparison between (4.10) and (4.19) immediately leads to the following relation

$$D_{Cr} = \frac{k_p a_{Y_2O_3}^{1/8}}{4f\left(a_{Y_2O_3(A)}^{1/8} - a_{Y_2O_3(O)}^{1/8} \right)} = \frac{k_p a_{Y_2O_3}^{1/8}}{4f\Delta a} \tag{4.20}$$

For a given material oxidized under specific oxidation conditions, k_p can always be obtained as a constant. Therefore, according to (4.20) the diffusivity of the Cr ion in oxide is decided by the difference between the activity of Y_2O_3 at the oxide surface and that at the oxide-alloy surface, which is denoted by Δa, as well as the local activity of Y_2O_3.

The upper limit of $a_{Y_2O_3}$ is

$$a^U_{Y_2O_3} = 1. \tag{4.21}$$

From the work of Kawamura et al. [126], when (4.15) reaches equilibrium, the free energy

$$\Delta G^0_{(4.15)} = -14.5\times10^4 + 5.38\times10T \pm 4.2\times10^3 \text{J/mol}. \tag{4.22}$$

Therefore, the possible lower limit of $a_{Y_2O_3}$ could be reached when $a_{Cr_2O_3} = 1$, i.e.

$$a^L_{Y_2O_3} = \exp\left(\frac{\Delta G^0_{(30)}}{RT}\right) \tag{4.23}$$

From (4.21) and (4.23), we can find the upper bound of Δa, which is

$$\Delta a^{ub} = 1 - \exp\left(\frac{\Delta G^0_{(30)}}{RT}\right). \tag{4.24}$$

4.3. Finite Element Implementation

4.3.1 Implementation description

The two dimensional diffusion-stress coupling model for steady state oxidation of a binary alloy was implemented by finite element method in the commercial software ABAQUS with a user defined element subroutine. Emphasis was put on the yttrium effect on scale growth and failure. As shown in

Figure 4.1 (b), a layer of polycrystalline oxide growing on the top of a binary alloy is considered in this implementation. The alloy part is considered as a whole bulk, while elements in the oxide part are divided into sets of grains and grain boundaries based on the random voronoi tessellation diagram. The elements beyond the oxide/alloy interface are modeled with fine mesh and identical thickness in the x_2

direction. The oxide scale surface movment is calculated by integrating equation (3.50). When the displacement at the oxide surface layer exceeds the specified element thickness, the material properties of the upper layer of elements at the air side switch from those for air to oxide.

In the grain boundary areas, the diffusivity model presented in section 4.2.2 is incorporated into the 2-D coupling model to account for the effects of yttrium. All material properties used in this finite element implementation are listed in Table 3.1 and Table 4.1 [7, 127-129]. Finally, in this simulation, all the properties in three material areas (alloy, oxide grains and oxide grain boundaries) are assumed to be homogeneous and isotropic, and the elastic constants of the oxide grains and grain boundaries are assumed to be identical.

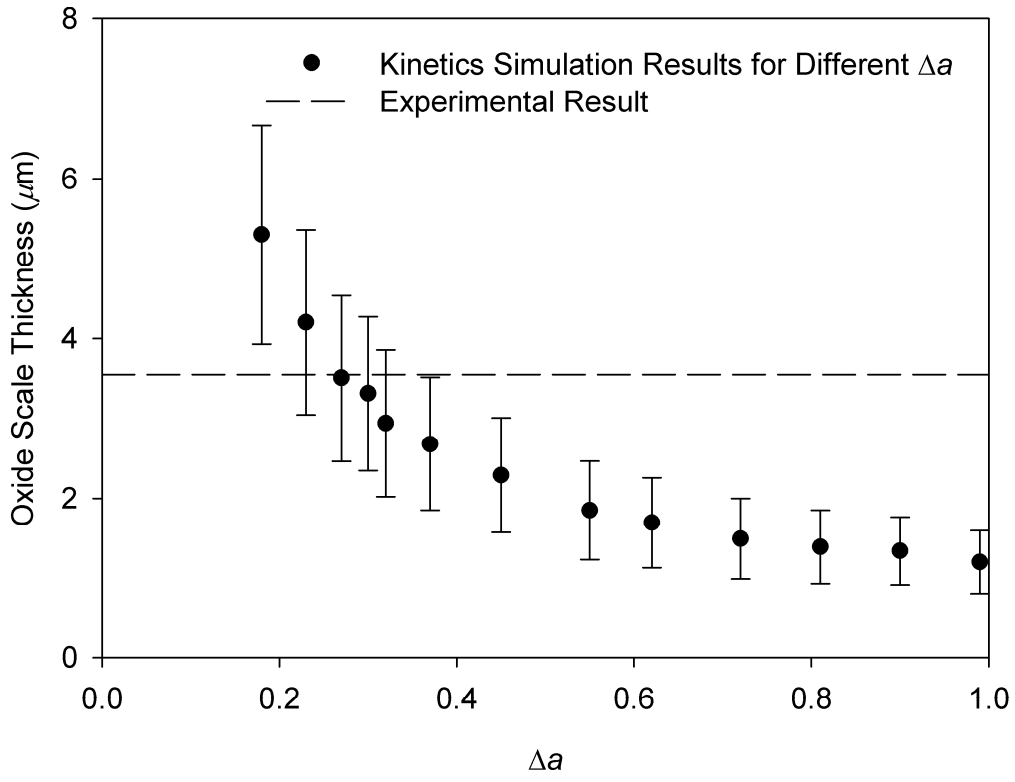

Figure 4.2 relation between Δa and scale thickness

4.3.2 Results and Discussions

The simulation is first carried out for Ni-Cr-Y oxidation at 1000 ^{o}C for validation. The diffusivity of Cr ions in the grain boundaries is first fitted based on the experimental results from the work of Delaunay et al. [130]. According to the oxidation kinetics results of Ni-Cr-Y alloy, when T=1273K, and $P_{O_2} = 1.0$ atm, the parabolic rate constant is $1.70 \times 10^{-11} \text{cm}^2\text{s}^{-1}$. So equation (4.20) implies that under this specific condition, the diffusivity is dependent on Δa and on the possible value of $a_{Y_2O_3}$. Besides, for each Δa value, there are always possible lower and upper bounds for values of $a_{Y_2O_3}$, which means that a specific Δa could lead to a range for

the diffusivities of Cr ion in the oxide grain boundaries. Since the diffusivities of Cr ions are critical to the growth of oxide scale, a range of D_{Cr} would be eventually reflected by a range of scale thickness.

Table 4.1 Additional Material properties for Cr_2O_3

Parabolic rate constant	k_p	4.6×10^{-15} cm^2/s
Diffusivity of Chromium ion	D_{Cr}	in Grain 5.9×10^{-18} cm^2/s, Undoped Alloy 2.4×10^{-18} cm^2/s, Doped Alloy in Grain Boundary 1.1×10^{-12} cm^2/s, Undoped Alloy 2.5×10^{-12} cm^2/s, Doped Alloy
Diffusivity of Oxygen ion	D_O	in Grain 2.6×10^{-18} cm^2/s, Undoped Alloy 8.2×10^{-18} cm^2/s, Doped Alloy in Grain Boundary 5.9×10^{-13} cm^2/s, Undoped Alloy 2.0×10^{-13} cm^2/s, Doped Alloy

Figure 4.2 shows the simulation results for the relation between Δa and the scale thickness under experimental conditions. The dot represents the thickness of scale at given Δa and the error bars stand for the possible thickness range for the corresponding $a_{Y_2O_3}$. The dashed line gives the experimental value of scale thickness, which roughly comes across to the dot corresponding to $\Delta a = 0.27$, with $a_{Y_2O_3} = 0.011$.

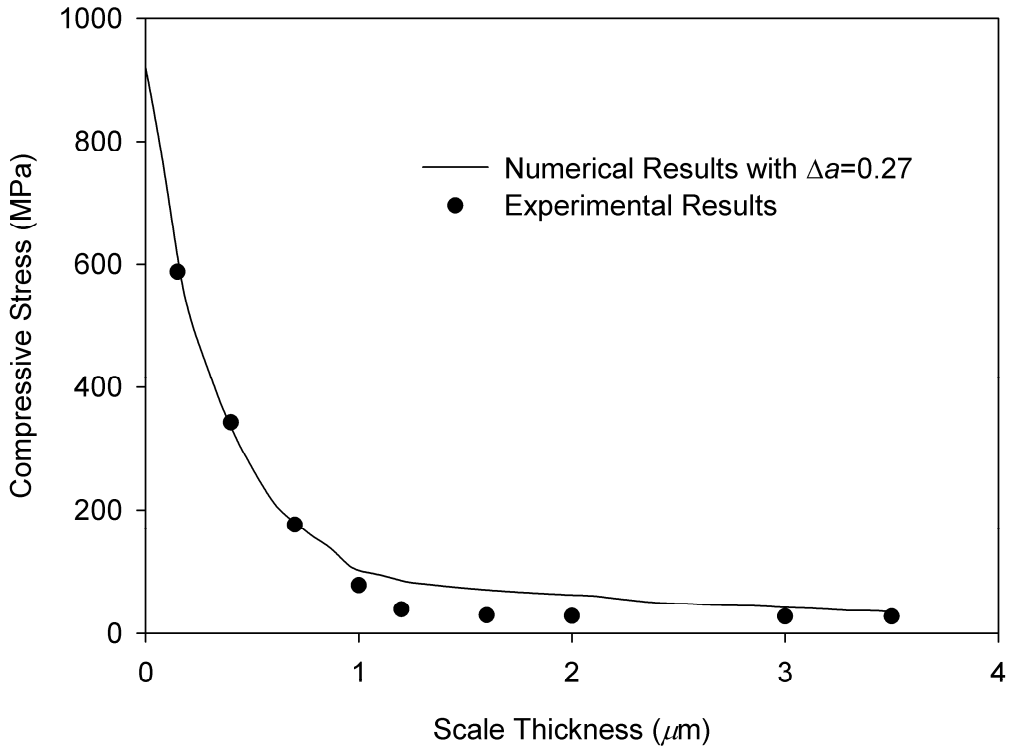

Figure 4.3 Compressive distribution along oxide thickness for Ni-Cr-Y alloy.

With the fitted data, the in-plane compressive stress σ_{11} is calculated and plotted with the experimental results in Figure 4.3. Comparison has shown good agreement between these two groups of results, especially for the results close to the alloy-oxide interface areas.

The model of the Cr ion diffusivity can be validated through comparison with the work of Tsai et al. [7]. According to their work, the diffusivity of Cr ions in grain boundaries at 1073 K is 2.5×10^{-13} $\mathrm{cm^2 s^{-1}}$, which is within the predicted range from (4.20) with $\Delta a = 0.0028$ and $a_{Y_2O_3} = 0.0086$. These data are all adopted in the finite element simulation.

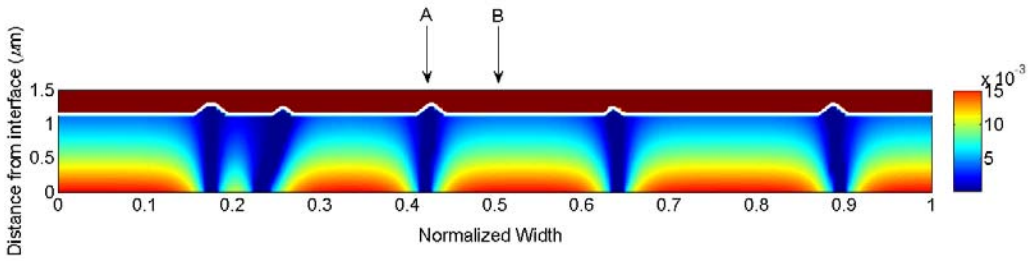

(a)

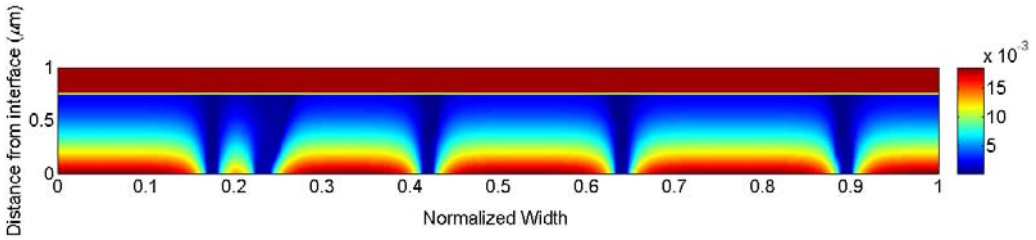

(b)

Figure 4.4 (a) Cr ion distribution in the oxide of pure Fe-Cr alloy; (b) Cr ion distribution in the oxide of yttrium doped Fe-Cr alloy.

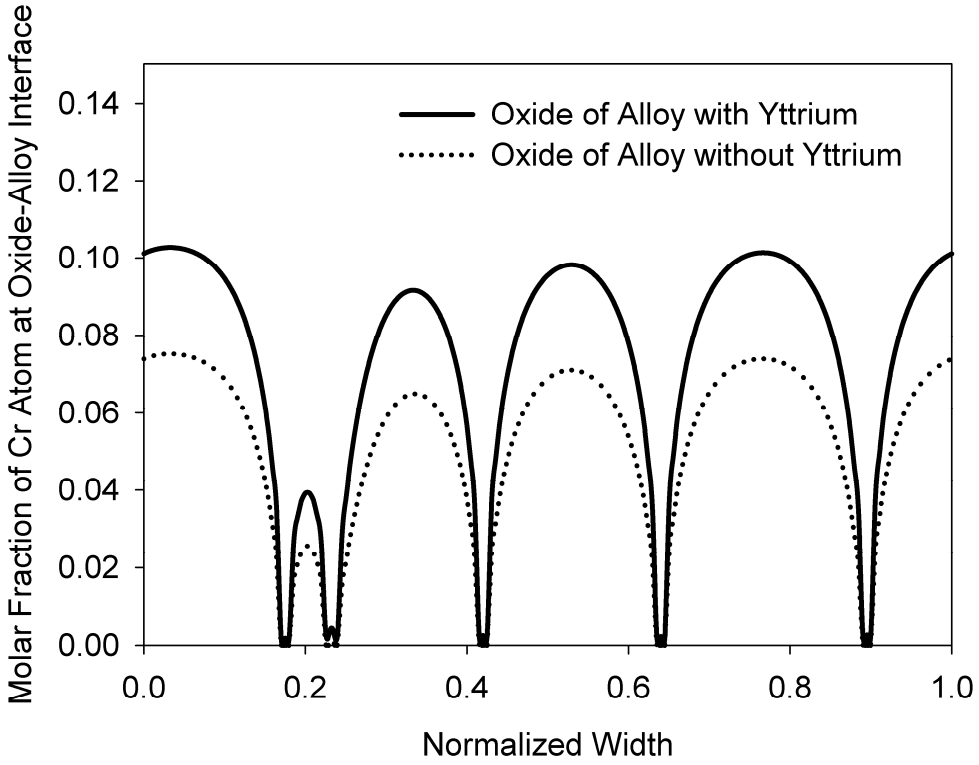

Figure 4.5 Cr atom molar fraction at oxide-alloy interface.

The majority of the present work focuses on the oxidation of Fe-Cr and Fe-Cr-Y alloys at 1073 K. Simulation results show that yttrium plays an important role in the oxidation kinetics of the alloys. The concentration distributions of Cr ions in oxide at 250 hours after the oxidation are shown Figure 4.4. Two important phenomena are observed. First, the concentrations at oxide grain areas is much higher than that at grain boundary areas, which is due to the combination of differences in diffusivities and surface oxide formations. Under the assumption that the oxide forms at the surface at steady state, metal ions are mainly consumed at the top surface; higher diffusivities expedite the movement of ions towards the surface, which

decreases the local metal ion concentration. The same mechanism also explains that the local Cr concentration in oxides from alloys containing dopants is higher than is found in oxides from pure alloy. Second, resource depletion is another factor that affects these results. Figure 4.5 illustrates the Cr atom concentration at the oxide-alloy interface. As can be seen, the higher the diffusivities of materials (oxide of undoped alloy) or areas (grain boundaries) are, the lower the corresponding Cr atom concentration would be. It should be noted here that the Cr atoms at the alloy-oxide interface are the sources of the Cr ions in the oxides. For undoped alloy, when the source concentration depletes rapidly, a low ionic concentration is expected. On the other hand, as shown in Figure 4.5, the addition of yttrium decreases the overall diffusivities of the oxide and results in less interfacial depletion.

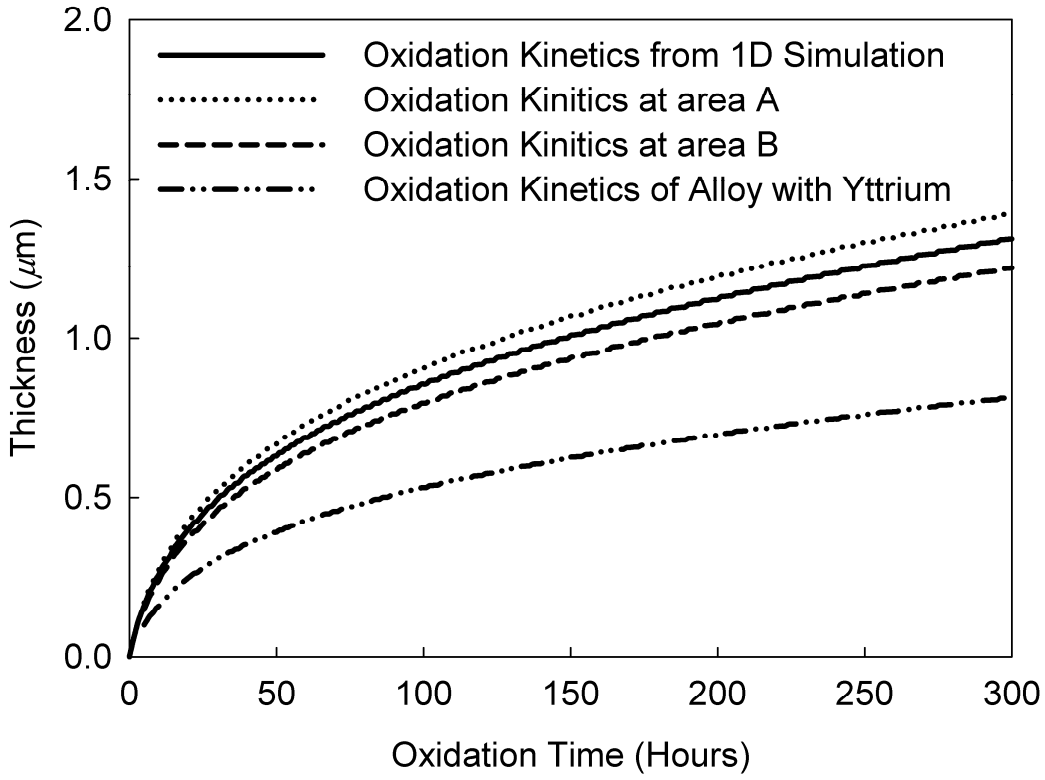

Figure 4.6 Oxidation kinetics.

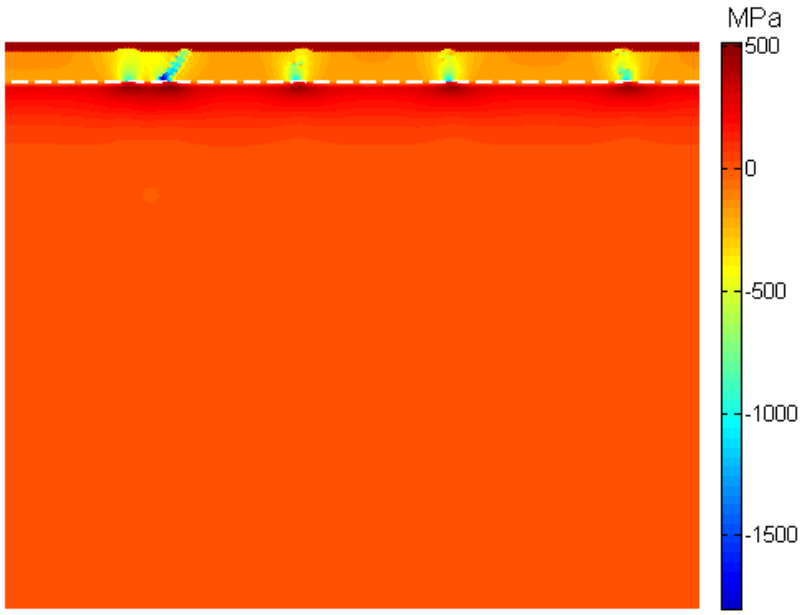

(a)

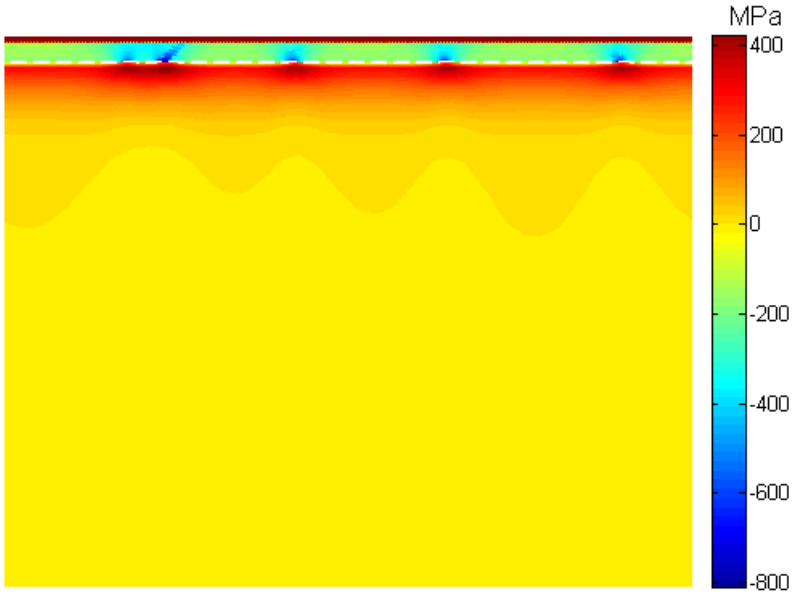

(b)

Figure 4.7 (a) Contour of in-plane stress σ_{11} in oxide and pure alloy after 250 hours of oxidation. (b) Contour of in-plane stress σ_{11} in oxide and yttrium doped alloy after 250 hours of oxidation.

Figure 4.4 also demonstrates the surface morphology differences between the undoped and doped cases. For an oxide of pure alloy (Figure 4.4 (a)), convex oxide surface morphology is observed at the small areas around the grain boundaries, which leads to an uneven oxide surface. Rapid diffusion in grain boundaries, which is 5-6 orders faster than that in grains, could be used to account for this phenomenon. For the oxide of a doped alloy, segregation of yttrium in oxide grain boundaries forms barriers for ionic diffusion and remarkably drags the grain-boundary ion diffusion. As a consequence, such convex morphology is hard to obtain for the oxide of a doped alloy. The results for the oxidation kinetics are shown in Figure 4.6 for the purpose of validating the models. An oxidation kinetics curve from a previous 1D result is plotted here for reference. Two curves of oxidation kinetics are plotted here for pure alloy: one represents the thickness growth around point A and the other shows that around point B. The 1-D results reasonably are located between the those at location A and B, though the average thickness for these two dimensional results may be a little less than the 1-D results due to the small area portion of the convex part in the x-cross section, but nevertheless, the agreement between 1-D and 2-D results in oxide kinetics is good enough. For the oxidation kinetics of the doped alloy, we may approximately consider the oxide to have a uniform thickness. The thickness of the oxide scale is reduced by an amount of about 40%.

According to experiments, binary alloys with yttrium dopants demonstrate not only smaller oxide scale thickness, but also better adherence with the alloy than do pure alloys. One of the mechanisms for this improvement is that dopants increase

the adhesion energy, which is beyond the scope of the current study. Another important mechanism is that any impurity addition changes the oxidation process in a way that reduces the oxide failure driven forces.

Figure 4.7 shows the distribution of stress components along x_1 (σ_{11}) after 250 hours of oxidation. For both cases, oxidation formation has induced GPa-level compressive stresses in the oxide grain boundaries, especially at the oxide-alloy interface (indicated by the white dashed line), and alloy depletion induced tensile stresses can be found around the oxide grain boundaries. As a consequence of the high level of compressive σ_{11}, a normal tensile stress σ_{22} of hundred MPa level presents on both sides of the high compressive area around the oxide/alloy interface (Figure 4.8). Except for the aforementioned observation in common, the stress level from the oxidation results of the doped alloy is remarkably lower than the stress level results obtained from the pure alloy. For example, the highest tensile stress σ_{22} obtained for pure alloy, as in Figure 4.8 (a), is 120 MPa. While for the doped alloy, this value is about 60 MPa. Since tensile σ_{22} is generally agreed to be the driven force of scale spallation, reduction of this normal tensile stress could effectively improve the protection of the oxide scale from failure. A more detailed tensile stress comparison along the interface in Figure 4.9 demonstrates that such improvement of protection is realized not only in reducing the level of the highest tensile stress, but in decreasing the area that high tensile stresses affect. This results is in certain level consistent with the mechanism proposed by Pieraggi and Rapp [120] that a fraction of the growth stress origin, misfit dislocation, has been pinned by the reactive element such that

both the level and the affected area of interfacial stresses decrease. According to [120], the misorientation dislocation climb parallel to the interface could be considered for the annihilation of vacancies upon cationic oxidation.

Grain refinement is another important phenomenon observed in oxidation of doped alloy. Grains that form the oxide scale of doped alloys are smaller and denser than those obtained in oxidation of pure alloys. A new simulation of oxidation of doped alloy with identical material properties but smaller oxide grain size was carried out. The comparison of the failure driven force σ_{22} generated after 250 hours of oxidation of a doped alloy with different grain sizes is given in Figure 4.10. The results show that the fine grain morphology further reduces the normal interfacial tensile stresses, which, in other words, could be reflected as the improvement of interfacial adherence; these results agree qualitatively with the experimental results.

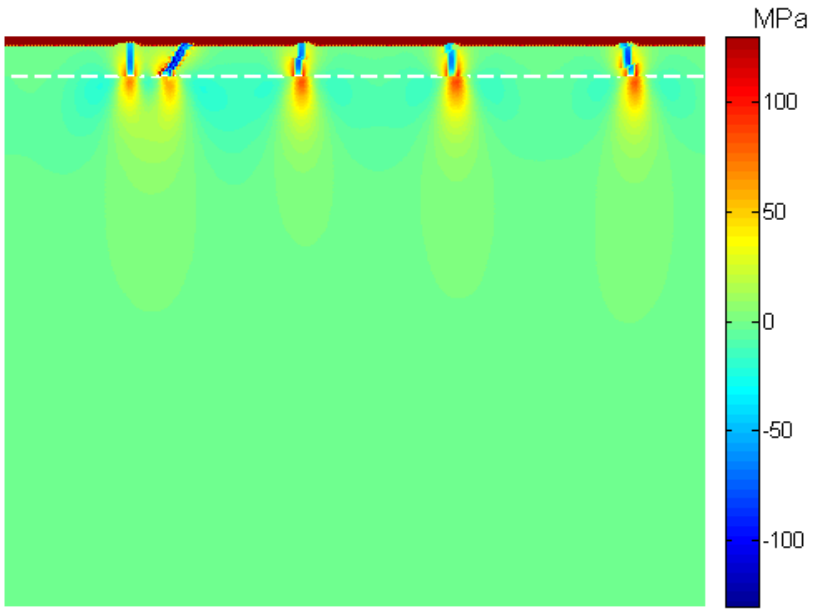

(a)

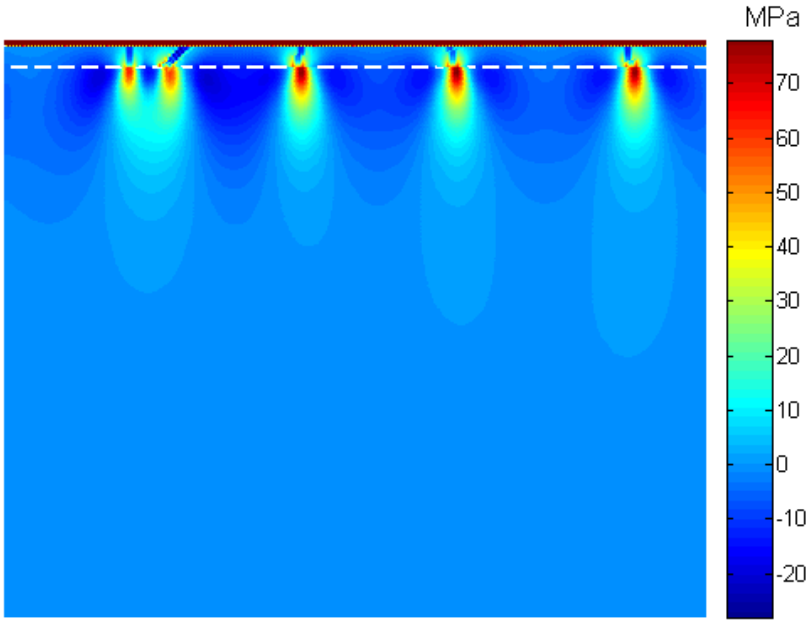

(b)

Figure 4.8 (a) Contour of normal stress σ_{22} in pure alloy and its oxide after 250 hours of oxidation. (b) Contour of normal stress σ_{22} in yttrium doped alloy and its oxide after 250 hours of oxidation.

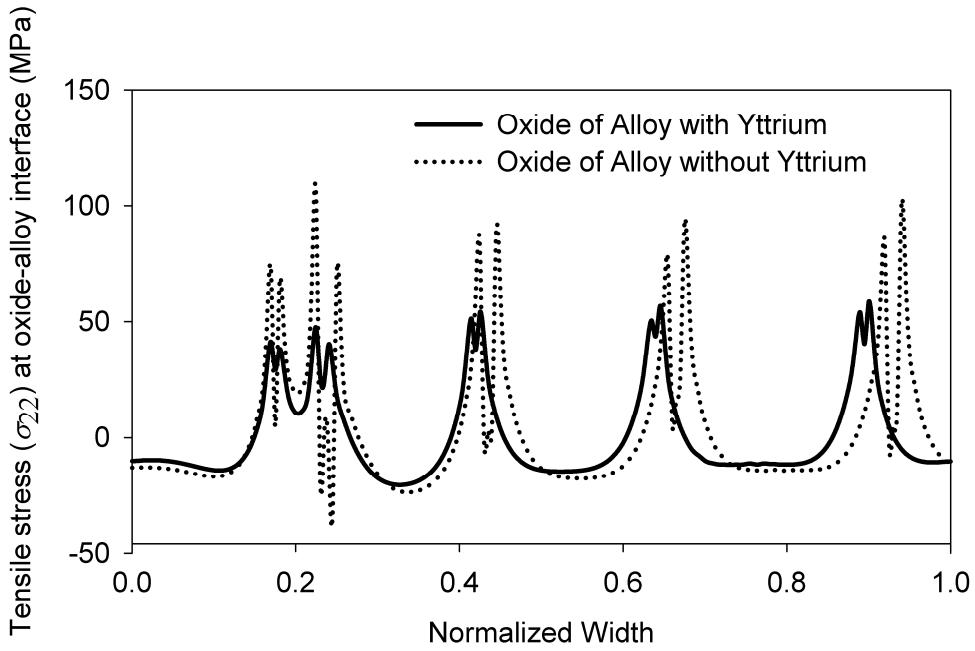

Figure 4.9 Normal Stresses σ_{22} at oxide-alloy interface after 250 hours of oxidation.

Last but not least, the effects of yttrium segregation are studied. During scale growth the distribution of the segregated reactive particles in the grain boundary areas could also affect the spallation driven forces even though the average of Yttria activities are the same. Figure 4.11 (a) plots the results obtained for interfacial σ_{22} with respect to different Δa but identical activation energy of Y_2O_3. A local plot in Figure 4.11 (b) shows more details of the change of σ_{22} around one grain boundary. The results show that both highest compressive and tensile normal stresses decrease with the increase of Δa in the grain boundary areas, which means biased distribution of reactive element could effectively reduce the ionic diffusion in the grain boundaries such that the oxide-alloy interfacial adhesion is improved.

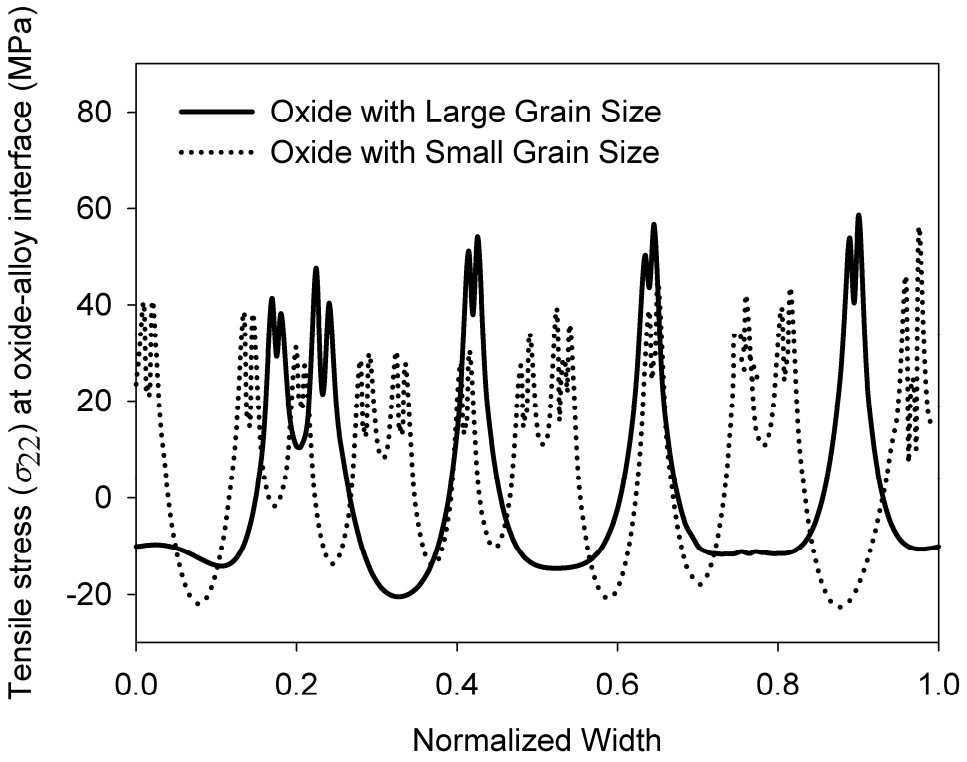

Figure 4.10 Grain size effect on normal stresses σ_{22} at oxide-alloy interface after 250 hours of oxidation.

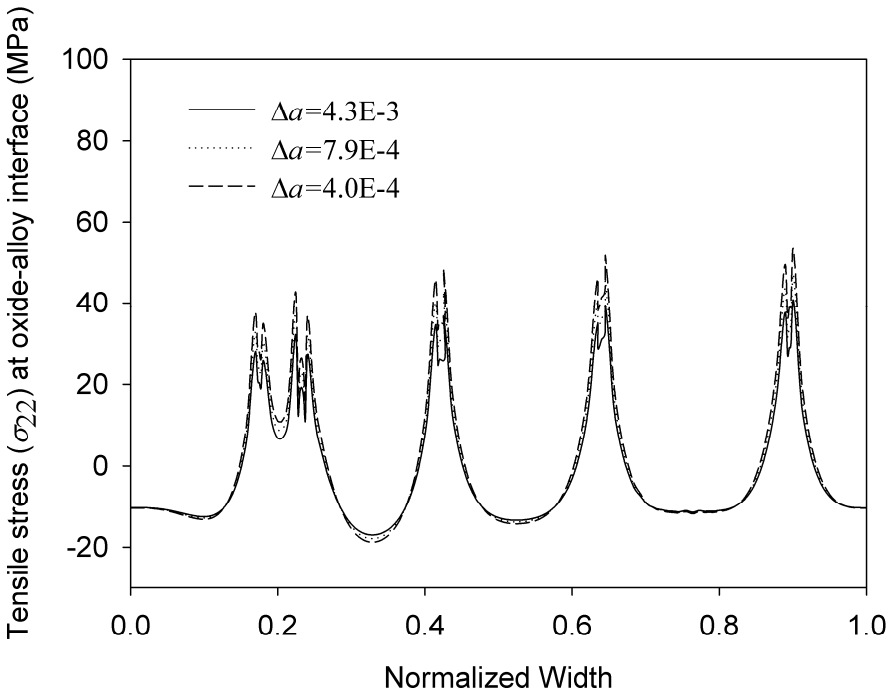

(a)

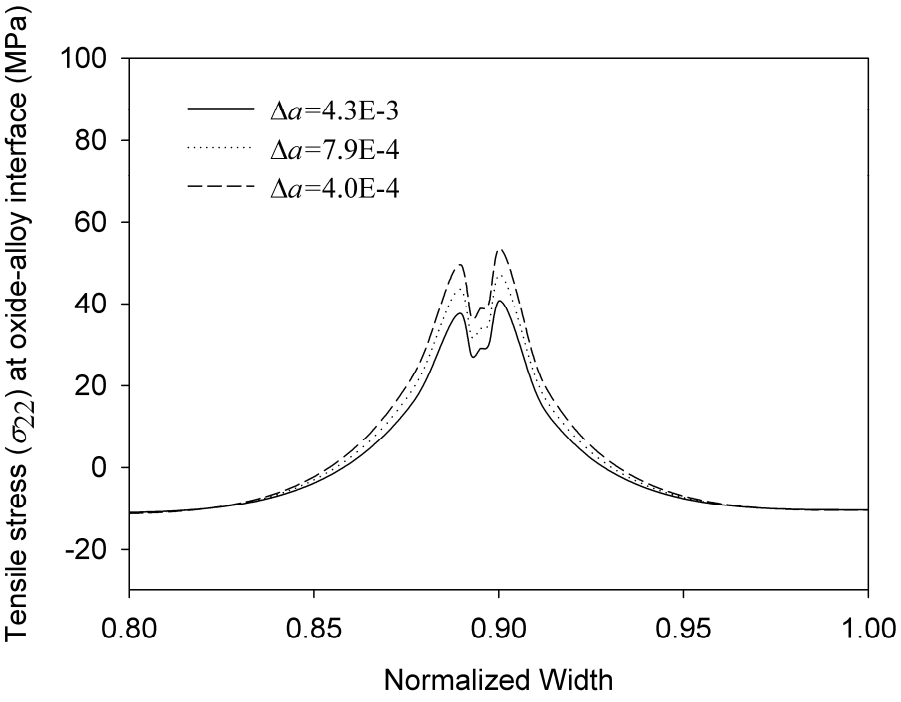

(b)

Figure 4.11 (a) The effect of Δa in grain boundary on normal stresses σ_{22} at oxide-alloy interface. (b) Enlargement of the part in (a) with x from 0.8 to 1.0

4.4. Conclusions

In this chapter, a 2D finite element model has been presented to analyze the effects of reactive elements on the oxidation of chromia scale forming binary alloys. The quantitative relation between the diffusivities of chromium ions and the activities of a reactive element (yttrium) has been derived for the first time and has been incorporated with a continuum thermodynamic model accounting for stress-diffusion interaction in the oxidation of Fe-Cr alloys. The model provides clear insight into the diffusion barrier mechanisms of reactive elements and into the effect of ionic diffusion on the stress distributions. The advantage of the stress-diffusion coupling model also show that the model provides a detailed distribution of stresses, as well as concentration distributions of all diffusing species in the system. The presented results confirm the experimental outcomes by predicting that the thickness of the oxide scale of Fe-Cr-Y is much less than that of Fe-Cr under identical oxidizing circumstances. It is also shown that normal tensile stresses with lower magnitude are generated at the oxide-alloy interface when the alloys are doped with reactive elements, which is believed to be among the important origins of reducing the driving force for oxide spallation. Hence the oxide-alloy interfacial adhesion is consequently improved. Finally, the model also predicts that a biased distribution of yttria activities in oxide grain boundaries would result in better spallation resistance.

CHAPTER 5 THE INELASTIC EXTENSION OF THE STRESS-OXIDATION INTERACTION MODEL

5.1. Introduction

Growth of oxide scale on metallic alloys may cause significant mechanical stress in the scale layer. In return, such stress may affect the oxidation kinetics and may also lead to scale spallation or detachment [8, 16, 124]. Mechanisms of stress generation in the scale may include heteroepitaxy [17], Pilling and Bedworth ratio (PBR) conversion from metal into scale [18-19], oxygen incorporation in substrate or reaction composition of oxygen and metal, nonstoichiometric vacancies concentration in the scale, etc. Among these, the PBR, i.e., the ratio of the oxide molar volume to that of the metal [18-19], is believe to be primarily responsible for the generation of stresses during selective oxidation [12], although oxygen incorporation in substrate or reaction composition of oxygen and metal may also introduces significant stresses in certain alloys.

Cationic diffusion is one sequential process of alloy oxidation. This metal atoms ionization and diffusion process eventually leads to injection of vacancies into the alloy substrate. However, it is observed that these vacancies are inconsistent with strong adherence at the alloy-oxide interface, in other words, the vacancies have to be annihilated by some intrinsic dislocation climb into the metal [17]. Interestingly, the dislocation has to return to the interface by a glide mechanism under the driving

foreces of strain energy minimization [29, 95]. This conforms to the plastic deformation mechanism of alloys at moderate to high temperature and hence provides local plastic strains.

Interfacial imperfections commonly exist between the oxide scales and the alloys during the oxidation process. The dissimilarity of material properties between alloys and oxides lead to complex interfacial fracture problems. To protect the oxide scale, it is pertinent to understand the mechanism of interfacial failure between such biomaterial interfaces. Unlike the crack propagation in homogenous media, the propagation of interfacial crack is in a mixed mode which is a combination of the commonly known failure modes type I and type II.

For a preexisting interfacial crack, an important issue is to determine its extending criteria. For elastic-plastic materials, those criteria are mostly based on change of energy. The energy release rate G [91], defined as the energy dissipation when a crack extends a unit area, is the criterion that is mostly used. For elastic-plastic materials, the energy release rate can be estimated by the J integral [92-93], or it can simply be calculated by its definition.

In this study, we extend our previous work by including inelastic deformation of the alloy. Details of these differences and their consequences will be explained later in this chapter. To demonstrate our model, a binary alloy (16% wt Fe-Cr) is used in this chapter as a model material. This model is implemented first in two-dimension using finite element method to study the propagation driving force of an interfacial crack along the oxide-alloy interface after steady state has been reached with the alloy

experiencing deformation plasticity. The model is then used in another two-dimensional study of the creep effect on the overall mechanical performance of the material during oxidation process. In both of these two studies, the reactive element effects are intensively studied. Finally, it will be seen from the derivation that the general approach presented here is applicable to a wide range of alloys.

5.2. Model Description for Inelastic Extension

When writing the field quantities related to deformation such as strain and stress, it is often convenient to introduce the Lagrangian reference frame X_i (i = 1, 2, 3). We assume in this chapter that X_i coincide with x_i initially at t = 0. The two coordinates are related by

$$\mathbf{x} = \mathbf{X} + \mathbf{U}(\mathbf{X}, t) \quad \text{or} \quad \mathbf{X} = \mathbf{x} - \mathbf{U}(\mathbf{X}(\mathbf{x}), t) = \mathbf{x} - u(\mathbf{x}, t), \tag{5.1}$$

where $\mathbf{U}(\mathbf{X}, t)$ is the particle displacement of the particle **X**, while $u(\mathbf{x}, t)$ can be interpreted as the displacement of the particle instantaneously located at **x**.

5.2.1 Kinematic Equations

The total deformation gradient tensor **F** is related to the displacement vector $\mathbf{U}(\mathbf{X}, t)$ through

$$\mathbf{F} = \mathbf{F}^e\mathbf{F}^p\mathbf{F}^c = \mathbf{I} + \nabla_X \mathbf{U} \quad , \quad \text{or} \quad \mathbf{F}^{-1} = \left(\mathbf{F}^e\mathbf{F}^p\mathbf{F}^c\right)^{-1} = \mathbf{I} - \nabla\mathbf{u} \quad . \tag{5.2}$$

The eigentransformation due to compositional change is given by

$$\mathbf{F}^c = \left(J^c\right)^{1/3}\mathbf{I} = \sqrt{1 + 2\sum_s \eta_s \Delta c_s}\,\mathbf{I} \quad . \tag{5.3}$$

where η_s is the coefficients of compositional expansion (CCE) and Δc_s is the

deviation of molar fraction of c_s from its stoichiometric composition [36].

It then follows from the second of (5.2) that

$$\mathbf{F}^{pe} = \mathbf{F}^{p}\mathbf{F}^{e} = (\mathbf{I} - \nabla\mathbf{u})^{-1} \cdot \left(\mathbf{F}^{c}\right)^{-1} = \frac{(\mathbf{I} - \nabla\mathbf{u})^{-1}}{\sqrt{1 + 2\sum_{s} \eta_s \Delta c_s}} \quad , \tag{5.4}$$

Or it may be given in another form

$$\mathbf{F}^{e} = \mathbf{F}^{p-1} \cdot \frac{(\mathbf{I} - \nabla\mathbf{u})^{-1}}{\sqrt{1 + 2\sum_{s} \eta_s \Delta c_s}} \tag{5.5}$$

The green deformation tensors are then obtained as

$$\begin{aligned} \mathbf{C}^{\mathbf{F}} &= \left(\mathbf{F}\right)^{T} \mathbf{F} = \left[(\mathbf{I} - \nabla\mathbf{u})^{-1}\right]^{T} (\mathbf{I} - \nabla\mathbf{u})^{-1} \\ \mathbf{C}^{pe} &= \left(\mathbf{F}^{pe}\right)^{T} \mathbf{F}^{pe} = \frac{1}{1 + 2\sum_{s} \eta_s \Delta c_s} \left[(\mathbf{I} - \nabla\mathbf{u})^{-1}\right]^{T} (\mathbf{I} - \nabla\mathbf{u})^{-1} \cdot \quad . \end{aligned} \tag{5.6}$$

In the metal ($x_3 < 0$), the chromium atom (s = Cr(a)) is the only independent diffusible species. $\eta_{\mathrm{Cr}(a)}$ can be measured experimentally or computed using molecular dynamic simulations [104]

5.2.2 Kinetic Equations

The mechanical stresses in both the oxide scale and the metal substrate must satisfy the equilibrium equations. In terms of the first Piola-Kirchhoff stress tensor, the equilibrium equations can be written as

$$\nabla_X \cdot \boldsymbol{\sigma}^{0} = \left(\nabla_x \cdot \boldsymbol{\sigma}^{0}\right) : \mathbf{F} = 0 \quad , \tag{5.7}$$

where the first gradient operator is with respect to the Lagrangian coordinates **X** and the second one is with respect to the spatial coordinates **x** as indicated by the subscript.

Making use of the Hooke's law, one can express the first Piola-Kirchhoff stress tensor in term of the deformation gradients,

$$\boldsymbol{\sigma}^0 = \left(\mathbf{C} : \mathbf{E}^e\right) \cdot \mathbf{F}^T, \tag{5.8}$$

where **C** is the elastic stiffness tensor. Similar to chapter 3, it is also assumed that **C** is independent of Δc_s.

In the alloy part, when plastic deformation occurs, the rate of deformation can be given by the flow rule, i.e.

$$\mathbf{D}^p = \dot{\lambda}\mathbf{S} \tag{5.9}$$

or in the form of the deformation gradient

$$\frac{1}{2}\left(\dot{\mathbf{F}}^p \cdot \mathbf{F}^{p-1} + \mathbf{F}^{p-\mathbf{T}} \cdot \dot{\mathbf{F}}^{p\mathbf{T}}\right) = \dot{\lambda}\mathbf{S}. \tag{5.10}$$

where $\dot{\lambda}$ is a scalar multiplier, and $\mathbf{S}$ is the deviatoric stress tensor.

5.2.3 Stress-Dependent Chemical Potential

Strictly speaking, electrochemical potentials should be used for the oxidation process. However, if local electroneutrality is assumed (as done here), the diffusion process can be described using the chemical potential alone [36]. For most insulating and semi-conducting ceramics, local electroneutrality is an excellent assumption throughout the film, except for the thin surface layers of a few nanometers [1, 105]. The stress-dependent chemical potential for a species *s* in ionic solids has been derived in [36],

$$\mu_s = \mu_s^0 + RT \ln c_s + V_s^m \tau_s \quad , \tag{5.11}$$

where μ_s^0 is the chemical potential of species *s* at some reference state, R and T

are the universal gas constant and temperature, respectively, V_s^m is the molar volume of species *s* in its nature (stress-free stoichiometric state). The last term in (3.8) is the stress-dependent part of the chemical potential derived in [36, 95]. If one assumes that the elastic stiffness tensor is independent of concentration, then τ_s reduces to

$$\tau_s = w_s\left(\mathbf{C}^{pe}\right) + \frac{\mathrm{tr}\left[\boldsymbol{\Sigma}\right]}{3J^c}\frac{\partial J^c}{\partial c_s}, \tag{5.12}$$

where $J^c = \left\|\mathbf{F}^c\right\|$ is the Jacobian of the deformation gradient tensor, and $w_s\left(\mathbf{C}^{pe}\right)$ is partial derivative strain energy density with respect to the species concentration, i.e.

$$w_s\left(\mathbf{C}^{pe}\right) = \frac{\partial w\left(\mathbf{C}^{pe}\right)}{V_m \partial \rho_s} \tag{5.13}$$

and the Eshelby stress tensor is in the form of [95]

$$\boldsymbol{\Sigma} = J^c w_0\left(\mathbf{C}^{pe}\right)\mathbf{I} - \tilde{\boldsymbol{\sigma}}\mathbf{C}^{\mathbf{F}}. \tag{5.14}$$

where $w_0\left(\mathbf{C}^{pe}\right)$ is the strain energy density per unit stress-free state volume, $\tilde{\boldsymbol{\sigma}}$ is the second Piola-Kirchhoff stress tensor.

5.2.4 Governing Equation and Boundary Conditions

In addition to the stress equilibrium equation (5.7), the continuity equation (3.17)-(3.19) are used in the oxide scale to govern the ionic diffusion. Similarly, we also need (3.20) in the alloy to describe the Cr atom diffusion.

In both oxide scale and alloy, the unknowns are still $\mathbf{u}(\mathbf{x},t)$ in all fields, $c_{Cr}(\mathbf{x},t)$ and $c_O(\mathbf{x},t)$ in the oxide scale, as well as $c_{\mathrm{Cr}(a)}(\mathbf{x},t)$ in the alloy. With

proper continuity conditions at the scale-air and metal-scale interfaces, and proper boundary conditions on the sides of the structure depicted in Figure 3.1, these partial differential equations formulate a boundary value problem that can be solved to obtain the deformation, stresses and the defect concentration throughout the scale layer and the metal substrate, as well as the oxidation kinetics.

5.3. Two-dimensional implementation on small scale yielding example

To illustrate the utility of the model formulated above and to reveal certain fundamental features of the model predictions, we present a two-dimensional numerical example in this section. The inelasticity of the substrate alloy is assumed to be deformation plasticity. Furthermore, since the inelastic behaviors accommodate the deformation due to nonstoichiometry and materials are confined in fixed areas, the plastic deformations are assumed to be small scale yielding.

5.3.1 Alloy-oxide Model with isotropic deformation plasticity in alloy

Figure 5.1 illustrates the geometry of a 2-D model of an alloy carrying a Cr_2O_3 layer at its top surface. A pre-existing crack lies along the oxide-alloy interface. The 2-D model has an x_3 thickness that is very large in comparison with the dimensions in the other two directions. This figure is for illustration purpose only and is not to scale. In this case study, we assume that all the material properties are independent of the ion concentration. Also, the scale layer is assumed to be a linear elastic and isotropic solids with E_1 and ν_1 being the elastic constants, and the metal

substrate is assumed to be an elastic-plastic and isotropic solids with E_2 and ν_2 being the elastic constants. The plastic constants will be given in a later derivation. All the elastic and plastic constants are assumed to be independent of the defect concentration for the case of the dilute concentration.

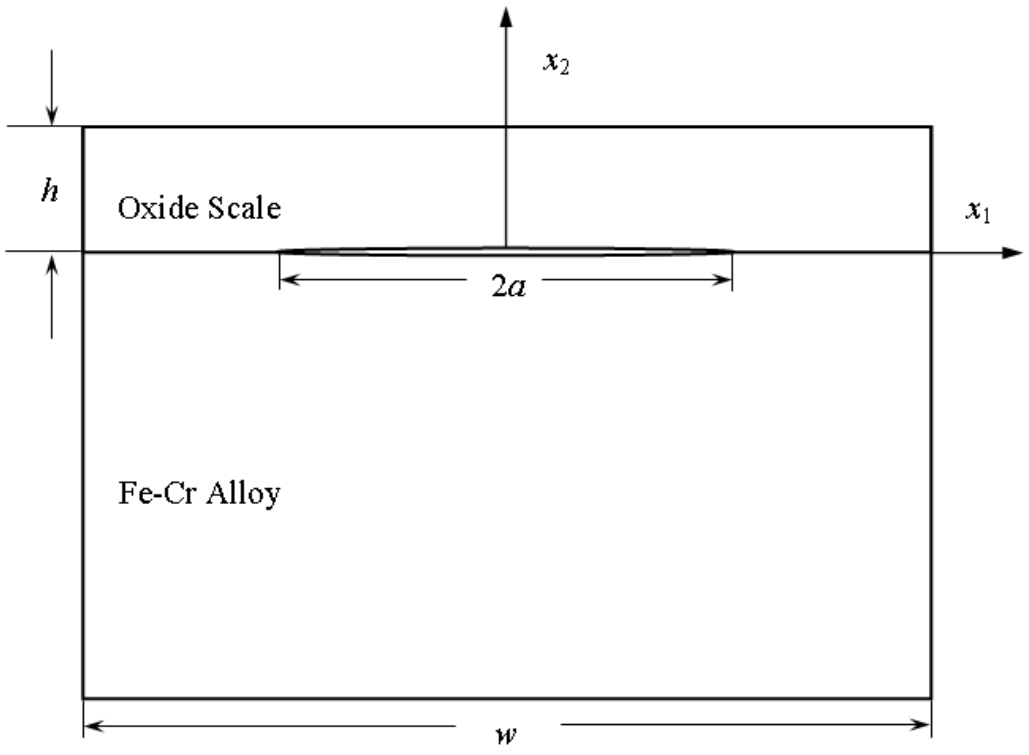

Figure 5.1 Schematic of the alloy-oxide structure with a interfacial crack (not to scale).

Since failure-inducing defects such as voiding and spallation usually take place after a relatively long period of oxidation, we assume that a steady state of

oxidation has been reached. So we only focus on steady state oxidation in this study. In this case, the interfacial failure is the primary interest rather than the oxide kinetics. Since the surface growth of the oxide has few effects on the interfacial crack growth driving force, we then assume a relatively thick scale and ignore the scale growth afterward. Based on this assumption, it is different from previous studies that the steady state in this case is time independent.

5.3.2 Stress-Dependent Chemical Potential

In the two-dimensional case, the chemical potential that governs the ionic diffusion is the same as equation (3.8). Here we focus on the description of the chemical potential governing the chromium atom, i.e.

$$\mu_{Cr(a)} = \mu^0_{Cr(a)} + RT \ln c_{Cr(a)} + V^m_{Cr(a)} \tau_{Cr(a)} \tag{5.15}$$

where $\mu^0_{Cr(a)}$ is the chemical potential of the chromium atom at a reference state, $V^m_{Cr(a)}$ is the molar volume of the substrate alloy in its natural (stress-free stoichiometric) state. The stress-dependent part of the chemical potential in equation (5.15) for small strain plastic deformation is in the form of

$$\begin{aligned} \tau_{Cr(a)} = \eta_{Cr(a)} \Bigg[& \frac{3}{2} \left[\boldsymbol{\varepsilon}^E \right]^T \left[\mathbf{C}_2 \right] \left[\boldsymbol{\varepsilon}^E \right] \\ & + 3 \left(\int \sigma_{kk} d\varepsilon^p_{kk} + \int \sigma_{23} d\varepsilon^p_{23} + \int \sigma_{13} d\varepsilon^p_{13} + \int \sigma_{12} d\varepsilon^p_{12} \right) - \sigma_{kk} \Bigg] \end{aligned} \tag{5.16}$$

where ε^p_{ij} is the plastic strain, the elastic strain tensor $\left[\boldsymbol{\varepsilon}^E \right]$ and elastic constant tensor will be given in the following section.

For the elastic deformation in the oxide scale, the stress-dependent part of the chemical potentials of the chromium ion and oxygen ion can still be described as

$$\tau_s = \eta_S \left[\frac{3}{2} \left[\boldsymbol{\varepsilon}^E \right]^T \left[\mathbf{C}_2 \right] \left[\boldsymbol{\varepsilon}^E \right] - \sigma_{kk} \right]. \tag{5.17}$$

with *s* representing Cr or O

5.3.3 Governing equations in 2-D

From chapter 3, deformation and defect concentration throughout the oxide scale layer and alloy substrate can be solved from the corresponding governing partial differential equations with proper continuity conditions. For the two dimensional model in the current study, the equilibrium equations

$$\begin{aligned} \frac{\partial \sigma_{11}}{\partial x_1} + \frac{\partial \sigma_{12}}{\partial x_2} &= 0 \\ \frac{\partial \sigma_{21}}{\partial x_2} + \frac{\partial \sigma_{22}}{\partial x_1} &= 0 \end{aligned} \tag{5.18}$$

have to be satisfied both in the oxide and in the alloy substrate.

The non-zero elastic strain components in the oxide scale are given as

$$\begin{aligned} \varepsilon_{11}^E &= \frac{\partial u_1}{\partial x_1} - \sum_s \eta_s \Delta c_s, \\ \varepsilon_{22}^E &= \frac{\partial u_2}{\partial x_2} - \sum_s \eta_s \Delta c_s, \\ \varepsilon_{33}^E &= -\sum_s \eta_s \Delta c_s, \\ \varepsilon_{12}^E &= \frac{1}{2} \left(\frac{\partial u_1}{\partial x_2} + \frac{\partial u_2}{\partial x_1} \right) \end{aligned} \tag{5.19}$$

The corresponding constitutive relations in the scale are given as

$$\sigma_{11}=\frac{E}{(1+\nu)(1-2\nu)}\left[(1-\nu)\left(\frac{\partial u_1}{\partial x_1}-\sum_s \eta_s \Delta c_s\right)+\nu\left(\frac{\partial u_2}{\partial x_2}-2\sum_s \eta_s \Delta c_s\right)\right]$$

$$\sigma_{22}=\frac{E}{(1+\nu)(1-2\nu)}\left[(1-\nu)\left(\frac{\partial u_2}{\partial x_2}-\sum_s \eta_s \Delta c_s\right)+\nu\left(\frac{\partial u_1}{\partial x_1}-2\sum_s \eta_s \Delta c_s\right)\right]$$

$$\sigma_{33}=\frac{E}{(1+\nu)(1-2\nu)}\left[(1-\nu)\left(-\sum_s \eta_s \Delta c_s\right)+\nu\left(\frac{\partial u_2}{\partial x_2}-\sum_s \eta_s \Delta c_s\right)+\nu\left(\frac{\partial u_1}{\partial x_1}-\sum_s \eta_s \Delta c_s\right)\right] \quad (5.20)$$

$$\sigma_{12}=\frac{E}{2(1+\nu)}\left(\frac{\partial u_1}{\partial x_2}+\frac{\partial u_2}{\partial x_1}\right)$$

In the substrate alloy, the elastic strains are given as

$$\begin{aligned}
\varepsilon_{11}^E &= \frac{\partial u_1}{\partial x_1}-\frac{3}{2}\alpha\left(\frac{q}{\sigma^0}\right)^{n-1}\frac{S_{11}}{E}-\eta_{Cr(a)}\Delta c_{Cr(a)},\\
\varepsilon_{22}^E &= \frac{\partial u_1}{\partial x_2}-\frac{3}{2}\alpha\left(\frac{q}{\sigma^0}\right)^{n-1}\frac{S_{22}}{E}-\eta_{Cr(a)}\Delta c_{Cr(a)},\\
\varepsilon_{33}^E &= -\frac{3}{2}\alpha\left(\frac{q}{\sigma^0}\right)^{n-1}\frac{S_{33}}{E}-\eta_{Cr(a)}\Delta c_{Cr(a)},\\
\varepsilon_{12}^E &= \frac{1}{2}\left(\frac{\partial u_1}{\partial x_2}+\frac{\partial u_2}{\partial x_1}\right)-\frac{3}{2}\alpha\left(\frac{q}{\sigma^0}\right)^{n-1}\frac{S_{12}}{E},
\end{aligned} \quad (5.21)$$

and the corresponding stress in the substrate alloy are obtained as

$$\begin{aligned}
\sigma_{11} &= \frac{E}{(1+\nu)(1-2\nu)}\left[(1-\nu)\varepsilon_{11}^E+\nu\left(\varepsilon_{22}^E+\varepsilon_{33}^E\right)\right]\\
\sigma_{22} &= \frac{E}{(1+\nu)(1-2\nu)}\left[(1-\nu)\varepsilon_{22}^E+\nu\left(\varepsilon_{11}^E+\varepsilon_{33}^E\right)\right]\\
\sigma_{33} &= \frac{E}{(1+\nu)(1-2\nu)}\left[(1-\nu)\varepsilon_{33}^E+\nu\left(\varepsilon_{11}^E+\nu\varepsilon_{22}^E\right)\right]\\
\sigma_{12} &= \frac{E}{(1+\nu)}\varepsilon_{12}^E
\end{aligned} \quad (5.22)$$

where the deviatoric stresses

$$S_{11}=\sigma_{11}-\frac{\sigma_{kk}}{3}, S_{22}=\sigma_{22}-\frac{\sigma_{kk}}{3}, S_{33}=\sigma_{33}-\frac{\sigma_{kk}}{3}, S_{12}=\sigma_{12} \quad (5.23)$$

α is the yield offset, σ^0 is the yield stress in one direction tensile load, n is the

plastic hardening exponent, q is the effective stress with the form of

$$q = \sqrt{3\left[\left(\sigma_{11} - \sigma_{22}\right)^2 / 4 + \sigma_{12}^2\right]}. \qquad (5.24)$$

The mass continuity equations for Cr and O ions in the oxide scale are given as

$$\begin{aligned} 0 &= D_{Cr}\left[\frac{\partial}{\partial x_1}\left(\frac{\partial c_{Cr}}{\partial x_1} + c_{Cr}\frac{V_{Cr}^m}{RT}\frac{\partial \tau_{Cr}}{\partial x_1}\right) + \frac{\partial}{\partial x_2}\left(\frac{\partial c_{Cr}}{\partial x_2} + c_{Cr}\frac{V_{Cr}^m}{RT}\frac{\partial \tau_{Cr}}{\partial x_2}\right)\right], \\ 0 &= D_{O}\left[\frac{\partial}{\partial x_1}\left(\frac{\partial c_{O}}{\partial x_1} + c_{O}\frac{V_{O}^m}{RT}\frac{\partial \tau_{O}}{\partial x_1}\right) + \frac{\partial}{\partial x_2}\left(\frac{\partial c_{O}}{\partial x_2} + c_{O}\frac{V_{O}^m}{RT}\frac{\partial \tau_{O}}{\partial x_2}\right)\right], \end{aligned} \qquad (5.25)$$

and for Cr atoms in the alloy substrate

$$\begin{aligned} 0 = D_{Cr(a)}\Bigg[&\frac{\partial}{\partial x_1}\left(\frac{\partial c_{Cr(a)}}{\partial x_1} + c_{Cr(a)}\frac{V_{Cr(a)}^m}{RT}\frac{\partial \tau_{Cr(a)}}{\partial x_1}\right) \\ &+ \frac{\partial}{\partial x_2}\left(\frac{\partial c_{Cr(a)}}{\partial x_2} + c_{Cr(a)}\frac{V_{Cr(a)}^m}{RT}\frac{\partial \tau_{Cr(a)}}{\partial x_2}\right)\Bigg] \end{aligned} \qquad (5.26)$$

where $D_{Cr(a)}$ is the diffusivity of chromium atom in Fe-Cr alloy.

With the chemical reaction equilibrium assumption holding in the oxide, we have

$$d\mu_p - 2d\mu_{\mathrm{Cr}} - 3d\mu_{\mathrm{O}} = 0 \qquad (5.27)$$

in the oxide scale, where the stress dependent parts of the chemical potentials in (5.25) and (5.26) are given by (5.17), i.e.,

$$\begin{aligned} \tau_{Cr} &= \eta_{Cr}\left(\frac{3}{2}\left[\boldsymbol{\varepsilon}^E\right]^T\left[\mathbf{C}_1\right]\left[\boldsymbol{\varepsilon}^E\right] - \sigma_{11} - \sigma_{22} - \sigma_{33}\right) \\ \tau_{O} &= \eta_{O}\left(\frac{3}{2}\left[\boldsymbol{\varepsilon}^E\right]^T\left[\mathbf{C}_1\right]\left[\boldsymbol{\varepsilon}^E\right] - \sigma_{11} - \sigma_{22} - \sigma_{33}\right) \end{aligned} \qquad (5.28)$$

and elastic constants

$$\left[\mathbf{C}_i\right]=\frac{E_i}{\left(1+\nu_i\right)\left(1-2\nu_i\right)}\begin{bmatrix}1-\nu_i & \nu_i & \nu_i & 0 & 0 & 0\\ \nu_i & 1-\nu_i & \nu_i & 0 & 0 & 0\\ \nu_i & \nu_i & 1-\nu_i & 0 & 0 & 0\\ 0 & 0 & 0 & 1-2\nu_i & 0 & 0\\ 0 & 0 & 0 & 0 & 1-2\nu_i & 0\\ 0 & 0 & 0 & 0 & 0 & 1-2\nu_i\end{bmatrix} \tag{5.29}$$

with *i* represents alloy or oxide.

In addition to the governing equations above, the interface conditions need to be specified. In the structure shown in Figure 5.1, there are two interfaces, the metal-scale interface and the scale-air interface. At these interfaces, the following conditions must be satisfied: (a) mass flux continuity of each species, (b) continuity of chemical potential of each species for adsorption and ionization reaction, respectively, (c) continuity of displacement and (e) continuity of traction. These conditions are described below.

Metal-Scale Interface ($x_2=0$)

The metal-scale interface is divided into two portions, the perfect portion and the crack portion. For the former interface, the ionization of Cr atoms is assumed to be an equilibrium process. Thus, the continuity of chemical potentials must hold between Cr ions and Cr atoms, i.e.

$$\frac{\mu^0_{\mathrm{Cr}(a)}-\mu^0_{\mathrm{Cr}}}{RT}+\ln\frac{c_{\mathrm{Cr}(a)}}{c_{\mathrm{Cr}}}=\frac{V^m_{Cr}\tau_{Cr}-V^m_{Cr(a)}\tau_{Cr(a)}}{RT} \quad . \tag{5.30}$$

Conservation of mass for Cr across the interface leads to

$$\frac{\partial c_{\mathrm{Cr}(a)}}{\partial x_2}+\frac{V^m_{Cr(a)}c_{\mathrm{Cr}(a)}}{RT}\frac{\partial\tau_{Cr(a)}}{\partial x_2}=\frac{D_{\mathrm{Cr}}}{D_{\mathrm{Cr}(a)}}\left[\frac{\partial c_{\mathrm{Cr}}}{\partial x_2}+\frac{V^m_{Cr}c_{\mathrm{Cr}}}{RT}\frac{\partial\tau_{Cr}}{\partial x_2}\right] \quad . \tag{5.31}$$

Furthermore, traction continuity is automatically satisfied by the choice of

stress components, and the continuity of displacement leads to

$$u_1\big|_{x_2=0^+} = u_1\big|_{x_2=0^-}, u_2\big|_{x_2=0^+} = u_2\big|_{x_2=0^-} . \tag{5.32}$$

For the crack portion, the corresponding continuity of Cr chemical potentials leads to:

alloy side

$$\mu^0_{Cr(a)} + RT\ln c_{Cr(a)} + V^m_{Cr(a)}\tau_{Cr(a)} = 0 \tag{5.33}$$

oxide side

$$\mu^0_{Cr} + RT\ln c_{Cr} + V^m_{Cr}\tau_{Cr} = 0 \tag{5.34}$$

and conservation of mass for Cr is

alloy side

$$D_{\mathrm{Cr}(a)}\frac{\partial c_{\mathrm{Cr}(a)}}{\partial x_2} + \frac{D_{\mathrm{Cr}(a)}c_{\mathrm{Cr}(a)}}{RT}V^m_{\mathrm{Cr}(a)}\frac{\partial \tau_{\mathrm{Cr}(a)}}{\partial x_2} = 0 \tag{5.35}$$

oxide side

$$D_{\mathrm{Cr}}\frac{\partial c_{\mathrm{Cr}}}{\partial x_2} + \frac{D_{\mathrm{Cr}}c_{\mathrm{Cr}}}{RT}V^m_{\mathrm{Cr}}\frac{\partial \tau_{\mathrm{Cr}}}{\partial x_2} = 0 \tag{5.36}$$

At both surfaces of the crack, the traction free condition is automatically satisfied by the choice of stress components

Finally, per the assumption that no O can cross the interface for both portions, i.e.,

$$\frac{\partial c_{\mathrm{O}}}{\partial x_2} + \hat{\eta}_{\mathrm{O}}\left[c_{\mathrm{O}}\sum_s \eta_s \frac{\partial c_s}{\partial x_2}\right] = 0 \quad . \tag{5.37}$$

At the Scale-Air Interface ($x_2 = h$)

At the scale-air interface, an equilibrium condition is assumed for the ionization of oxygen (in the air), i.e.,

$$\frac{\mu_{\mathrm{O}_2}^0}{2RT} + \ln P_{\mathrm{O}_2}^{1/2} = \frac{\mu_{\mathrm{O}}^0}{RT} + \ln c_{\mathrm{O}} + V_O^m \tau_O . \tag{5.38}$$

Note that unlike the previous study, *h* is known a priori in this case. In addition, a fixed value boundary condition is applied on Cr ions at the surface, i.e.,

$$c_{\mathrm{Cr}}\big|_{x_2=h} = 0 . \tag{5.39}$$

Furthermore, it is assumed that, in comparison with the stresses in the scale layer, the atmospheric pressure is negligible in typical applications. Thus, the scale-air interface can be viewed as a traction free surface which is satisfied by the choice of the stress components.

Inside the alloy far from the interface, $c_{Cr(a)} = C$ as $x_2 \to -\infty$. Additionally, periodic boundaries are applied at the left ($x_1 = -\frac{w}{2}$) and right ($x_1 = \frac{w}{2}$) hand side of the 2D model, i.e.,

$$\begin{aligned} &u_1\big|_{x_1=-\frac{w}{2}} = u_1\big|_{x_1=\frac{w}{2}}, u_2\big|_{x_1=-\frac{w}{2}} = u_2\big|_{x_1=\frac{w}{2}} \\ &c_{Cr}\big|_{x_1=-\frac{w}{2}} = c_{Cr}\big|_{x_1=\frac{w}{2}}, c_O\big|_{x_1=-\frac{w}{2}} = c_O\big|_{x_1=\frac{w}{2}}, c_{Cr(a)}\big|_{x_1=-\frac{w}{2}} = c_{Cr(a)}\big|_{x_1=\frac{w}{2}} \end{aligned} \tag{5.40}$$

5.4. Finite Element Implementation

5.4.1 Implementation description

The two dimensional diffusion-stress coupling model for steady state oxidation of a binary alloy was implemented by the finite element method in the

commercial software ABAQUS with a user defined element subroutine. Emphasis was put on the crack extension driving forces and on failure. As shown in Figure 5.1, a binary alloy carrying a layer of oxide on it top with a crack laying along the scale-alloying interface is considered in this implementation. Continuity equations (5.25), (5.26) and equilibrium equations (5.18). together with corresponding boundaries are solved simultaneously to obtained u_1, u_2, c_{Cr}, c_O and $c_{Cr(a)}$. The oxygen partial pressure is set to be 0.3 atm at the air-oxide interface. Finally, in this simulation, all the materials (alloy, oxide) are assumed to be homogeneous and isotropic. In this study, the yield offset $\alpha = 2.3$, yield stress $\sigma^0 = 30\text{MPa}$, and the plastic hardening exponent n=6.44. All other material properties used in this finite element implementation are listed in Table 3.1 and Table 4.1. The half crack length a is 20 μm.

5.4.2 Results and discussions

The simulation is first carried out on the oxide scale bucking instability for validation. Under certain equi-biaxial compressive in-plane stress $\sigma_{11} = \sigma_{33} = -\sigma_c$, the oxide scale above the interfacial scale will bulk up. The analytical solution for this bucking instability has been obtained by Hutchinson and Suo [131]. The classical bucking stress of a clamped-clamped wide plate is solved as the critical bucking stress, which is in the form of

$$\sigma_c = \frac{\pi^2 B}{12} \frac{E_1}{\left(1-\nu_1^2\right)} \left(\frac{h}{a}\right)^2 \qquad (5.41)$$

where a is the half crack length, the bending stiffness

$$B = \frac{E_1 h^3}{12\left(1-\nu_1^2\right)}. \tag{5.42}$$

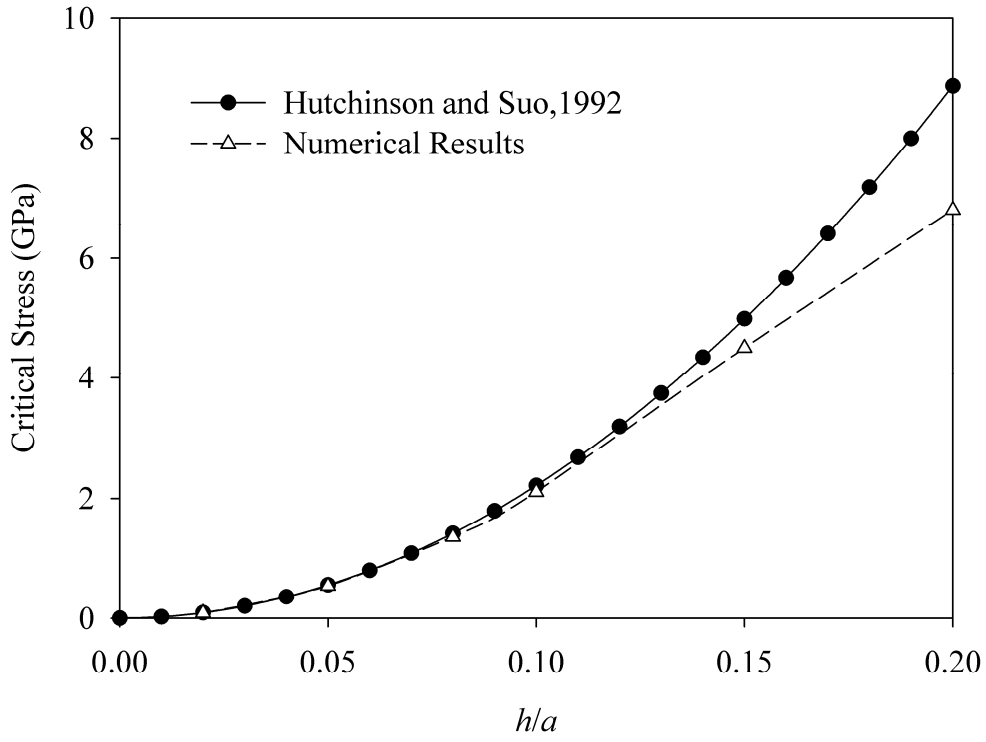

Figure 5.2 oxide scale bucking instability.

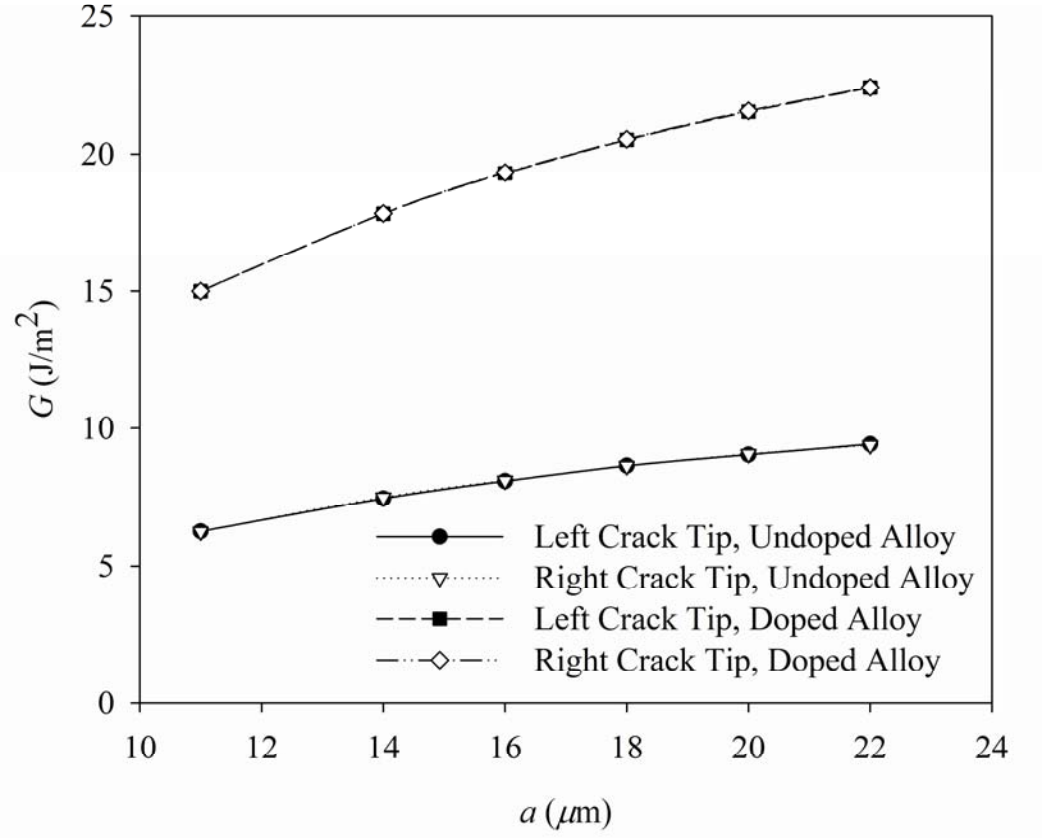

Figure 5.3 Energy release rate change with half crack length at the same oxide scale thickness.

To compromise with the analytical solution, the finite element analysis is applied to a bimaterial interfacial crack problem while ignoring plastic deformation in the alloy. The relation between σ_c and h/a from the finite element solution is plotted in Figure 5.2 along with the analytical relation (5.41). The solutions have fairly good agreement with each other, especially at the period that $h/a \le 0.1$. In this study, the half crack length a used in this simulation is 20 μm. Therefore, as long as

the scale is not much thicker than 2 μm, which is the typical steady-state scale thickness, the finite element solution is valid. For $h/a < 0.1$, the small h/a assumption of the analytical solution is violated, hence solution (5.41) may not be appropriate.

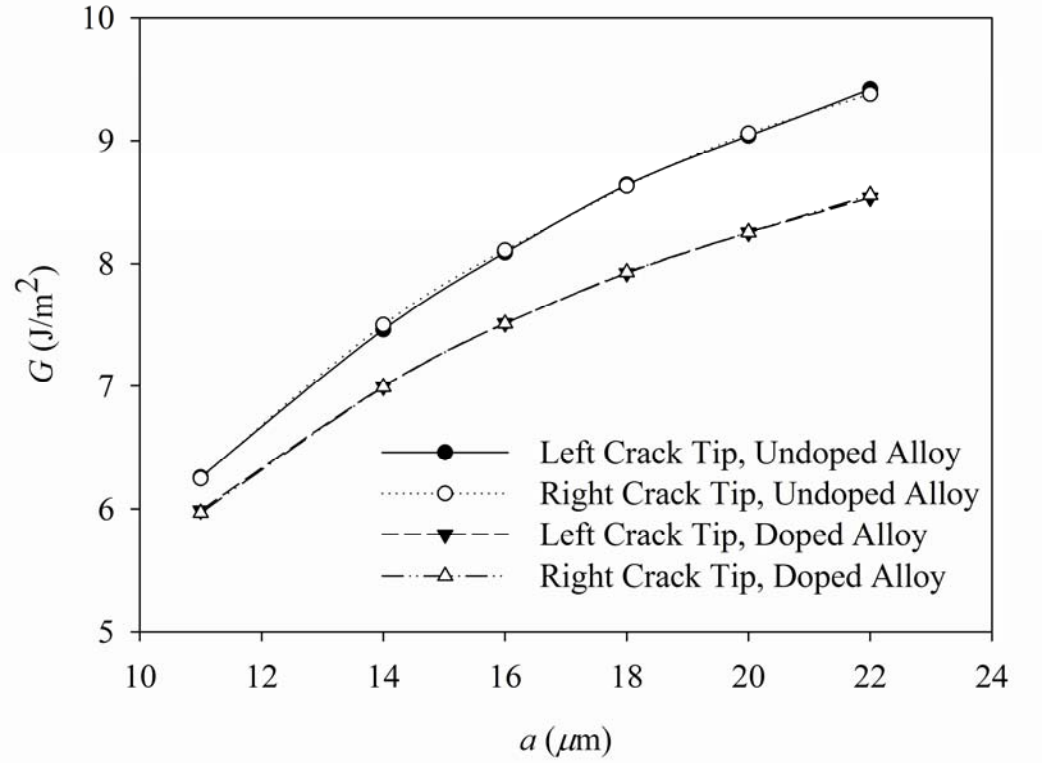

Figure 5.4 Energy release rate change with half crack length at the same oxidation time.

In previous works (chapter 3), we have analyzed the stress distribution in oxide scale and alloy, which gives us a general view of possible failure mechanism as

well as critical locations. A high level of normal tensile stress has been predicted at the oxide-alloy interface, which is consistent with the experimental observation. However, an understanding of defect evolution of defects is still needed necessarily, especially regarding the parameters that affect the failure driving force.

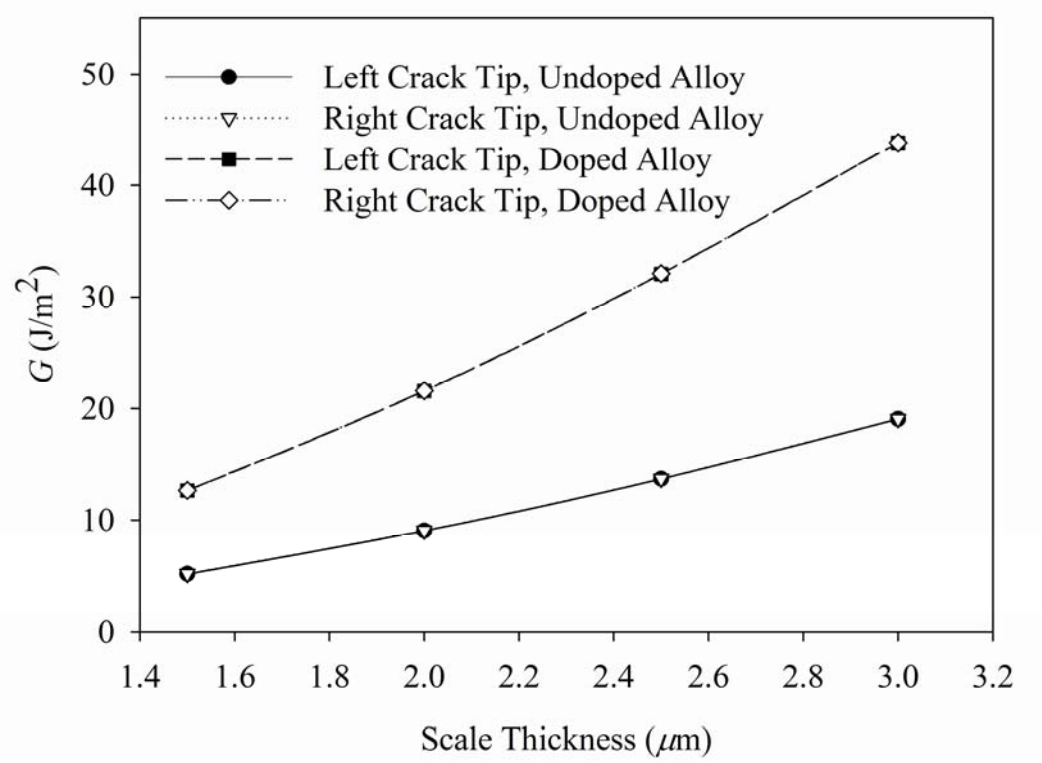

Figure 5.5 Energy release rate change with oxide scale thickness.

The energy release rate *G*, defined as energy dissipated during fracture, is considered as the crack growth driving force in this study. By definition, the energy

release rate can be evaluated by the ratio between the overall strain energy change of the whole system and the crack propagation area. For a model of elastic-plastic Fe-Cr alloy carrying a scale of thickness h=1μm, with half crack a=20μm, the energy release rate is obtained as 8.9 J/m^2.

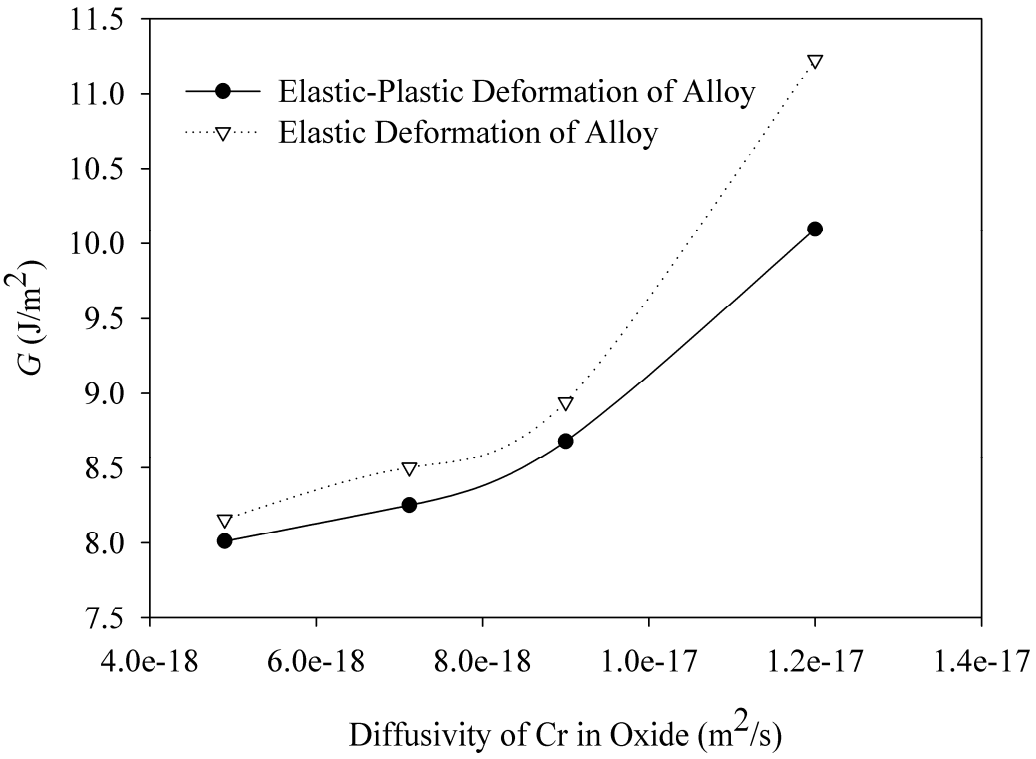

Figure 5.6 Energy release rate change with diffusivity.

For the growth of an interfacial crack, it is necessary to examine whether this crack experiences a stable crack growth or undergoes a stable fracture process. Figure 5.3 shows the variation of energy release rate along with the crack growth for doped and undoped Fe-Cr alloys at 1073K when the oxide scale has consistent thickness.

Due to symmetry, the energy release rates of the left and the right ends are almost identical, which could be also observed in later results. As seen, the energy release rates of both the left and the right cracks increase with the growth of crack. This means that for any given crack with certain crack length, if the energy release rate is initially smaller than the critical value G_c, the crack rests.

As discussed in chapter 4, a reactive element dopant such as yttrium has an important effect on oxide scale protection. One of the explanations is that the dopant would help to reduce the failure driving force. However, it draws immediate attention that in Figure 5.3 the energy release rate obtained from a doped alloy is about three times that obtained from an undoped alloy. This seems different from intuition because the result predicts that under the same conditions the oxide on doped alloy will trend to spall off easily. The reason is that the oxide scales on both alloys are assumed to be the same. Comparing the oxidation kinetics of doped and undoped alloys (Figure 4.6), we can find that it takes much more time for the doped alloy to form the same thickness of oxide as does the undoped alloy. This means that in reality the doped alloy experiences much longer time of oxidation, and therefore, it shows higher tendency for crack growth. To demonstrate the reactive element effect on the fracture driving force G, it is better for us to compare the results in the situation that the alloys experience oxidation for the same period of time. Since all the simulations are carried out with time independence, a compromise which we call the “same time rule” is made. From the oxidation kinetics in chapter 3, a 1.5μm oxide scale is formed on pure alloy after 500 hours of oxidation. In contrast, for doped alloy, a 0.8 μm oxide

scale is predicted from the results in chapter 4 after the same time of oxidation. We then obtained the *G-a* relation with h=1.5μm for pure alloy and h=0.8 μm for doped alloy, which is plotted Figure 5.4. Now we can see that after the same period of oxidation, the oxide-doped alloys model supplies less energy driven force for spallation.

The previous has shown not only that the crack length can affect the energy release rate of the interfacial crack, but that it may enable the oxide scale thickness to have its impact. Figure 5.5 shows the relation between the energy release rate of the interfacial crack and the oxide scale thickness. Accompanying the growth of scale thickness, the energy release rate increases. Hence, we can say that in the oxidation process an existing crack defect will be subject to an increasing crack-extension driving force when the oxide scale keeps growing. The comparison in Figure 5.5 shows that doped alloy has a higher energy release rate than the undoped alloy at the same oxide scale level, which is consistent with the discussion on Figure 5.3. Furthermore, the energy release rate obtained from doped alloy is more sensitive to the change of scale thickness. This may be because the strain energy density in the oxide-doped alloy model is greater than that in the oxide-pure alloy model. Hence, the variation of strain energy per unit extension area for crack between oxide and doped alloy is higher than for cracks between oxide and pure alloy.

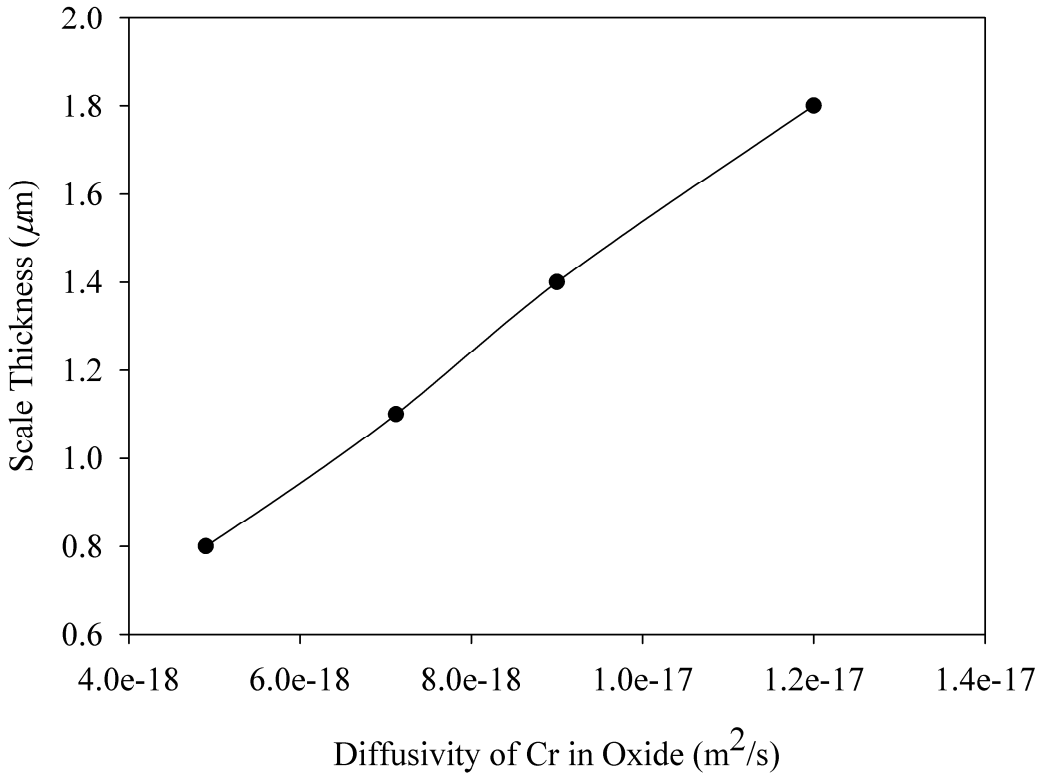

Figure 5.7 Corresponding oxide scale thickness for diffusivity of Cr in oxide.

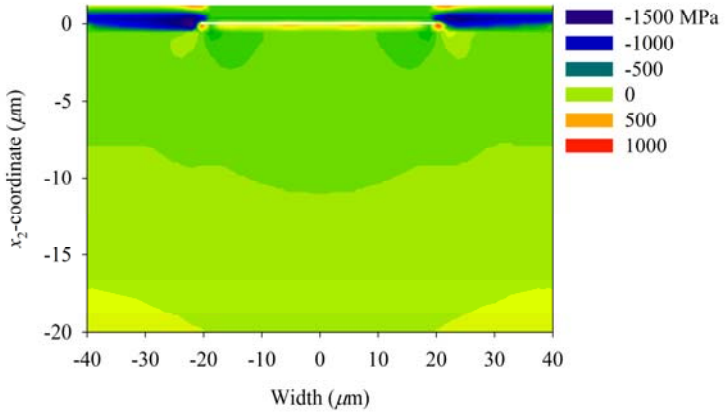

(a)

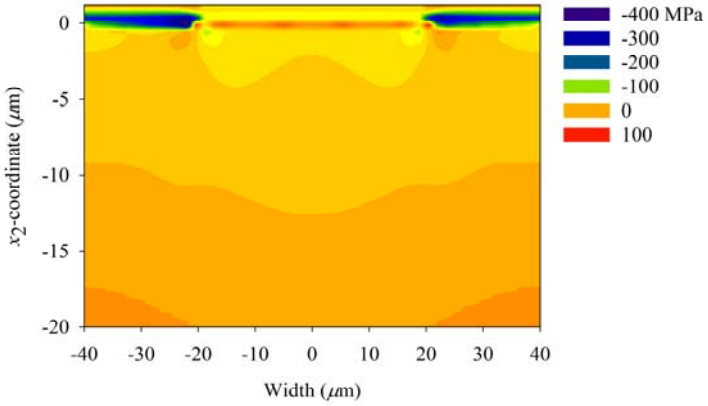

(b)

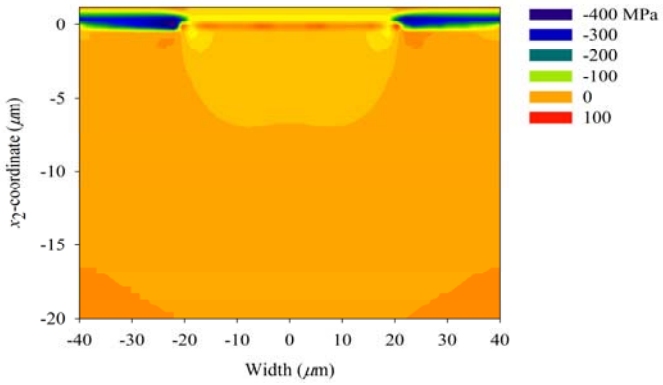

(c)

Figure 5.8 (a) Distribution of σ_{11} when alloy is elastic. (b) Distribution of σ_{11} when alloy is elastic-plastic. (c) Distribution of σ_{11} when alloy is elastic-plastic with yttrium dopant.

For a specific alloy, the thickness of its oxide scale after oxidation increase with the oxidation time; while for different alloys, their oxide thicknesses after the same time of oxidation vary due to different rates of ionic diffusion. The impact of diffusivity differences on oxidation kinetics may eventually be observed in their effects on interfacial crack growth driving force. Figure 5.6 gives the relation between energy release rate and the overall diffusivity of Cr ions in oxide scale at $1073K$. The variation of diffusivity may originate from the variations in the dopant content in the alloy, which has been discussed in chapter 4. The energy release rate G is calculated based on the "same time" rule, i.e., for each diffusivity, we obtain the oxide scale thickness (given in Figure 5.7) from the kinetics calculation of 500 hundred hours of oxidation and then use this scale thickness in finite element analysis for its corresponding energy release rate. The results in Figure 5.6 show that under the same conditions, a crack with pure elastic alloy substrate has more failure driving force than one with an elastic-plastic alloy substrate, i.e., the plasticity of alloys help prevent the crack from growing. For both curves in Figure 5.6, a trend of increasing slope is observed. This means that after same time period of oxidation, faster diffusion of species will lead to a higher level of interfacial failure driving force. Observations on stress distribution in oxide and alloy structures have further proved this. Distribution of σ_{11} in oxide scale with elastic alloy, elastic-plastic alloy and elastic-plastic doped alloy are plotted in Figure 5.8 (a), (b) and (c) respectively. Comparison between Figure 5.8 (a) and (b) illustrate that plasticity helps to reduce the maximum tensile and compressive stresses. Further reduction of maximum stress

magnitude can be found in (c), i.e., the additive dopants could lead to lower stress generation and hence lower failure. This is consistent with the trend predicted in Figure 5.9. The stress σ_{22}, generated as the consequence of in plane stress and chemical origins, shows a similar decreasing trend, especially for σ_{22} around the crack tip. The plasticity trims down a huge magnitude of interfacial tensile stresses from those induced in the elastic case.

The asymptotic stress field around the crack tip has also been obtained for possible failure mode analysis. The measure of mode mixity ψ with a reference length *L* from the crack tip is given as [131]

$$\psi = \tan^{-1}\left\{\frac{\mathrm{Im}\left[\left(K_1 + iK_2\right)L^{i\varsigma}\right]}{\mathrm{Re}\left[\left(K_1 + iK_2\right)L^{i\varsigma}\right]}\right\} \qquad (5.43)$$

where K_1 and K_2 are the stress intensity factors, *L* is a reference length, $i = \sqrt{-1}$. When the distance from the crack tip along the interface is *L*, the mode mixity is reduced to

$$\psi_L = \tan^{-1}\left\{\frac{\sigma_{12}}{\sigma_{22}}\right\} \qquad (5.44)$$

Due to freedom in choice of *L*, the mode mixity at any radius *r* along the interface is then obtained as

$$\psi = \psi_L + \varsigma \ln\left(\frac{r}{L}\right) \qquad (5.45)$$

Following [132], we set the reference length *L* to be the plastic zone size, which is given as

$$L = \frac{K_{el}^2}{2\pi\tau_0^2} \qquad (5.46)$$

where K_{el} is the magnitude of the complex stress intensity factor, τ_0 is the alloy yield stress in shear.

Figure 5.10 (a) gives the mode of mixity along the oxide-alloy interface in front of the crack tips. The modes of mixity for both tips are very close to mode II with the values close to 90^o and -90^o respectively. The mixed mode curve for the right tip of the crack is re-plotted in Figure 5.10 (b) for more details. Both of these figures show that shear stresses have stronger effect along the alloy-scale interface and that this effect decrease a little along with the increase of distance from the crack tip. This can be accounted for by the trend of volume expansion of scale layer and the trend of volume contraction of the alloy substrate.

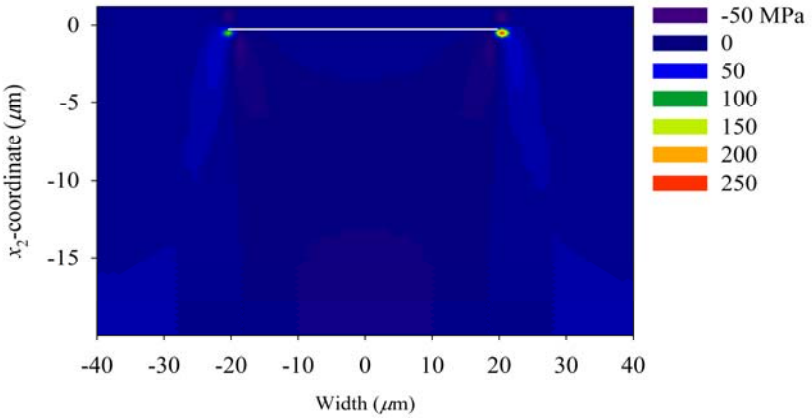

(a)

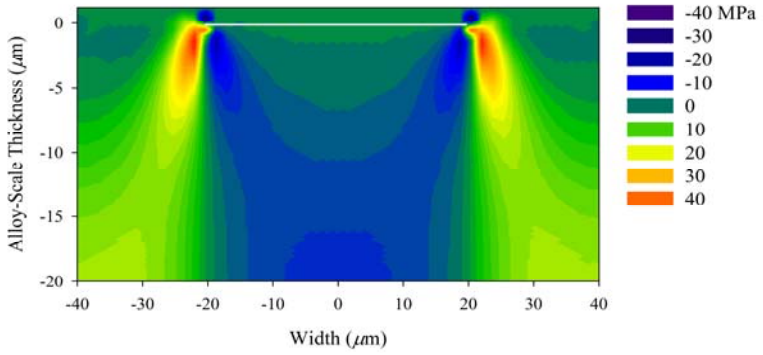

(b)

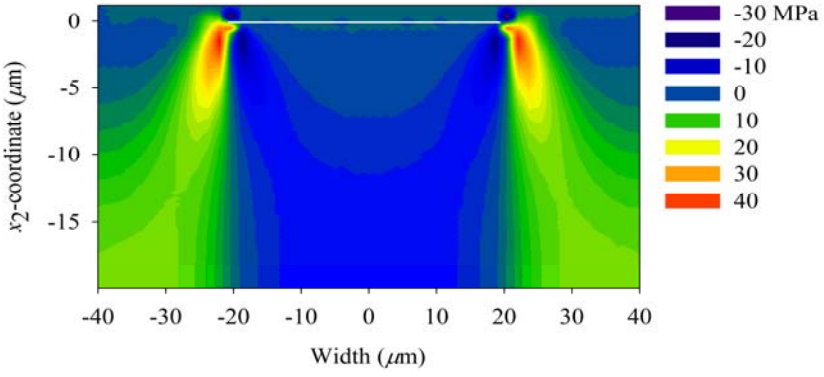

(c)

Figure 5.9 (a) Distribution of σ_{22} when alloy is elastic. (b) Distribution of σ_{22} when alloy is elastic-plastic. (c) Distribution of σ_{22} when alloy is elastic-plastic with yttrium dopant.

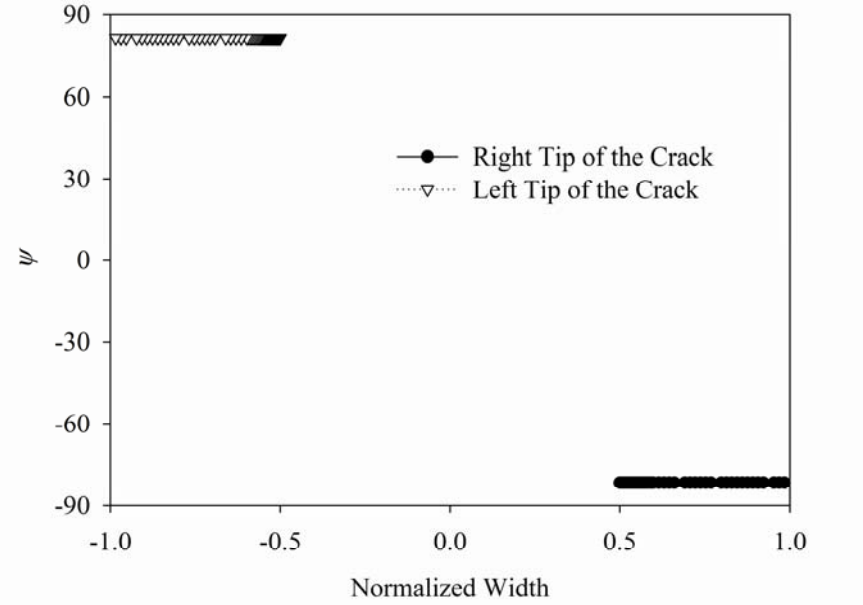

(a)

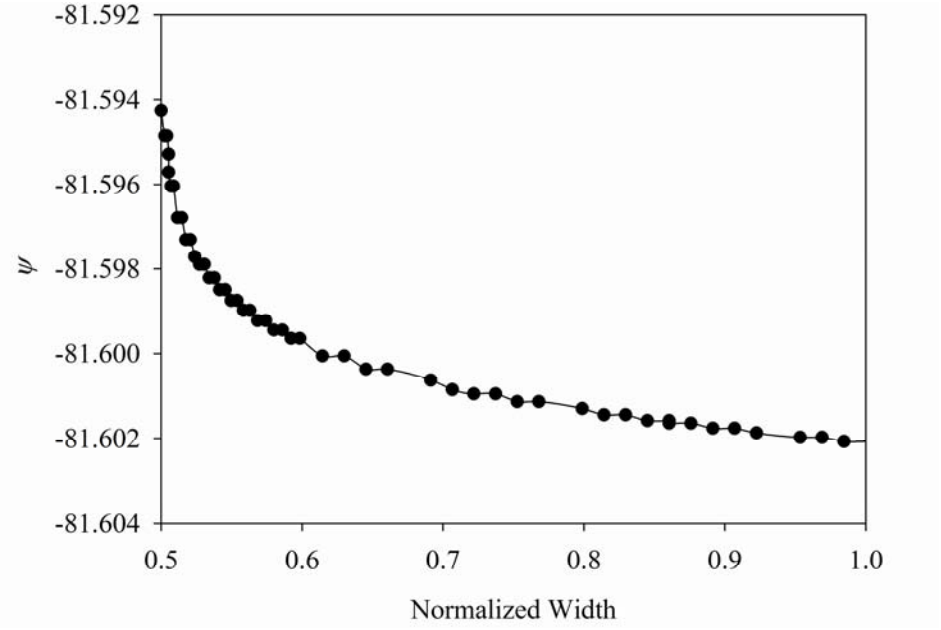

(b)

Figure 5.10 (a) mode of mixity along oxide-alloy interface. 10(b) mode of mixity along oxide-alloy interface in front of the right tip of the crack.

The angular variations of normalized stresses $\sigma_{r\theta}/\sigma_{\max}$ and $\sigma_{\theta\theta}/\sigma_{\max}$ are obtained and plotted in Figure 5.11, where $\sigma_{\max}$ is the maximum magnitude of the stresses. Due to the symmetry of the crack about x_1=0, the normal stresses $\sigma_{\theta\theta}$ around the two tips are almost identical while the shear stresses are anti-symmetric to each other. Hence the analysis is only focused on the right tip. The highest shear stress occurs aroud $\theta = 0^\circ$ while the highest normal stresses is reached at $\theta \approx 20^\circ$, which is in the elastic oxide scale right above the crack tip; besides, the oxide scale experience tensile stress at the crack tip. In the elastic-plastic alloy part, the alloy first experiences a tensile stress ahead the crack tip. The normal stress $\sigma_{\theta\theta}$ then rapidly changes to compressive, which may be attributed to the consequence of yielding and causes a possible crack tip closure.

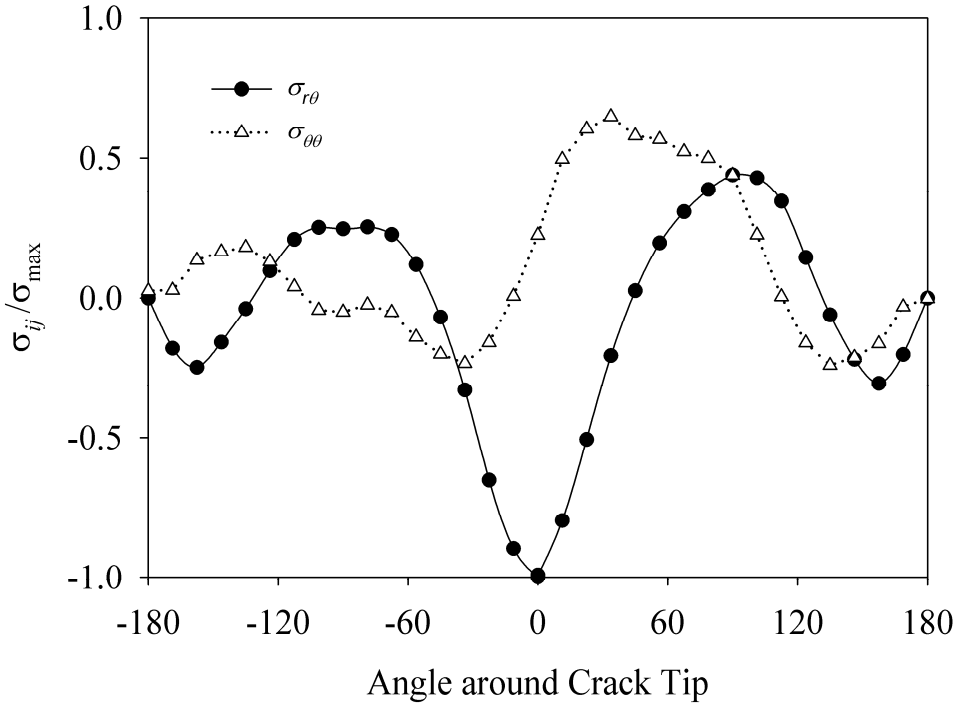

Figure 5.11 Angular variation of normalized stresses near the right tip of a center crack.

5.5 A Comprehensive Reactive Element Effects during Oxidation of Binary Alloy

5.5.1 Grain Refinement

Oxide grain refinement is one of the phenomena that have been often observed in oxidation experiments using reactive element (Y, Nd, Ce, etc.) doped alloys. Stroosnijder et al. [133] compared the oxidation of yttrium-doped and undoped chromium in air at 900^{o}C and observed that a small equiaxed grain structure of the scale grew on the Y containing alloy instead of the large columnar grain structure

scale on the undoped one. A better observation of the grain sized effect could be found in the works of Chevalier et al. [76, 134-135]. They observed the Nd2O3 coated Fe-30wt.% alloy and found that the size of Cr2O3 grain was effectively reduced from the level of 10 μm to the level of 1 μm, as shown in Fig 5.1.

Explanations [133, 136-137] have been proposed for the grain size effects. Pint and Alexander [136] attributed the small grain size to the inhibit of grain boundary segregation. They proposed that the large reactive element particle segregated at the grain boundary prevents oxide grain growth and thus leads to smaller grains. However, most researchers [133, 137] have agreed that the small grain size originates from inward anion diffusion. The reactive element oxide compound emerging at the grain boundaries, such as $NdCrO_3$ [138], drastically reduces the diffusion transport of metal cation by blocking these fast diffusion areas. As a consequence, it eventually changes the oxidation from dominant cation transport to dominant anion transport. Due to this modification of the grain boundary transport mechanism, together with the small interior growth space, the grain size trends to be small. Another plausible mechanism for the change of ionic transport comes from the work of Pieraggi and Rapp [17, 120]. They attributed the growth of cation-diffusing scales to the metal vacancy mechanism [17]. Metal vacancies are generated at the scale-gas interface and are eliminated at the alloy-scale interface by the climb into the alloy of the intrinsic misfit dislocations. The reactive element ions or their compounds segregated at the alloy-scale interface pin the misfit dislocations and keep them from climbing into the alloy [120]. The misfit dislocations, therefore, are not able to serve

as the sinks of cation vacancies. Hence, instead of cation diffusion, the anion inward diffusion becomes dominant to support the growth of oxide scale.

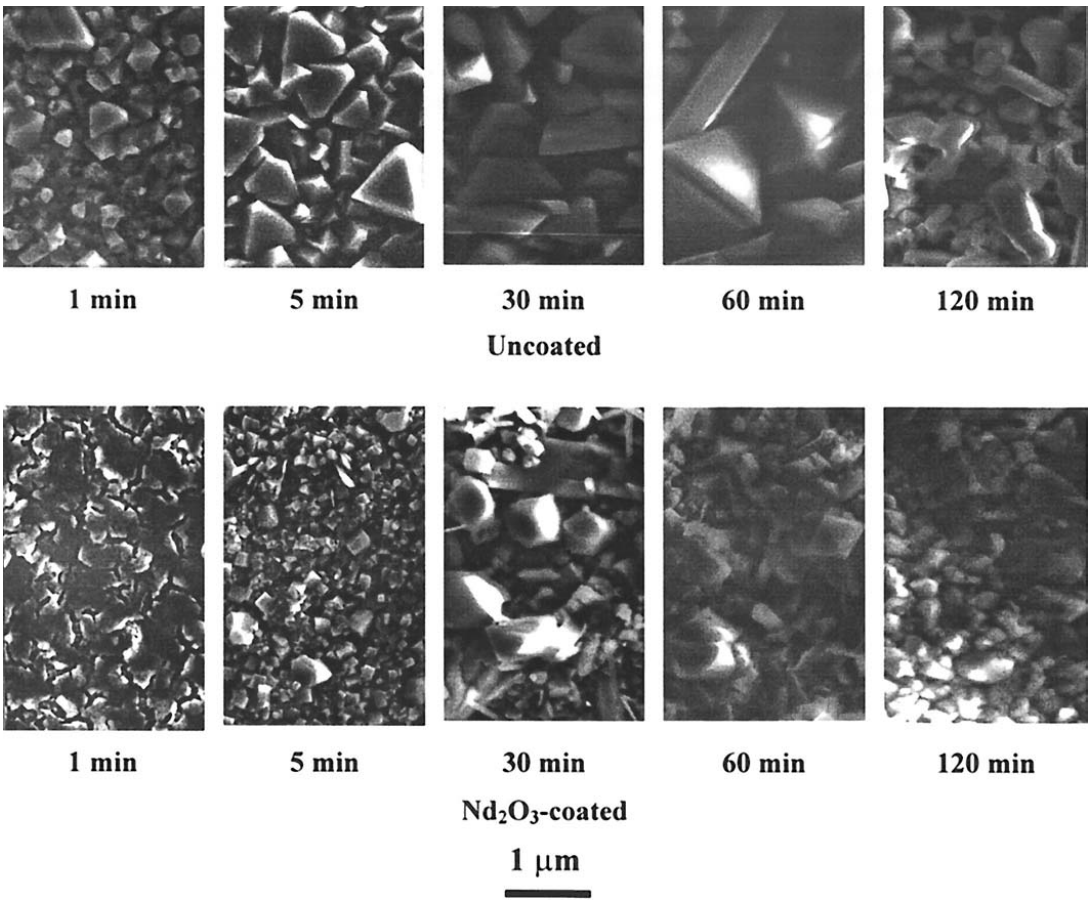

Figure 5.12 Grain size refinement with reactive element oxide dopant [135]

5.5.2 Reduce of diffusivity

Though the reactive element effect in the oxide appears as a change of the crystal structure of the oxide scale and the oxide mechanism, essentially, the reactive element effect is the change of transport properties of the electronically charged

species in the oxide scale. The overall transport property of diffusible species in the oxide, the diffusivity, is typically determined by two factors: The local diffusivities in different crystal structure areas (e.g. grain bulks, grain boundaries) and the ratio of different structural areas.

Many works [7, 24, 80, 139] have been done to experimentally measure the diffusivities of ions in the oxide. Czerwinski and Szpunar [139] observed the controlling effect of the CeO_2 on grain boundary diffusion in oxide films. Based on the method from Atkinson and Taylor [140], they estimated the grain boundary diffusivity of the metal ion. It is suggested that the Ce^{+4} ions block the outward diffusion of metal ion along oxide grain boundaries. Park et al.[141] determined the cation diffusivity in grains and along grain boundaries on sintered Cr_2O_3-0.09wt.% Y_2O_3 at 1100 ^oC and the p_{O_2} corresponding to that of Cr/Cr_2O_3 equilibrium at that temperature. The results indicated that the presence of Y has a negligible effect on lattice diffusion. However, for grain boundary diffusion, Y containing oxide has a faster cation transport rate. A more comprehensive measurement of yttrium's effect on ionic diffusion can be found in the work of Huntz and his colleagues [7, 24]. They determined the diffusivities along Cr_2O_3 grain boundaries at 800 ^oC and 900 ^oC by using ^{18}O and ^{54}Cr tracers. Their results showed that the yttrium inhibited both cation diffusion and anion diffusion. The diffusion of chromium ions is still faster than that of the oxygen ion in oxide grain boundaries. So, based on their observations, they argued that Cr_2O_3 scale growth is controlled by counter-current diffusion of oxygen and chromium.

Even though different researchers have obtained different conclusions on the reactive element effect, it is a common conclusion that the effect is mostly realized at the change of grain boundary ionic diffusion. To evaluate the grain boundary diffusion change towards the overall diffusivity and eventually the overall oxide kinetics, one need to include this effect together with the ratio of different diffusion areas and also the possible grain size effect. This leads to the necessarity of a geometric study of polycrystalline solids. An early model for diffusion through a crystalline structure was established by Fisher, who considered a semi-infinite solid with a single fast diffusing grain boundary embedded in a bulk of much lower diffusivity [38]. Many subsequent studies [39-40] examined the same basic geometry with less restrictive boundary conditions. The simplest geometry for polycrystalline diffusion that can be captured is a system of parallel grain boundaries, such as a columnar structure. This geometry was adopted in many studies [42-43, 142] that focus on diffusion through polycrystalline films, and it was concluded that a bulk containing parallel grain boundaries behaves like a homogeneous diffusing system with an effective diffusivity D_{eff}. The most widely used model [41-42] for D_{eff} depends on the bulk diffusivity D_B, grain boundary diffusivity D_{gb} and the volume fraction of grain boundaries f, i.e.

$$D_{eff} = (1-f)D_B + fD_{gb} \qquad (5.47)$$

However, Chen and Schuh [143] pointed out that (5.47) is the upper bound of the effective diffusivity. It is only accurate for the parallel grain boundary polycrystalline model. For more general grain-grain boundary geometries, such as

voronoi tessellation, the interconnections between grain boundaries have to be included. The effective diffusivity is therefore given as

$$D_{eff} = (1-f)D_B + fD_{gb} + \frac{f(1-f)(D_{gb}-D_B)^2}{f(D_{gb}-D_B)-3D_{gb}} \qquad (5.48)$$

with the third term on the right hand side as the counter part for lateral interconnections between grain boundaries. The volume fraction can be further related with the microstructural descriptor, i.e.

$$f = H_{gb}\frac{\delta}{g} \qquad (5.49)$$

where H_{gb} is a dimensionless numerical factor, δ and g are the grain boundary thichness and the grain size respectively. After substitution of (5.49) into (5.48), one may obtain the explicit expression of the effective diffusivity as the function D_B, D_{gb}, δ and a, i.e.

$$D_{eff} = \left(1-H_{gb}\frac{\delta}{g}\right)D_B + H_{gb}\frac{\delta}{g}D_{gb} + \frac{H_{gb}\frac{\delta}{g}\left(1-H_{gb}\frac{\delta}{g}\right)(D_{gb}-D_B)^2}{H_{gb}\frac{\delta}{g}(D_{gb}-D_B)-3D_{gb}} \quad . \qquad (5.50)$$

Note that $D_B << D_{gb}$ for both Cr and O ions in doped and undoped Cr_2O_3 scale [7], one may simplify (5.50) to

$$D_{eff} = D_B + H_{gb}\frac{\delta}{g}\left[1-\frac{1-H_{gb}\frac{\delta}{g}}{3-H_{gb}\frac{\delta}{g}}\right]D_{gb}, \qquad (5.51)$$

which clearly illustrates that the interconnections between grain boundaries reduce the effective diffusivity. When the volume fraction of grain boundaries $H_{gb}\frac{\delta}{g} << 1$, which is usually the case for undoped oxide scale, we find from (5.51) that the

decrease of local diffusivity would reduce the diffusivity while the refinement of crystal structure increases the effective diffusivity.

In this study, the effective diffusivities of Cr and O ions in oxide grain boundaries will be obtained and used in the later simulations. The diffusivity of Cr D_{gb} in oxide grain boundaries will first be evaluated using the method in [144]. D_B is assumed to be unaffected by the reactive element dopant and obtained from [7]. The overall effective diffusivity of Cr can then be obtained from (5.50) with given crystal structure. For the effective diffusivity of the O ion, we may use a similar procedure. However, for necessary simplification, the classic Wagner's approach [118] will be used here.

5.5.3 Reactive element effect on interfacial adhesion

Enhancement of the scale-alloy interface adherence is another important effect that has been attributed to the reactive element effect. It presents as the better resistance to oxide scale spallation, especially during cooling from high temperature [31]. Researchers have developed many possible mechanisms to explain this improvement of adhesion. Due to the change of crystal structure and refinement of grains, one possible explanation was related to the dependence upon energy increase of the interfacial chemical bonding. However, the atomic computation upon the work of adhesion between thermally grown oxides and the alloys indicated that the reactive elements only have limited influence on the adhesive energy [145-146]. Experimentally, Tien and Pettit [147] demonstrated that Al_2O_3 showed similar effects

on adhesion of Cr_2O_3 on chromia forming alloys.

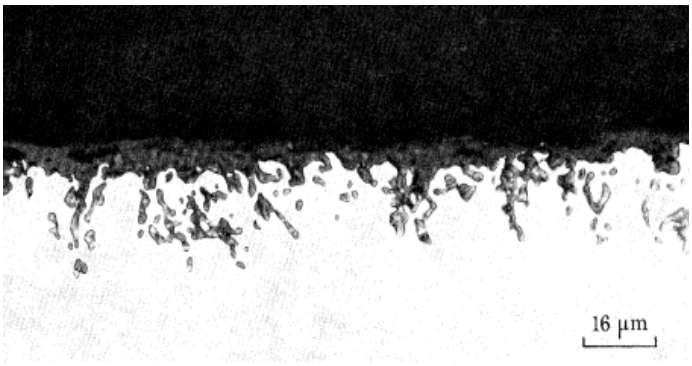

Figure 5.13 Interfacial pegs formation for Co-10Cr-11Al [148]

Another possible explanation of good interface adhesion is based on the mechanism change of oxide scale, especially for Cr_2O_3 forming alloy. As a result of the internal oxide growth on the doped alloy, the oxide scale is continuously attached with the alloy substrate. Unlike the oxidation of undoped alloy, discussed in [149], vacancies rarely coalesce to form interfacial voids. Instead, the oxide scale penetrates in the alloy and forms pegs. The keying effect of pegs improves the interfacial adhesion. Pegs are often observed from the oxidation of yttrium doped Al_2O_3 forming alloys, such as the one shown in Figure 5.13. Cr_2O_3 pegs are rarely reported [137, 150]; however, since the oxygen ions are mostly transported inward via the scale grain boundaries, the keying effect and formation of pegs is inevitable. As shown in [151], the Cr_2O_3 scale-alloy interface gradually develops into uneven surface with oxide keying in the alloy around the scale grain boundaries.

Following the approaches of [152-153], in this study, we use a periodic morphology in the finite element computation to mimic the interfacial pegs, as shown in Figure 5.14.

5.5.4 Reactive element effect on alloy creep

As shown in the previous study, a high level of stress is generated in the alloy substrate, especially around the scale-alloy interface. At temperature over 800 ^{o}C, creep would always occur under this level of stresses. Pieraggi and Rapp [17] explained that the creep was generated by the return of the dislocations climbing into the metal from the interface via glide. Therefore, based on the reactive element effect explained in [120], conclusion could be drawn that the existence of reactive element at the interface could reduce the creep. Dunand and his coworker [154-155] disclosed that reactive elements could lead to precipitants in Al-Sc alloys such that the creep performance of alloys could be changed. Micromechanics is an effective approach for evaluating the overall mechanical performance of reactive-element doped materials. For example, the homogenized method [156] is adopted to obtain a representative constitutive relation for the creep of SnAg alloy. However, for the specific materials we are interested in, the Fe-Cr alloys, the dispersion particle (such as Y_2O_3) are typically as small as the nanometer level [157]. For a typical power law creep, dislocation movement is the major contribution to the creep strain [142]. The segregated reactive element addictives in the alloy matrix hence act as barriers for the slip of dislocations [158].

In this study, the dispersion particle geometry is assumed to be the same as that used in [159], i.e. a cubic shaped particle with surfaces inclined at an angle β to the slip plane and with edge length *d*. So the distance between top of the inclined surface and the slip surface is

$$h = d\sin\beta \tag{5.52}$$

To describe the creep rate due to dislocation movement, the Orowan equation [158, 160-161] is adapted, i.e.

$$\dot{\varepsilon}'_p = \rho b \frac{1}{1-\sigma^t/\sigma^t_{Or}} v \tag{5.53}$$

where $\dot{\varepsilon}'_p$, are the creep strain rates, σ^t are the shear stresses and σ^t_{Or} is the effective Orowan stress given as,

$$\sigma^t_{Or} = \frac{Gb}{2\lambda}, \tag{5.54}$$

where *b* is the magnitude of the Burgers vector, *G* is the shear modulus, and 2λ is the mean planar spacing. The density of mobile dislocations ρ is given as [161]

$$\rho = \left(\frac{\sigma^t}{Gb}\right)^2 \tag{5.55}$$

The dislocation velocity *v* is estimated as [159]

$$v = 2\lambda \frac{Gb^4}{d^3} C_i A \left(\frac{\sigma^t - \sigma^t_{th}}{\sigma^t_{Or}}\right)^n, \tag{5.56}$$

where C_i is a kinetic constant, other constants can be given as

$$n = 3.5\beta^{0.3}\left(\frac{h}{d}\right)^{0.2} \tag{5.57}$$

and

$$A = 60\times 10^{-1.9\beta}\left(\frac{d}{h}\right)^{1.6} \tag{5.58}$$

The threshold stress

$$\sigma_{th}^{t} = \frac{h}{\lambda}\sigma_{Or}^{t}. \tag{5.59}$$

If the isotropic Von Mises yield criterion is adopted here,

$$\dot{\varepsilon}_{ij}^{p} = \frac{3}{2}\frac{\dot{\bar{\varepsilon}}^{p}}{\bar{\sigma}} S_{ij}. \tag{5.60}$$

where $\dot{\bar{\varepsilon}}^{p}$ is the effective strain rate and $\bar{\sigma}$ is the effective stress. From equation (5.53) and (5.56), we have the relationship

$$\dot{\bar{\varepsilon}}^{p} = \rho b \frac{1}{1-\bar{\sigma}/M\sigma_{Or}^{t}} 2\lambda \frac{Gb^{4}}{d^{3}} C_{i} A \left(\frac{\bar{\sigma}}{M\sigma_{Or}^{t}} - \frac{h}{\lambda} \right)^{n} \tag{5.61}$$

where *M* is the Taylor Factor. So the creep strain rate from (5.60) and (5.61) is then obtained as

$$\dot{\varepsilon}_{ij}^{p} = \frac{3}{2}\rho b \frac{1}{\bar{\sigma}\left(1-\bar{\sigma}/M\sigma_{Or}^{t}\right)} 2\lambda \frac{Gb^{4}}{d^{3}} C_{i} A \left(\frac{\bar{\sigma}}{M\sigma_{Or}^{t}} - \frac{h}{\lambda} \right)^{n} S_{ij} \tag{5.62}$$

5.6 Two-dimensional implementation considering reactive element effects

In this section, we revisit the two dimensional form of the oxidation theory with two considerations. First, we include the inelastic deformation; here we specify the deformation as high temperature creep behavior of substrate alloy. Second, the aforementioned reactive element effects on high temperature oxidation of alloys are integrated in the current implementation. The effect on microstructure and diffusivities is accounted for by adopting equation (5.50) and the oxide grain boundary diffusivity we obtained in [144]. The interfacial peg geometry is considered as an uneven interface, as shown in Fig. 5.3. For the dispersion enhanced creep, the creep of alloy with Y_2O_3 particles follows the relation in equation (5.62).

In the previous study, the scale-alloy interface is fixed in the coordinates, because the oxide mainly grows at the scale-gas surface such that the inward growth can be ignored. However, in this study, the scale growth mechanism switches to inward oxygen diffusion dominant growth. Therefore, we have to consider the interface to be moving, which make this implementation different from those in previous studies.

For simplification and clarification, we need some assumptions used in this study. First, the moving velocity for the bulk of the oxide is ignored. The inward scale growth is treated as the phase transformation due to oxidation. Cr below the interface gets oxidized and converts into oxide locally, which moves the scale-alloy interface but does not change the special position of the bulk oxide. Secondly, the scale-alloy interface movement is controlled by the local oxygen flux which is not considered to cease at the interface any more. Instead, we consider a different boundary condition for oxygen ions at the scale-alloy interface. We assume that at any instantaneous time, the oxide concentration at the interface follows the Pilling and Bedworth ratio and thus is a fixed value. The chemical potential of the oxygen ions is in equilibrium with those of the oxide and Cr ions.

5.6.1 Governing equations in two dimension

In oxide scale, the mass continuity equations for Cr and O ions are given as

$$\frac{\partial c_{\mathrm{Cr}}}{\partial t} = D_{Cr}\left[\frac{\partial}{\partial x_1}\left(\frac{\partial c_{Cr}}{\partial x_1} + c_{Cr}\frac{V_{Cr}^m}{RT}\frac{\partial \tau_{Cr}}{\partial x_1}\right) + \frac{\partial}{\partial x_2}\left(\frac{\partial c_{Cr}}{\partial x_2} + c_{Cr}\frac{V_{Cr}^m}{RT}\frac{\partial \tau_{Cr}}{\partial x_2}\right)\right]$$
$$\frac{\partial c_{\mathrm{O}}}{\partial t} = D_{O}\left[\frac{\partial}{\partial x_1}\left(\frac{\partial c_{O}}{\partial x_1} + c_{O}\frac{V_{O}^m}{RT}\frac{\partial \tau_{O}}{\partial x_1}\right) + \frac{\partial}{\partial x_2}\left(\frac{\partial c_{O}}{\partial x_2} + c_{O}\frac{V_{O}^m}{RT}\frac{\partial \tau_{O}}{\partial x_2}\right)\right]. \quad (5.63)$$

where the overall diffusivity D_s in the oxide is given by (5.50).

In an alloy substrate, the mass continuity equations for Cr atoms and O ions are given as

$$\frac{\partial c_{Cr(a)}}{\partial t} = D_{Cr(a)}\left[\frac{\partial}{\partial x_1}\left(\frac{\partial c_{Cr(a)}}{\partial x_1} + c_{Cr(a)}\frac{V_{Cr(a)}^m}{RT}\frac{\partial \tau_{Cr(a)}^a}{\partial x_1}\right) + \frac{\partial}{\partial x_2}\left(\frac{\partial c_{Cr(a)}}{\partial x_2} + c_{Cr(a)}\frac{V_{Cr(a)}^m}{RT}\frac{\partial \tau_{Cr(a)}^a}{\partial x_2}\right)\right] \quad (5.64)$$

The stress-dependent part of the chemical potential, for constant linear elastic and small strain deformation, is given as

for species in oxide

$$\tau_s = \eta_s\left[\frac{3}{2}c_{ijkl}\,\varepsilon_{ij}^e\varepsilon_{kl}^e - \sigma_{kk}\right] \quad (5.65)$$

for species in alloy

$$\tau_s^a = \eta_s\left[\frac{3}{2}c_{ijkl}\,\varepsilon_{ij}^e\varepsilon_{kl}^e + 3\int \sigma_{ij}d\varepsilon_{ij}^p - \sigma_{kk}\right] \quad (5.66)$$

In the whole field, the stress equilibrium equations have to be satisfied, i.e.

$$\frac{\partial \sigma_{11}}{\partial x_1} + \frac{\partial \sigma_{12}}{\partial x_2} = 0$$
$$\frac{\partial \sigma_{21}}{\partial x_2} + \frac{\partial \sigma_{22}}{\partial x_1} = 0 \quad (5.67)$$

The corresponding constitutive relations and the strain rate relationships are given as:

in oxide

$$\sigma_{11} = \frac{E}{(1+\nu)(1-2\nu)}\left[(1-\nu)\left(\frac{\partial u_1}{\partial x_1} - \sum_s \eta_s \Delta c_s\right) + \nu\left(\frac{\partial u_2}{\partial x_2} - 2\sum_s \eta_s \Delta c_s\right)\right]$$
$$\sigma_{22} = \frac{E}{(1+\nu)(1-2\nu)}\left[(1-\nu)\left(\frac{\partial u_2}{\partial x_2} - \sum_s \eta_s \Delta c_s\right) + \nu\left(\frac{\partial u_1}{\partial x_1} - 2\sum_s \eta_s \Delta c_s\right)\right] \qquad (5.68)$$
$$\sigma_{12} = \frac{E}{2(1+\nu)}\left(\frac{\partial u_1}{\partial x_2} + \frac{\partial u_2}{\partial x_1}\right)$$

and

$$\varepsilon_{11}^E = \frac{\partial u_1}{\partial x_1} - \sum_s \eta_s \Delta c_s,$$
$$\varepsilon_{22}^E = \frac{\partial u_1}{\partial x_2} - \sum_s \eta_s \Delta c_s,. \qquad (5.69)$$
$$\varepsilon_{12}^E = \frac{1}{2}\left(\frac{\partial u_1}{\partial x_2} + \frac{\partial u_2}{\partial x_1}\right)$$

in alloy

$$\sigma_{11} = \frac{E}{(1+\nu)(1-2\nu)}\left[(1-\nu)\,\varepsilon_{11}^e + \nu\varepsilon_{22}^e\right]$$
$$\sigma_{22} = \frac{E}{(1+\nu)(1-2\nu)}\left[(1-\nu)\,\varepsilon_{22}^e + \nu\varepsilon_{11}^e\right] \qquad (5.70)$$
$$\sigma_{12} = \frac{E}{2(1+\nu)}\left(\frac{\partial u_1}{\partial x_2} + \frac{\partial u_2}{\partial x_1}\right)$$

$$\dot{\varepsilon}_{ij} = \dot{\varepsilon}_{ij}^e + \dot{\varepsilon}_{ij}^c + \dot{\varepsilon}_{ij}^p$$
$$\dot{\varepsilon}_{ij}^p = \rho b \frac{1}{\bar{\sigma}\left(1 - \bar{\sigma}/M\sigma_{Or}^t\right)} 2\lambda \frac{Gb^4}{d^3} C_i A\left(\frac{\bar{\sigma}}{M\sigma_{Or}^t} - \frac{h}{\lambda}\right)^n S_{ij} \qquad (5.71)$$
$$i, j = 1,2$$

With the chemical reaction equilibrium assumption, we have

$$d\mu_p - 2d\mu_{\mathrm{Cr}} - 3d\mu_{\mathrm{O}} = 0 \qquad (5.72)$$

in the oxide scale.

The interfacial boundary conditions are prescribed as

At the Metal-Scale Interface

Continuity of chemical potentials must hold between Cr ions and Cr atoms, i.e.

$$\frac{\mu^0_{\mathrm{Cr}(a)} - \mu^0_{\mathrm{Cr}}}{RT} + \ln\frac{c_{\mathrm{Cr}(a)}}{c_{\mathrm{Cr}}} = \frac{V^m_{Cr}\tau_{Cr} - V^m_{Cr(a)}\tau_{Cr(a)}}{RT} \quad . \tag{5.73}$$

Conservation of mass for Cr across the interface leads to

$$\frac{\partial c_{\mathrm{Cr}(a)}}{\partial x_2} + \frac{V^m_{Cr(a)} c_{\mathrm{Cr}(a)}}{RT}\frac{\partial \tau_{Cr(a)}}{\partial x_2} = \frac{D_{\mathrm{Cr}}}{D_{\mathrm{Cr}(a)}}\left[\frac{\partial c_{\mathrm{Cr}}}{\partial x_2} + \frac{V^m_{Cr} c_{\mathrm{Cr}}}{RT}\frac{\partial \tau_{Cr}}{\partial x_2}\right]. \tag{5.74}$$

Furthermore, per the assumption that no O can cross the interface into the metal, the O ion flux transforms all to oxide and must follow the Stefan [107] condition at the scale-alloy interface, i.e.,

$$\frac{2V^m_{Cr(a)}}{3} D_O\left(\frac{\partial c_{\mathrm{O}}}{\partial x_2} + \frac{V^m_O c_{\mathrm{O}}}{RT}\frac{\partial \tau_O}{\partial x_2}\right) = -\frac{du_2}{dt} \quad . \tag{5.75}$$

The oxide concentration at the interface follows the PBR, i.e.

$$\varepsilon^c = \left[\left(\mathrm{PBR}\right)^{1/3} - 1\right] \tag{5.76}$$

to estimate the interfacial chemical strain.

Finally, traction continuity is automatically satisfied by the choice of stress components, and the continuity of displacement leads to

$$u_1\big|_{x_2=0^+} = u_1\big|_{x_2=0^-}, u_2\big|_{x_2=0^+} = u_2\big|_{x_2=0^-} . \tag{5.77}$$

At the Scale-Air Interface

An equilibrium condition is assumed for the ionization of oxygen (in the air), i.e.,

$$\frac{1}{2RT}\mu^0_{\mathrm{O}_2} + \ln P^{1/2}_{\mathrm{O}_2} = \frac{\mu^0_{\mathrm{O}}}{RT} + \ln c_{\mathrm{O}} + V^m_O \tau_O \quad . \tag{5.78}$$

In addition, since the oxide forms at the surface, and since Cr ions cannot leave the scale, the Cr ion flux transforms all to oxide and must follow the Stefan [107]

condition at the scale-air interface, i.e.,

$$\frac{V_p^m}{2} D_{Cr} \left(\frac{\partial c_{\mathrm{Cr}}}{\partial x_2} + \frac{V_{Cr}^m c_{\mathrm{Cr}}}{RT} \frac{\partial \tau_{Cr}}{\partial x_2} \right) = -\frac{du_2}{dt} \quad . \tag{5.79}$$

Furthermore, the scale-air interface can be viewed as a traction free surface, which is satisfied by the choice of the stress components.

Inside the alloy far from the interface, $c_{Cr(a)} = C$ as $x_2 \to -\infty$. Additionally, periodic boundaries are applied at the left ($x_1 = -\frac{w}{2}$) and right ($x_1 = \frac{w}{2}$) hand side of the 2D model, i.e.,

$$\begin{aligned} &u_1\Big|_{x_1=-\frac{w}{2}} = u_1\Big|_{x_1=\frac{w}{2}}, u_2\Big|_{x_1=-\frac{w}{2}} = u_2\Big|_{x_1=\frac{w}{2}} \\ &c_{Cr}\Big|_{x_1=-\frac{w}{2}} = c_{Cr}\Big|_{x_1=\frac{w}{2}}, c_O\Big|_{x_1=-\frac{w}{2}} = c_O\Big|_{x_1=\frac{w}{2}}, c_{Cr(a)}\Big|_{x_1=-\frac{w}{2}} = c_{Cr(a)}\Big|_{x_1=\frac{w}{2}} \end{aligned} \quad . \tag{5.80}$$

5.7 Finite Element Implementation

5.7.1 Implementation description

The two dimensional diffusion-stress coupling model for steady state oxidation of a binary alloy was implemented by finite element method in the commercial software ABAQUS with a user defined element subroutine. Emphasis was put on the yttrium effect on scale growth and material performance. As shown in Figure 5.14, a layer of homogenized polycrystalline oxide growing on the top of a binary alloy is considered in this implementation. The alloy part is considered as a whole bulk. The scale-alloy interface is assumed to be a curve in some portion in this study to mimic the peg shape. The scale-alloy interface except for the peg portion is

assumed to be flat and is set as $x_2 = 0$ at time t=0. The initial oxide scale carried on the Fe-Cr-Y alloy beyond $x_2 = 0$ is 20 nm. The size for the initial peg shape is given in Figure 5.14 (b).

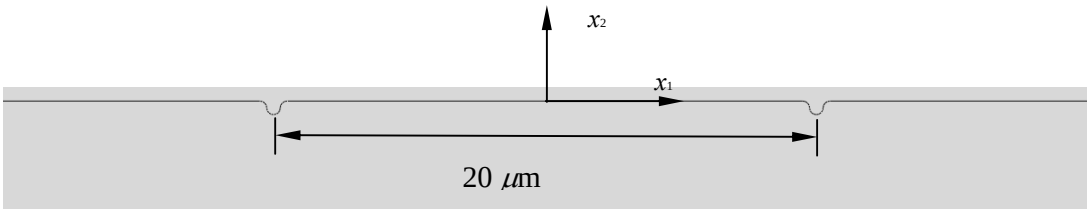

(a)

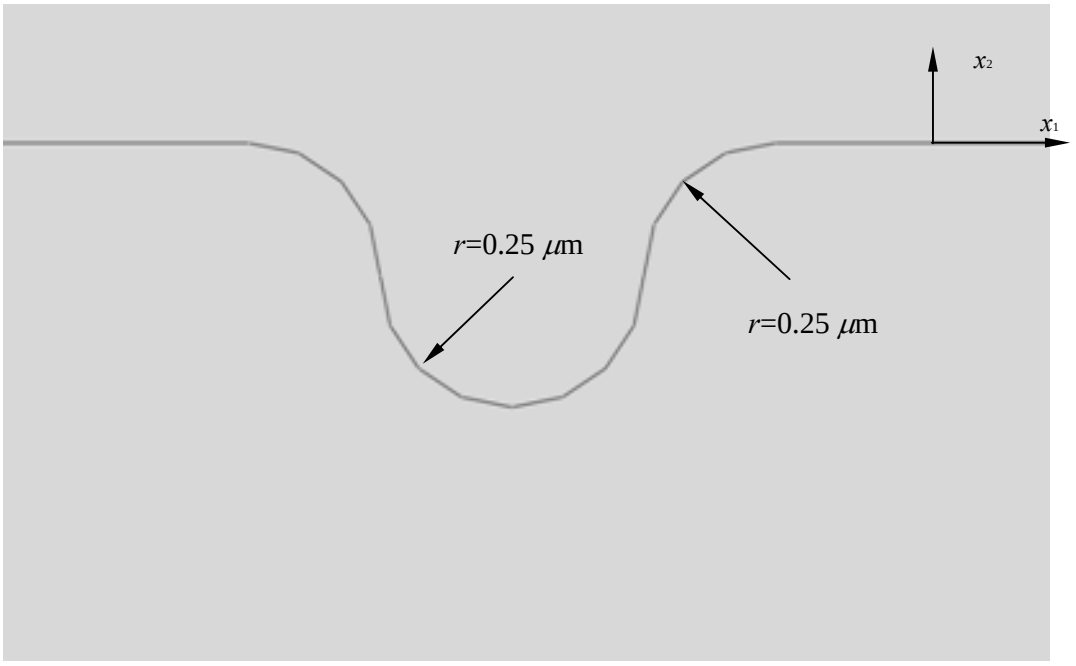

(b)

Figure 5.14 (a) Unflatted scale-alloy interface (b) local view of the unflatted surface

The elements beyond the scale-gas interface and below the scale-alloy interface are modeled with fine mesh and identical thickness in the x_2 direction. The oxide scale interface's upward movement is calculated by integrating equation (3.50) and the inward movement is calculated by (5.75). When the displacement exceeds the specified element thickness, the material properties of the elements (air or alloy) that are adjacent to the corresponding interfaces switch to oxide. The data used, including the parabolic coefficient k_p, oxygen ion diffusivities in oxide grain areas and grain-boundary areas, and the chromium ion diffusivity in oxide grain areas are estimated from [7], which are also listed in Table 4.1, all other material properties are listed in Table 5.1.

5.7.2 Results and Discussion

The simulation is first carried out for oxidation of Ni-Cr-Y alloy under 1073K for validation. The diffusivity of chromium ion in oxide grain boundary areas are obtained from our previous study in chapter 4. Here we relist it, i.e.,

$$D_{Cr} = \frac{k_p a_{Y_2O_3}^{1/8}}{4 f \Delta a} \qquad (5.81)$$

In this study, we use an average activity $a_{Y_2O_3}$ in the grain-boundary areas to obtain a average chromium diffusivity. We also assume the magnitude of $a_{Y_2O_3}$ is one tenth of that of Δa. Substituting the aforementioned quantities into (5.50), we can obtain the overall diffusivities for oxygen ion and chromium ions, and hence we can calculate the oxidation kinetics. Figure 5.15 gives a series of oxygen kinetics of the flat portion versus different average sizes of oxide grains. We also plot the

parabolic kinetics with the k_p we used in (5.81). The results indicate that for given diffusivities of species, the smaller the grain size, the more the scale grows. In this figure, we find that when g=2.43μm which corresponds to f=6E-4, the predicted kinetics matches the kinetics profile with prescribed k_p. Comparing the f value to the results in [7] which is in the range of 4.5E-4 to 5.0E-4, we found the ratio we estimated is fairly close to that obtaind in the experiments.

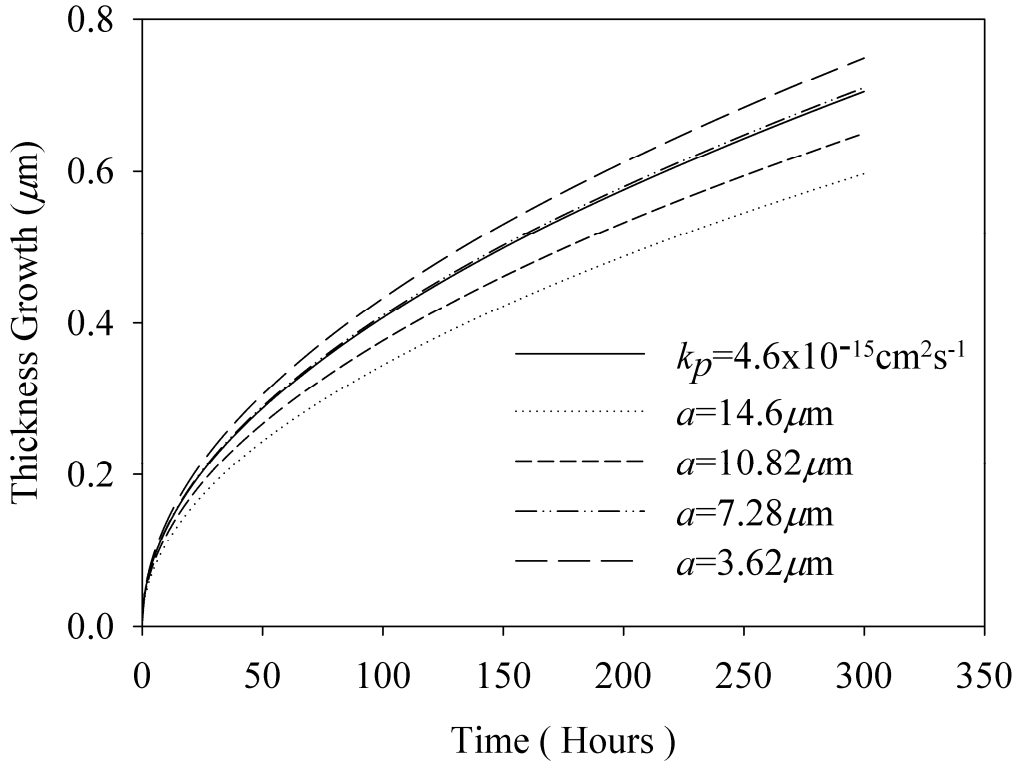

Figure 5.15 Oxidation kinetics of Fe-Cr-Y versus average sizes of oxide grains

Table 5.1 Material properties for alloy

16% (wt) Fe-Cr alloy properties	Symbol	Value
Particle surface inclined angle	β	$\pi/4$
Particle edge length	d	2.5 nm
Burgers vector	b	0.25 nm
Kinetic constant	C_i	0.9788 $m^2 J^1 s^{-1}$
Dimensionless factor	H_{gb}	2.91
Grain boundary thickness	δ	1.5nm
Taylor factor	M	0.4
Pilling and Bedworth ratio	PBR	2.07

After validating our results, we get back to the kinetics of Fe-Cr-Y alloy. In the following study, we assume that the yttrium has only blocked the diffusion of chromium ion while the dopant does not change or rarely changes the diffusivity of oxygen ions. This assumption has also been confirmed by Pieraggi and Rapp [120]. Observations after different oxidation times have shown that the oxide scale thickness of the flat-interface portion remains flat during the oxidation process.

Figure 5.16 shows the predicted results of thickness change at the flat-interface portion of the oxide scale. It is clearly indicated that the overall scale growth on the doped alloy is from the contribution of downward growth dominated by oxygen ion diffusion.

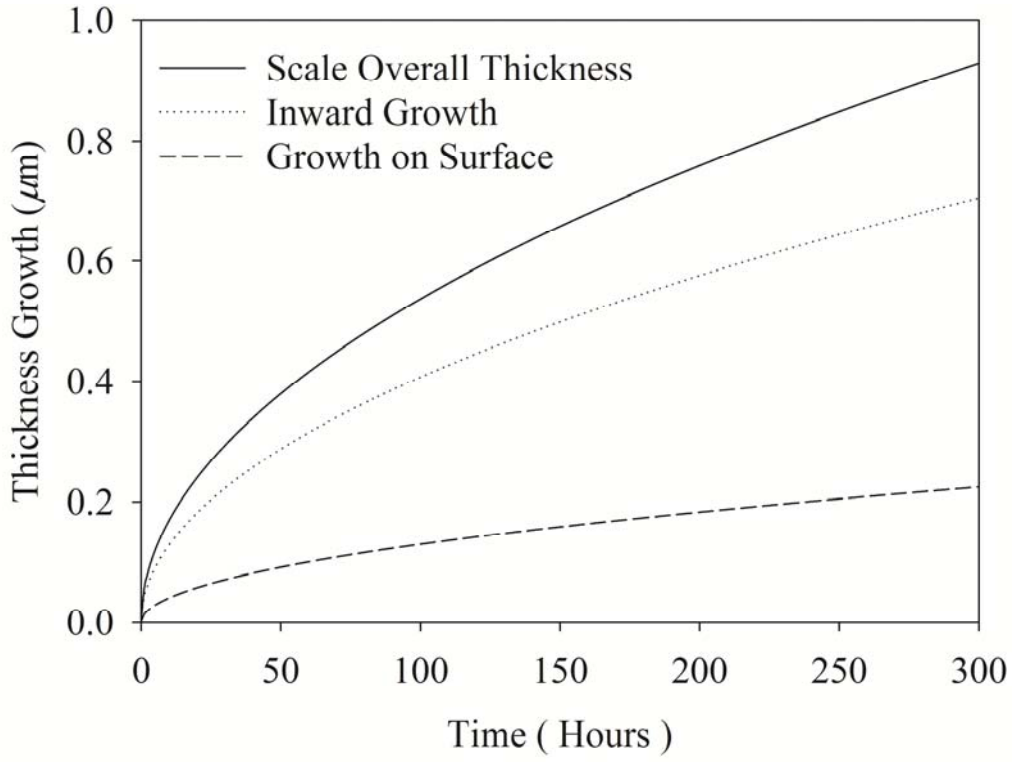

Figure 5.16 Change of oxide scale thickness

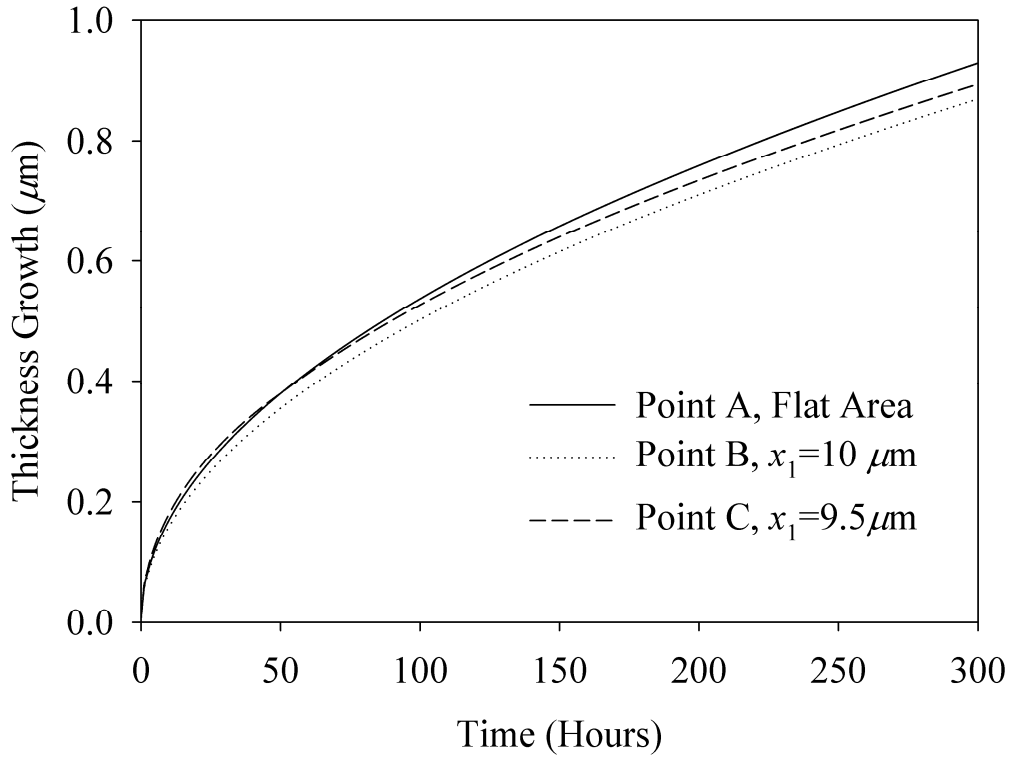

Figure 5.17 Oxidation Kinetics of the Peg

However, at the peg portion of the interface (or the curved portion), not only is the thickness of the scale different, but the growth trend of the scale varies as well. Figure 5.17 gives the oxidation kinetics at different locations (x_1=9 μm, x_1=9.4 μm, x_1=10 μm) around the peg portion of the interface. The results show that the thickness at a position corresponding to the valley of the curved interface grows slower than all other positions. An interesting trend of scale growth can be found at the slope area of the valley (x_1=9.4 μm). The oxide scale at x_1=9.4 μm first experiences a fast growth trend. The trend then gradually reduces to a relatively slow one as that is at the valley bottom. To obtain more information about the phenomenon, we also plotted the

inward-growth velocity distribution along the scale-alloy interface around the peg area. This can be found in Figure 5.18. We found that the inward-growth velocity reached its current minimum value at the bottom of the valley at each given time. The maximum velocities, using the one at t=50 hours as an example, occur at the sloped area of the valley and can be located relatively close to the flat portion of the interface. As the location becomes far from the valley, the inward-growth velocities decrease to a constant level. Besides, due to the growth of thickness, the inward-growth velocity at different times keeps decreasing. From expansion of the distance between the two local maximum velocities, we can easily identify the transversely growing trend of the peg.

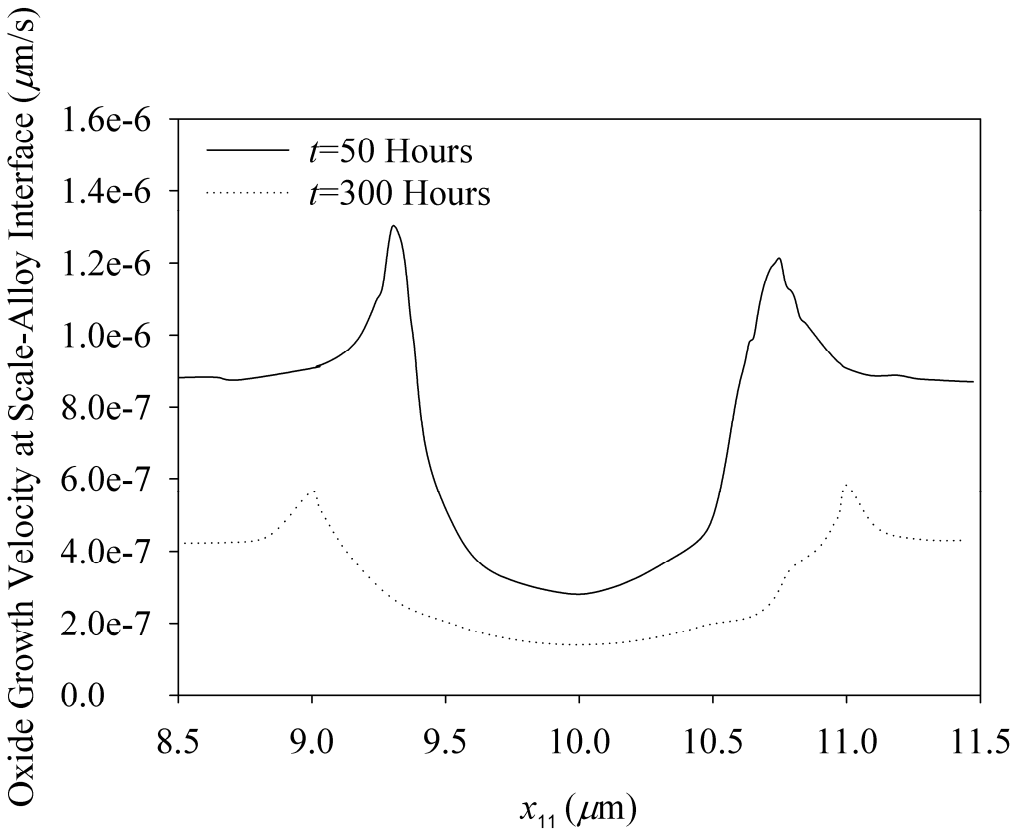

Figure 5.18 Inward-growth velocity distribution along scale-alloy interface at different times

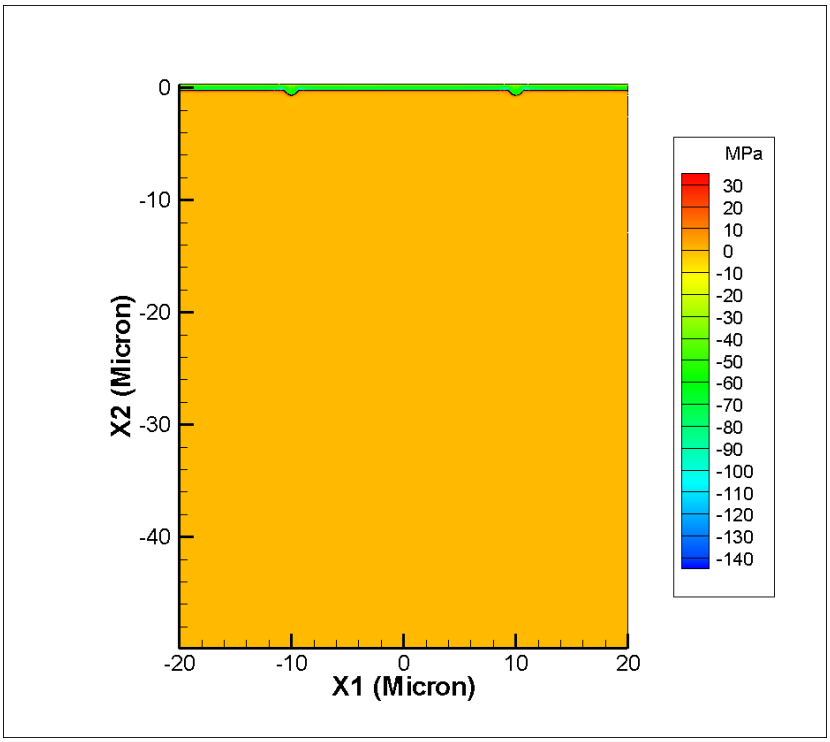

(a)

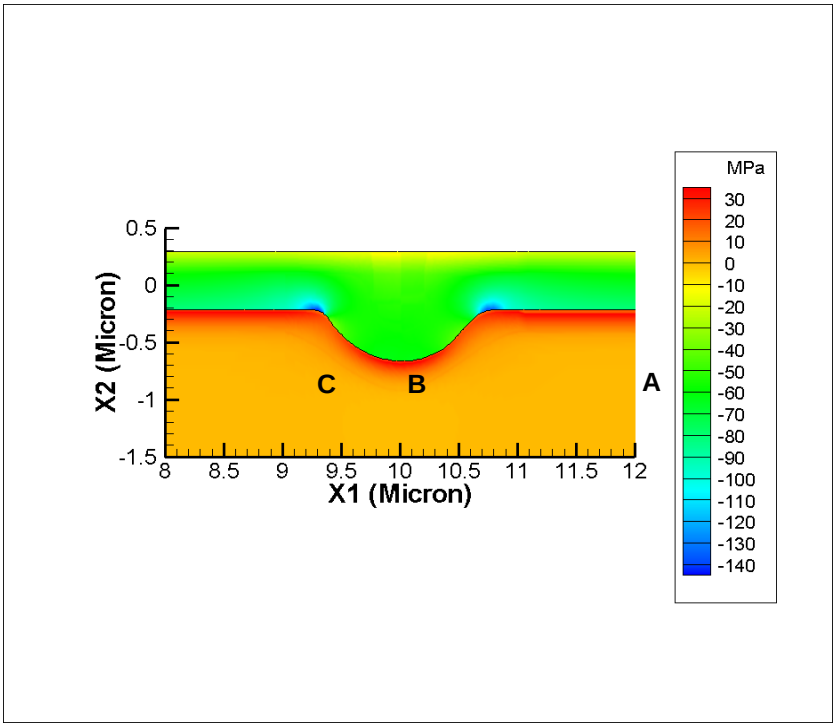

(b)

Figure 5.19 (a) Contour of in-plane stress σ_{11} in oxide and alloy after 50 hours of oxidation. (b) Contour of in-plane stress σ_{11} around peg.

From the inward-growth governing equation (5.75), we know that both the inward-growth velocity and the oxidation kinetics are controlled by the gradient of the stress-dependent chemical potential. Therefore, the scale growth trend and the distribution of inward-growth velocities should be explained based on this equation. Since the scale thickness at the valley is relatively larger than that beyond the flat interface, the gradient for oxygen ion concentration is low at that area. While for the gradient of stress dependent part, from the stress distribution in Figure 5.19 (b) we found that at t=50 hours the highest stress gradient occur around the locations where we observed the fastest inward-growth velocity. The observations from Figure 5.17, Figure 5.18 and Figure 5.19 (b) indicate the stress dependent effect. The highest interfacial stress gradient assists the inward oxygen flux at the scale-alloy interface. As a direct consequence, the inward-growth of the scale reaches the highest velocity, which is represented in Figure 5.17 by the dashed-line before 50 hours. The next step after the fast local scale growth will be the width expansion of the pegs. Consequentially, the highest stress gradients move far from the bottom of the valley, which leave the previously fast growth area to a relatively slow growth area. This growth rate change is accounted for by: first, the decrease of the oxygen ions concentration gradient due to thicker local scale; two, the decrease of stress gradient due to movement of highest compressive stresses at the scale-alloy interface.

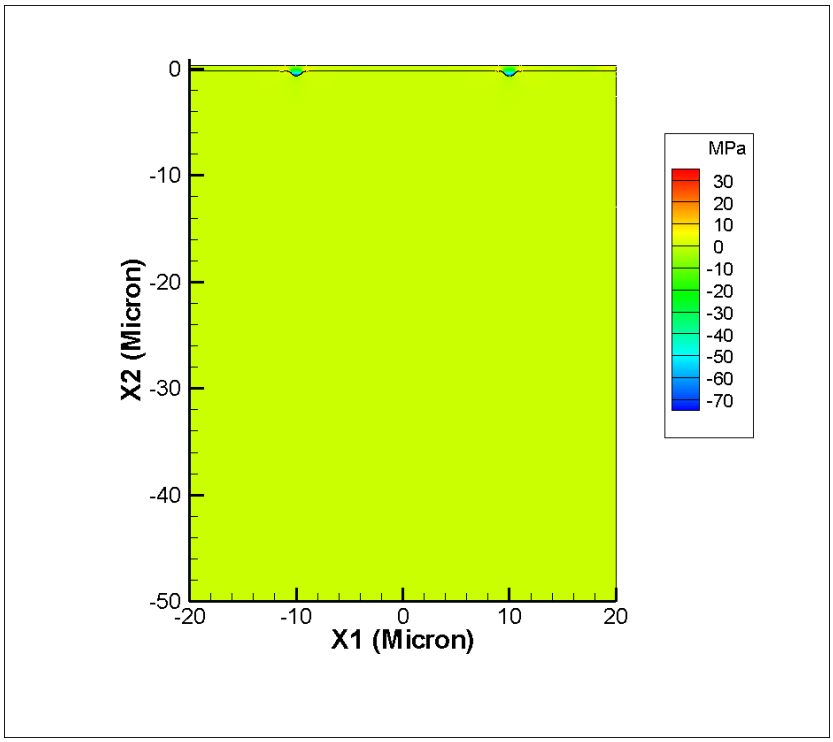

(a)

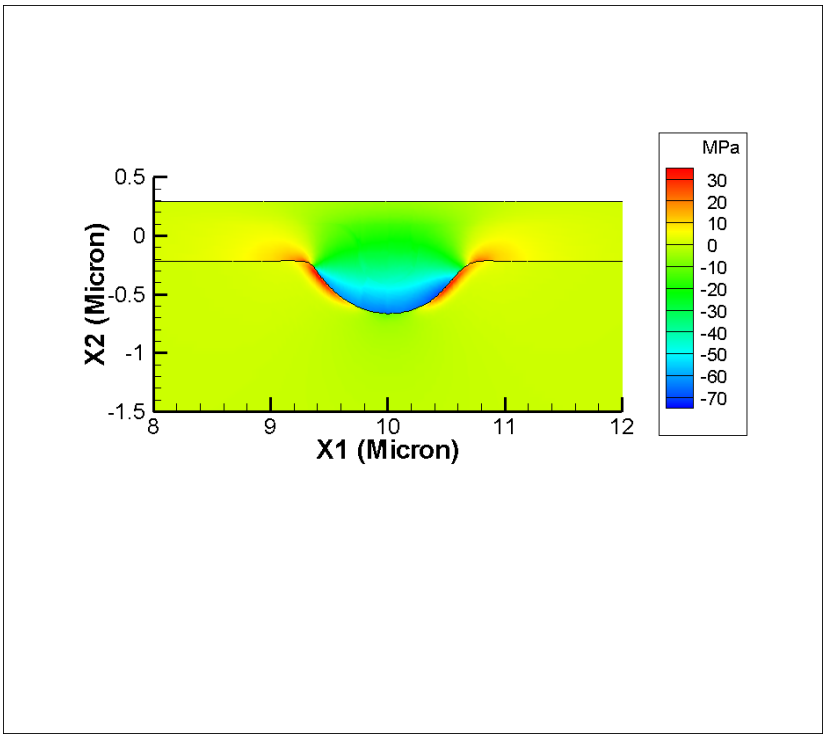

(b)

Figure 5.20 (a) Contour of in-plane stress σ_{22} in oxide and alloy after 50 hours of oxidation. (b) Contour of in-plane stress σ_{22} around peg.

The results in Figure 5.20, which is obtained at t=50 hours, indicate that the highest interfacial tensile stress occurs at the peg areas. Here, the results for stress distribution in Figure 5.19 and Figure 5.20 are obtained with the mean planar spacing 2λ set to be 1 μm. Due to yielding and creep of the alloy, the highest level of tensile is around 30 MPa. To demonstrate the dopant dispersion effect on creep, i.e. the threshold stress effect, we also plot the evolution of the magnitude of the highest tensile stress, which is given in Figure 5.21. As can be seen, the highest tensile stress increases with the decrease of 2λ. The magnitude change of the tensile stress can mostly be accounted for by the increase of the threshold stress for creep due to the smaller mean planar spacing.

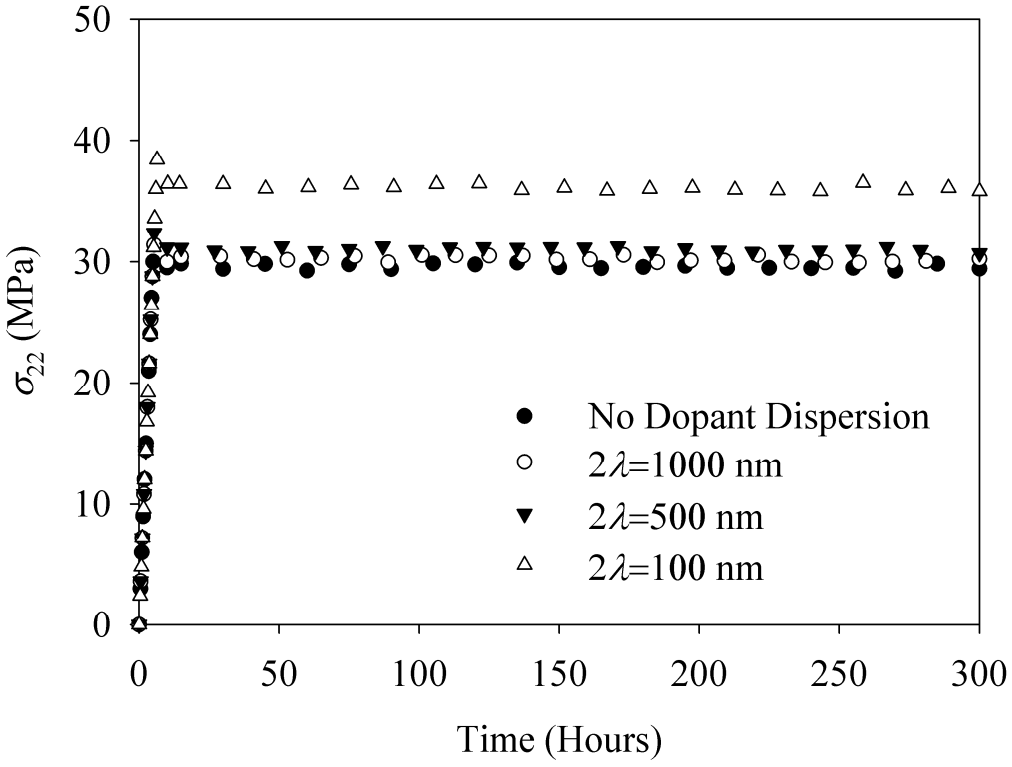

Figure 5.21 Evolution of the highest normal tensile stress versus different planar spacing of the Y_2O_3 dispersion

5.8 Summary

In this chapter, a continuum thermodynamics model is developed to include alloy inelastic behavior into stress-diffusion interaction during oxidation of Fe-Cr alloys. The chemical potential is related with not only the concentration of species and elastic deformation, but also inelastic deformation. This gives a fully coupled relation between the chemical reaction and mechanical stress, namely not only oxidation induces stress, but in return stress also affects the rate of oxidation by

changing the elastic-plastic deformation.

As an example, this model has been implemented in two-dimension using finite element method to study the growth mechanism of an interfacial crack along oxide-alloy interface after steady state has been reached. The presented results provide clear insight into how the plastic deformation of an alloy affects the stresses distribution around the crack tip and the crack growth driving force. It is also found that the reactive element effect reduces ionic diffusion and the resultant slow oxidation kinetics helps to arrest the interfacial crack.

The implementation of the modified stress-diffusion interaction model was emphasized on the reactive element effect (REE). The results were presented in light of the REE on scale growth kinetics and mechanical response of the scale-alloy system. It was found that both stresses and the variation of oxide grain size can significantly affect the oxidation kinetics by changing the dominating oxygen flux. The creep and yielding of alloy drastically reduce the highest normal tensile stress at the scale-alloy interface. The existence of reactive oxide dispersion in the alloy slightly increases the magnitude of the highest normal tensile stress.

Finally, it should be pointed out that, although it is developed based on a Fe-Cr alloy, the present model can be easily extended to many different types of binary alloys.

CHAPTER 6 SUMMARY AND RECOMMENDATIONS FOR FUTURE WORKS

6.1 Overview and findings

6.1.1 Overview

In this study, the issue of interaction between stress and transport of ionic species during high-temperature oxidation process was addressed. The materials Fe-16wt % Cr and Fe-16wt % Cr-Y alloys were used in this study for their prospective roles as the interconnect materials in solid oxide fuel cells. Efforts were taken for possible improvements on the service time of the alloy interconnect in a solid oxide fuel cell environment. Two interesting features make this goal more realistic: stress dependent oxidation kinetics and reactive element modification of the cation diffusivity in oxide scale.

Following the background review, the majority of this dissertation starts with the establishment of the diffusion-stress interaction oxidation model in chapter 3. After demonstrating the stress-dependent effect on oxidation kinetics and the oxidation-induced interfacial failure mechanism, the modification effect of the reactive element (Yttrium oxide) on cation diffusivity (Chromium ion) was modeled in chapter 4. The remainder of this dissertation then extends the interactive model to include the inelastic deformation of the alloys (chpter 5). Care has been given to the

reactive element effect on materials with interfacial crack and the comprehensive oxidation process of alloy with reactive element dopants. Here we list the major findings from this study.

1) Stresses and ionic diffusion have strong interaction during the oxidation process. This interaction eventually applies an impact on the oxidation kinetics.
2) Metal are severely depleted along the alloy grain boundaries, especially at the scale-alloy interface. The metal depletion provides significant possibility for interfacial void generation, or we may say that the depletion initialize the interfacial void/imperfection. High magnitude interfacial normal tensile stresses are also introduced around the depleted alloy grain boundary areas. These tensile stresses may assist the interfacial imperfections to grow along the scale-alloy interface.
3) The reactive element effect is essentially realized by blocking the cation diffusion along the grain boundaries of the oxide. The interfacial normal tensile stresses in RE doped alloy, as one of the consequence, are drastically reduced to roughly 50-60% of those generated in undoped alloys.
4) The effect of reactive dopants also affects the strain energy release rates of the pre-existing scale-alloy interfacial crack. This reinforces the need for reactive elements during the design of metallic alloys for high temperature applications.

6.2 Chapter summaries

6.2.1 Chapter 3 Stress-Oxidation Interaction in Selective Oxidation of Fe-Cr Alloys with elastic deformation

In this chapter, a continuum thermodynamic model is developed to account for stress-diffusion interaction in the oxidation of Fe-Cr alloys. In comparison with other existing models, the present approach is formulated in the Eulerian framework. In this fully coupled theory, not only the hydrostatic stress, but also the deviatoric stress needs to be considered. The model provides detailed distribution of stresses in the scale layer, as well as concentration distributions of all diffusing species in the system. The model results provide clear insight into oxidation mechanisms and how the stress affects the diffusion and oxidation process. The results also demonstrate the spallation initiating mechanisms and how the ionic diffusion affects the stress distributions.

6.2.2 Chapter 4 The Reactive Element Effect on Diffusivity Modification

In this chapter, a quantitative relation between the diffusivities of chromium ions and the activities of a reactive element (yttrium) have been derived and have been incorporated with a continuum thermodynamic model accounting for stress-diffusion interaction in the oxidation of Fe-Cr alloys. A 2D finite element model has been presented to analyze the effects of reactive elements on the oxidation. The presented results confirm the experimental outcomes by predicting that the thickness of the oxide scale of Fe-Cr-Y is much less than that of Fe-Cr at the identical

oxidizing circumstances. It is also shown that normal tensile stresses with lower magnitude are generated at the oxide-alloy interface when the alloys are doped with reactive elements, which is believed to be among the important origins of reducing the driving force for oxide spallation.

6.2.3 Chapter 5 The comprehensive study of the reactive element effect

In this chapter, the diffusion-stress interaction model is developed to include alloy inelastic behavior into stress-diffusion interaction during oxidation of Fe-Cr alloys. The chemical potential is related with not only the concentration of species and elastic deformation, but also inelastic deformation. This model has been first implemented in two dimensions using the finite element method to study the reactive element effect on the propagation driving force of an interfacial crack along oxide-alloy interface after steady state has been reached. It is found that the reactive element effect on reducing ionic diffusion and the resultant slow oxidation kinetics help to rest the interfacial crack. The modified stress-diffusion interaction model is then implemented to a more comprehensive study on the reactive element effect, including peg forming, scale grain size and the creep dispersion effects. The results were presented in light of the REE on scale growth kinetics and mechanical response of the scale-alloy system. It was found that both stresses and the variation of oxide grain size can significantly affect the oxidation kinetics by changing the dominating oxygen flux. The creep and yielding of the alloy drastically reduce the highest normal tensile stress at the scale-alloy interface. The existence of reactive oxide dispersion in

alloy slightly increases the magnitude of the highest normal tensile stress.

6.3 Contributions

The major contributions of this study are:

1) Development of the diffusion-stress interaction model for oxide growth on metallic alloy.
2) Development of diffusivity of metal cation in oxide grain boundaries for quantitative estimation of the reactive element effect on ionic diffusion.
3) Estimation of the stress-diffusion interaction effect on oxidation kinetics of binary metallic alloys.
4) Identification of the mechanism of interfacial spallation/failure of an oxide scale grown on a binary alloy.
5) Estimation of the reactive element effect on improvement of mechanical performance of scale-alloy systems, including the decrease of interfacial normal tensile stresses, interfacial energy release rate.

Although the study is focusing on Fe-16wt. % Cr alloy, the methodologies developed can be used to estimate the oxidation kinetics and mechanical performance during the selective oxidation of any other binary alloy

6.4 Future work

In this study, the concentrations of cations and anion in the oxide scale are assumed to be dilute. So we may express the stress-independent chemical potential in

the Boltzmann type. However, it is highly possible that the concentration of the ions in the oxide could be so much higher that it exceeds the range of dilute solution. Under such circumstances, the expression of the Boltzmann type for chemical potential is inappropriate. The Fermi-Dirac type expression is required for the expression of chemical potential. It is necessary to study how this different definition affects the stress-diffusion interaction.

The reactive element effect on the ionic diffusivity was estimated in this study by the electrochemistry methodology. The diffusivity in the oxide grain boundary may also be analyzed by the molecular dynamics method. In accordance with classical diffusion theory, the diffusivity is computed by the mean-square displacement (MSD) of atoms which by definition is given as

$$\text{MSD}=\sum_i \left\langle \left| r(t) - r(0) \right|^2 \right\rangle$$

where $\langle . \rangle$ denotes the averaging over all atoms, $r_i(t)$ is the position of atom i at time t and $r_i(0)$ is the initial position. The diffusivity can be given as the slope of the MSD curve vs time, which is

$$D = \frac{\text{MSD}}{6Nt}$$

where N is the total number of atoms in the ensemble. The above procedure will be repeated for several values of applied stress.

A most used assumption in this study is that the material properties are

independent of the stress and ion concentrations. However, it has been found that the material properties, such as the elastic constants are dependent on quantities such as defect concentration. Once again, we can use MD methodology to evaluate the dependences of the material properties on stress or concentrations. With the field dependent material properties explicitly evaluate, it would improve the accuracy of the prediction from the diffusion-stress interaction model.

This dissertation is entirely focusing on theoretical derivations and numerical implementations based on necessary experimental results. In order to verify the oxidation kinetics, the level of stress generated, and the stress dependent effect on ionic transport, it would be interesting to have some further work on experimental validation. Experimental techniques such as thermo-gravity analysis (TGA), X-ray diffraction and tracer measurement are necessary to accomplish these studies.

This study is a new attempt in theoretical description of oxide scale growth. Other possible extensions of this work involve considering multiple dopants in addition to the single dopant that has been considered in this work, either experimental works or the MD simulations will be good extensions. The reaction rate constants (which could be considered as a function) stand for the possibility that the cations and anions meet in the oxide scale to form a compound and hence is a concentration dependent quantity. Modeling the concentration dependent reaction rate constant involves ab initio simulation and will be an interesting topic. Furthermore, integrating this reaction rate function into the established model will give us more accurate results in predicting the oxide growth and hence is a meaningful extension.

REFERENCES

1. Krishnamurthy, R. and D.J. Srolovitz, *Stress distributions in growing oxide films.* Acta Materialia, 2003. **51**(8): p. 2171-90.

2. Limarga, A.M., D.S. Wilkinson, and G.C. Weatherly, *Modeling of oxidation-induced growth stresses.* Scripta Materialia, 2004. **50**(12): p. 1475-1479.

3. Bull, S.J., *Modeling of residual stress in oxide scales.* Oxidation of Metals, 1998. **49**(1-2): p. 1-17.

4. Young, E.W.A., J.H. Gerretsen, and J.H.W. de Wit, *The oxygen partial pressure dependence of the defect structure of chromium(iii)oxide.* Journal of the Electrochemical Society, 1987. **134**(9): p. 2257-60.

5. Atkinson, A. and R.I. Taylor, *Diffusion of ^{57}co along grain boundaries in nio.* Philosophical Magazine A: Physics of Condensed Matter, Defects and Mechanical Properties, 1982. **45**(4): p. 583-592.

6. Atkinson, A., *Transport processes during the growth of oxide films at elevated temperature.* Reviews of Modern Physics, 1985. **57**(2): p. 437-70.

7. Tsai, S.C., A.M. Huntz, and C. Dolin, *Growth mechanism of cr_2o_3 scales: Oxygen and chromium diffusion, oxidation kinetics and effect of yttrium.* Materials Science & Engineering A: Structural Materials: Properties, Microstructure and Processing, 1996. **A212**(1): p. 6-13.

8. Rhines, F.N. and J.S. Wolf, *Role of oxide microstructure and growth stresses in the high- temperature scaling of nickel.* Metallurgical and Materials Transactions B, 1970. **1**(6): p. 1701-10.

9. Kofstad, P., *Diffusion and electrical conductivity in binary metal oxide.* 1972, New York: Wiley.

10. Bernard, O., et al., *Mechanical and microstructural characterisation of oxide films damage.* Materials Science & Engineering A (Structural Materials:

Properties, Microstructure and Processing), 2002. **A335**(1-2): p. 32-42.

11. Calvarin, G., et al., *Oxide scale stress determination by raman spectroscopy application to the nicr/cr2o3 system and influence of yttrium.* Scripta Materialia, 1998. **38**(11): p. 1649-1658.

12. Huntz, A.M., *Stresses in nio, cr_2o_3 and al_2o_3 oxide scales.* Materials Science & Engineering A: Structural Materials: Properties, Microstructure and Processing, 1995. **A201**(1-2): p. 211-228.

13. Mougin, J., et al., *In-situ determination of growth and thermal stresses in chromia scales formed on a ferritic stainless steel.* Materials and Corrosion-Werkstoffe Und Korrosion, 2002. **53**(7): p. 486-490.

14. Mougin, J., et al., *In situ raman monitoring of chromium oxide scale growth for stress determination.* Journal of Raman Spectroscopy, 2001. **32**(9): p. 739-744.

15. Tolpygo, V.K. and D.R. Clarke, *Competition between stress generation and relaxation during oxidation of an fe-cr-al-y alloy.* Oxidation of Metals, 1998. **49**(1-2): p. 187-212.

16. Stringer, J., *Stress generation and relief in growing oxide films.* Corrosion Science, 1970. **10**(7): p. 513-43.

17. Pieraggi, B. and R.A. Rapp, *Stress generation and vacancy annihilation during scale growth limited by cation-vacancy diffusion.* Acta Metallurgica, 1988. **36**(5): p. 1281-1289.

18. Kofstad, P. *Fundamental aspects of corrosion by hot gases*. 1989. Les Embiez, France.

19. Huntz, A.M. *Scale growth and stress development*. 1988. London, UK.

20. Barnes, J.J., J.G. Goedjen, and D.A. Shores, *A model for stress generation and relief in oxide metal systems during a temperature-change.* Oxidation of Metals, 1989. **32**(5-6): p. 449-469.

21. Goedjen, J.G., et al., *Evaluation of stresses in ni-nio and cr-cr2o3 during high-temperature oxidation by in-situ x-ray-diffraction.* Materials Science and Engineering a-Structural Materials Properties Microstructure and Processing, 1994. **177**(1-2): p. 115-124.

22. Birnie, J., et al., *Ex situ and in situ determination of stress distributions in chromium oxide films by raman microscopy.* Corrosion Science, 1992. **33**(1): p. 1-12.

23. Lobnig, R.E., et al., *Diffusion of cations in chromia layers grown on iron-base alloys.* Oxidation of Metals, 1992. **37**(1-2): p. 81-93.

24. Huntz, A.M. and S.C. Tsai, *Diffusion in oxide scales - application to cr2o3 scales.* Journal of Materials Science Letters, 1994. **13**(11): p. 821-825.

25. Sabioni, A.C.S., et al., *Relation between the oxidation growth-rate of chromia scales and self-diffusion in cr2o3.* Journal of Materials Science, 1992. **27**(17): p. 4782-4790.

26. Howes, V.R., *Observations of the metal-oxide interface for a fe-cr alloy.* Corrosion Science, 1968. **8**(4): p. 221-224.

27. Howes, V.R., *The early growth of oxide on a fe-cr alloy.* Corrosion Science, 1967. **7**(11): p. 735-746.

28. Appleby, W.K. and R.F. Tylecote, *Stresses during the gaseous oxidation of metals.* 1970. **10**(5): p. 325-41.

29. Suo, Z., et al., *Stresses induced in alloys by selective oxidation.* Acta Materialia, 2003. **51**(4): p. 959-74.

30. Yearian, H.J., E.C. Randell, and T.A. Longo, *Structure of oxide scales on chromium steels.* Corrosion, 1956. **12**(10): p. 55-65.

31. Nijdam, T.J., L.P.H. Jeurgens, and W.G. Sloof, *Modelling the thermal oxidation of ternary alloys - compositional changes in the alloy and the development of oxide phases.* Acta Materialia, 2003. **51**(18): p. 5295-5307.

32. Li, J.C.M., R.A. Oriani, and L.S. Darken, *Thermodynamics of stressed solids.* Zeitschrift Fur Physikalische Chemie-Frankfurt, 1966. **49**(3-5): p. 271-&.

33. Larche, F. and J.W. Cahn, *Linear theory of thermochemical equilibrium of solids under stress.* Acta Metallurgica, 1973. **21**(8): p. 1051-1063.

34. Venkatraman, R., et al., *Mechanical-properties and microstructural characterization of al-0.5-percent cu thin-films.* Journal of Electronic Materials, 1990. **19**(11): p. 1231-1237.

35. Venkatraman, R., S. Chen, and J.C. Bravman, *The effect of laser reflow on the variation of stress with thermal cycling in aluminum thin-films.* Journal of Vacuum Science & Technology a-Vacuum Surfaces and Films, 1991. **9**(4): p. 2536-2542.

36. Swaminathan, N., J. Qu, and Y. Sun, *An electrochemomechanical theory of defects in ionic solids. I. Theory.* Philos. Mag., 2007. **87**(11): p. 1705-1721.

37. Krishnamurthy, R. and D.J. Srolovitz, *Stress distributions in growing polycrystalline oxide films.* Acta Materialia, 2004. **52**(13): p. 3761-80.

38. Fisher, J.C., *Calculation of diffusion penetration curves for surface and grain boundary diffusion.* Journal of Applied Physics, 1951. **22**(1): p. 74-77.

39. Whipple, R.T.P., *Concentration contours in grain boundary diffusion.* Philosophical Magazine, 1954. **45**(371): p. 1225-1236.

40. Chung, Y.C. and B.J. Wuensch, *An improved method, based on whipple's exact solution, for obtaining accurate grain-boundary diffusion coefficients from shallow solute concentration gradients.* Journal of Applied Physics, 1996. **79**(11): p. 8323-8329.

41. Gilmer, G.H. and H.H. Farrell, *Grain-boundary diffusion in thin-films .1. Isolated grain-boundary.* Journal of Applied Physics, 1976. **47**(9): p. 3792-3798.

42. Gilmer, G.H. and H.H. Farrell, *Grain-boundary diffusion in thin-films .2. Multiple grain-boundaries and surface-diffusion.* Journal of Applied Physics, 1976. **47**(10): p. 4373-4380.

43. Preis, W. and W. Sitte, *Fast grain boundary diffusion and rate-limiting surface exchange reactions in polycrystalline materials.* Journal of Applied Physics, 2005. **97**(9).

44. Harding, J.H., *Short-circuit diffusion in ceramics.* Interface Science, 2003. **11**(1): p. 81-90.

45. Harding, J.H., K.J.W. Atkinson, and R.W. Grimes. *Experiment and theory of diffusion in alumina*. 2003. Schloss Ringberg, Germany: American Ceramic Soc.

46. Chen, J., et al., *Ab initio theoretical tensile test on y-doped σ=3 grain boundary in α-al₂o₃.* Acta Materialia, 2005. **53**(2): p. 403-10.

47. Suzuki, A. and Y. Mishin, *Atomic mechanisms of grain boundary motion.* New Frontiers of Processing and Engineering in Advanced Materials, 2005. **502**: p. 157-162.

48. Gutierrez, G. and B. Johansson, *Molecular dynamics study of structural properties of amorphous al_2o_3.* Physical Review B (Condensed Matter and Materials Physics), 2002. **65**(10): p. 104202-1.

49. Daw, M.S. and M.I. Baskes, *Embedded-atom method - derivation and application to impurities, surfaces, and other defects in metals.* Physical Review B, 1984. **29**(12): p. 6443-6453.

50. Mishin, Y., et al., *Interatomic potentials for monoatomic metals from experimental data and ab initio calculations.* Physical Review B, 1999. **59**(5): p. 3393-3407.

51. Mishin, Y., et al., *Structural stability and lattice defects in copper: Ab initio, tight-binding, and embedded-atom calculations.* Physical Review B, 2001. **63**(22).

52. Mishin, Y., *Atomistic modeling of the gamma and gamma '-phases of the ni-al system.* Acta Materialia, 2004. **52**(6): p. 1451-1467.

53. Karakasidis, T. and M. Meyer, *Grain-boundary diffusion of cation vacancies*

in nickel oxide: A molecular-dynamics study. Physical Review B: Condensed Matter, 1997. **55**(20): p. 13-853.

54. Plimpton, S.J. and E.D. Wolf, *Effect of interatomic potential on simulated grain-boundary and bulk diffusion: A molecular-dynamics study.* Physical Review B (Condensed Matter), 1990. **41**(5): p. 2712-21.

55. Clarke, D.R., *The lateral growth strain accompanying the formation of a thermally grown oxide.* Acta Materialia, 2003. **51**(5): p. 1393-407.

56. Huin, D., P. Flauder, and J.B. Leblond, *Numerical simulation of internal oxidation of steels during annealing treatments.* Oxidation of Metals, 2005. **64**(1-2): p. 131-167.

57. Favergeon, J., T. Montesin, and G. Bertrand, *Mechano-chemical aspects of high temperature oxidation: A mesoscopic model applied to zirconium alloys.* Oxidation of Metals, 2005. **64**(3-4): p. 253-79.

58. Li, Y.L. and J.E. Morral, *A local equilibrium model for internal oxidation.* Acta Materialia, 2002. **50**(14): p. 3683-3691.

59. Stephenson, G.B., *Deformation during interdiffusion.* Acta Metallurgica, 1988. **36**(10): p. 2663-2683.

60. Evans, A.G. and R.M. Cannon. *Stresses in oxide films and relationships with cracking and spalling*. in *Norman L. Peterson Memorial Symposium - Oxidation of Metals and Associated Mass Transport, Proceedings.* 1987. Orlando, FL, USA: Metallurgical Soc of AIME.

61. Li, J.C.M., F.V. Nolfi, and C.A. Johnson, *Diffusional equilibrium of substitutional atoms in a stressed solid.* Acta Metallurgica, 1971. **19**(8): p. 749-&.

62. Larche, F.C. and J.W. Cahn, *The interactions of composition and stress in crystalline solids.* Acta Metallurgica, 1985. **33**(3): p. 331-57.

63. Guggenheim, E.A., *Thermodynamics*. 1949, New York: Interscience Publisher, Inc.

64. Wu, C.H., *The role of eshelby stress in composition-generated and stress-assisted diffusion.* J. Mech. Phys. Solids, 2001. **49**(8): p. 1771-1794.

65. Fergus, J.W., *Metallic interconnects for solid oxide fuel cells.* Materials Science & Engineering A (Structural Materials: Properties, Microstructure and Processing), 2005. **397**(1-2): p. 271-83.

66. Wood, G.C., *Oxidation of iron-chromium alloys and stainless steels at high temperatures.* Corrosion Science, 1962. **2**: p. 173-196.

67. Wood, G.C., T. Hodgkiess, and D.P. Whittle, *Comparison of scaling behaviour of pure iron-chromium and nickel-chromium alloys in oxygen.* Corrosion Science, 1966. **6**(3-4): p. 129-147.

68. Seybolt, A.U., *Observations on fe-cr-o system.* Electrochemical Society -- Journal, 1960. **107**(3): p. 147-156.

69. Lai, D., et al., *Oxidation of iron-chromium alloys at 750-1025 c.* Corrosion, 1961. **17**(7): p. 109-116.

70. Footner, P.K., D.R. Holmes, and D. Mortimer, *Oxidation of iron-chromium binary alloys.* Nature, 1967. **216**: p. 54-56.

71. Wood, G.C. and D.A. Melford, *Examination of oxide scales on iron-chromium alloys by x-ray scanning microanalysis.* Iron and Steel Institute -- Journal, 1961. **198**(Part 2): p. 142-148.

72. Yu, X. and Y. Sun, *The oxidation improvement of fe_3al based alloy with cerium addition at temperature above 1000 ^{o}c.* Materials Science and Engineering A, 2003. **363**(1-2): p. 30-39.

73. Bautista, A., F. Velasco, and J. Abenojar, *Oxidation resistance of sintered stainless steels: Effect of yttria additions.* Corrosion Science, 2003. **45**(6): p. 1343-54.

74. Qu, W., J. Li, and D.G. Ivey, *Sol-gel coatings to reduce oxide growth in interconnects used for solid oxide fuel cells.* Journal of Power Sources, 2004. **138**(1-2): p. 162-173.

75. Wolff, I.M., et al., *Oxidation and corrosion behaviour of fe-cr and fe-cr-al alloys with minor alloying additions.* Materials Science & Engineering A (Structural Materials: Properties, Microstructure and Processing), 1998. **A241**(1-2): p. 264-76.

76. Chevalier, S., et al., *The reactive element effect on thermally grown chromia scale residual stress.* Materials Science & Engineering A: Structural Materials: Properties, Microstructure and Processing, 2003. **A343**(1-2): p. 257-64.

77. Martinez-Villafane, A., et al., *Oxidation performance of a fe-13cr alloy with additions of rare earth elements.* Materials Science & Engineering A (Structural Materials: Properties, Microstructure and Processing), 2003. **A363**(1-2): p. 15-19.

78. Meier, G.H. and F.S. Pettit, *Fundamental studies of the durability of materials for interconnects in solid oxide fuel cells (sofcs).* FY 2004 Annual Report, 2004.

79. Perez, F.J., et al., *Effect of yttrium and erbium ion implantation on the oxidation behaviour of the aisi 304 austenitic steel.* Surface and Coatings Technology, 2000. **126**(2-3): p. 116-122.

80. Polman, E.A., T. Fransen, and P.J. Gellings, *The reactive element effect - ionic processes of grain-boundary segregation and diffusion in chromium-oxide scales.* Journal of Physics-Condensed Matter, 1989. **1**(28): p. 4497-4510.

81. Liu, Z.Y., W. Gao, and Y.D. He, *Modeling of oxidation kinetics of y-doped fe-cr-al alloys.* Oxidation of Metals, 2000. **53**(3-4): p. 341-350.

82. Williams, M.L., *The stresses around a fault or crack in dissimilar media.* Bull Seismol Soc. Am., 1959. **49**(2): p. 199-204.

83. Dundurs, J., *Edge-bonded dissimilar orthogonal elastic wedges under normal and shear loading.* Journal of Applied Mechanics, 1969. **36**: p. 650-652.

84. Erdogan, F., *Stress distribution in bonded dissimilar materials with cracks.* Journal of Applied Mechanics, 1965. **32**(2): p. 403-410.

85. Rice, J.R. and G.C. Sih, *Plane problems of cracks in dissimilar media.* Journal

of Applied Mechanics, 1965. **32**(2): p. 418-423.

86. Comninou, M., *An overview of interface cracks.* Engineering Fracture Mechanics, 1990. **37**(1): p. 197-208.

87. Hutchinson, J.W., M.E. Mear, and J.R. Rice, *Crack paralleling an interface between dissimilar materials.* Journal of Applied Mechanics-Transactions of the Asme, 1987. **54**(4): p. 828-832.

88. Rice, J.R., *Elastic fracture mechanics concepts for interfacial cracks.* Journal of Applied Mechanics-Transactions of the ASME 1988. **55**(1): p. 98-03.

89. Shih, C.F. and R.J. Asaro, *Elastic-plastic analysis of cracks on bimaterial interfaces .1. Small-scale yielding.* Journal of Applied Mechanics-Transactions of the Asme, 1988. **55**(2): p. 299-316.

90. Zywicz, E. and D.M. Parks, *Elastic yield zone around an interfacial crack tip.* Journal of Applied Mechanics-Transactions of the Asme, 1989. **56**(3): p. 577-584.

91. Griffith, A.A., *Phenomena of rupture and flow in solids.* Philosophical Transactions of the Royal Society of London, Series A, 1968. **221**: p. 163-198.

92. Rice, J.R., *Elastic-plastic mechanics of crack extension.* International Journal of Fracture, 1968. **4**(1): p. 41-47.

93. Rice, J.R., *Path independent integral and approximate analysis of strain concentration by notches and cracks.* Journal of Applied Mechanics, 1968. **35**: p. 379-386.

94. Krueger, R., *The virtual crack closure technique: History, approach and applications*. 2002, NASA: Hampton,VA.

95. El Kadiri, H., M.F. Horstemeyer, and D.J. Bammann, *A theory for stress-driven interfacial damage upon cationic-selective oxidation of alloys.* J. Mech. Phys. Solids, 2008. **56**(12): p. 3392-3415.

96. Matsuda, N., et al. *The effect of atmosphere on the creep deformation of a*

particle reinforced aluminum alloy matrix composites. 2004.

97. Lee, K.L., *Effect of oxidation on the creep behaviour of copper-chromium in situ composite.* Composites Part a-Applied Science and Manufacturing, 2003. **34**(11): p. 1235-1244.

98. Huntz, A.M., et al., *Comparison of oxidation-growth stresses in nio film measured by deflection and calculated using creep analysis or finite-element modeling.* Oxidation of Metals, 2002. **57**(5-6): p. 499-521.

99. Seo, M., et al., *Selective oxidation of fe-30cr at low-temperatures - 743-823-k.* Oxidation of Metals, 1986. **25**(3-4): p. 164-174.

100. Wood, G.C., Hodgkies.T, and D.P. Whittle, *A comparison of scaling behaviour of pure iron-chromium and nickel-chromium alloys in oxygen.* Corrosion Science, 1966. **6**(3-4): p. 129-&.

101. Hultquist, G., M. Seo, and N. Sato, *Selective oxidation of fecr alloys in the 295-450 k temperature-range.* Oxidation of Metals, 1986. **25**(5-6): p. 363-372.

102. Cabrera, N. and N.F. Mott, *Theory of the oxidation of metals.* Reports on Progress in Physics, 1948. **12**: p. 163-184.

103. Hoshino, K. and N.L. Peterson, *Cation self-diffusion and impurity diffusion in* $fe_2o_3^+$. Journal of Physics and Chemistry of Solids, 1985. **46**(11): p. 1247-1254.

104. Swaminathan, N. and J. Qu, *Evaluation of thermomechanical properties of non-stoichiometric gadolinium doped ceria using atomistic simulations.* Modelling and Simulation in Materials Science and Engineering, 2009. **17**(4): p. 045006.

105. Dechamps, M. and F. Barbier, *Science of ceramic interfaces.* 1991, Holland: Elsevier.

106. Levich, V., *Physicochemical hydrodynamics*. 1962, Englewood Cliffs, N.J.: Prentice-Hall.

107. Garcia, E.A. and J. Kovacs, *Diffusion model for the oxidation of zirconium at 573 and 623 k.* Journal of Nuclear Materials, 1994. **210**(1-2): p. 78-83.

108. Kurokawa, H., K. Kawamura, and T. Maruyama, *Oxidation behavior of fe–16cr alloy interconnect for sofc under hydrogen potential gradient.* Solid State Ionics, 2004. **168**: p. 13-21.

109. Brylewski, T., et al., *Application of fe-16cr ferritic alloy to interconnector for a solid oxide fuel cell.* Solid State Ionics, 2001. **143**(2): p. 131-50.

110. Pragnell, W.M. and H.E. Evans, *A finite-difference model to predict 2d depletion profiles arising from high temperature oxidation of alloys.* Modelling and Simulation in Materials Science and Engineering, 2006. **14**(4): p. 733-740.

111. Kumar, S. and S.K. Kurtz, *Simulation of material microstructure using a 3d voronoi tessellation - calculation of effective thermal-expansion coefficient of polycrystalline materials.* Acta Metallurgica Et Materialia, 1994. **42**(12): p. 3917-3927.

112. Liu, Y., Y. Kageyama, and S. Murakami, *Creep fracture modeling by use of continuum damage variable based on voronoi simulation of grain boundary cavity.* International Journal of Mechanical Sciences, 1998. **40**(2-3): p. 147-158.

113. Lepinoux, J. and Y. Estrin, *Mechanical behaviour of alloys containing heterogeneously distributed particles: Modelling with delaunay triangulation.* Acta Materialia, 2000. **48**(17): p. 4337-4347.

114. Guessasma, S., *Young's modulus of 2d cellular structures under periodic boundary conditions and subject to structural effects.* Computational Materials Science, 2008. **44**(2): p. 552-565.

115. Priolo, A., et al., *Conductance of 2-dimensional disordered voronoi networks.* Physical Review B, 1992. **46**(22): p. 14889-14892.

116. Kamaya, M. and M. Itakura, *Simulation for intergranular stress corrosion cracking based on a three-dimensional polycrystalline model.* Engineering Fracture Mechanics, 2009. **76**(3): p. 386-401.

117. Fritzen, F., T. Bohlke, and E. Schnack, *Periodic three-dimensional mesh generation for crystalline aggregates based on voronoi tessellations.* Computational Mechanics, 2009. **43**(5): p. 701-713.

118. Wagner, C., *Theoretical analysis of diffusion processes determining oxidation rate of alloys.* Journal of the Electrochemical Society, 1952. **99**(10): p. 369-380.

119. Zhou, H.G., J. Qu, and M. Cherkaoui, *Stress-oxidation interaction in selective oxidation of cr-fe alloys.* Mechanics of Materials, 2010. **42**: p. 63-71.

120. Pieraggi, B. and R.A. Rapp, *Chromia scale growth in alloy oxidation and the reactive element effect.* Journal of the Electrochemical Society, 1993. **140**(10): p. 2844-2850.

121. Saito, Y., B. Onay, and T. Maruyama, *The reactive element effect (ree) in oxidation of alloys.* Journal de Physique, 1993: p. 217-230.

122. Pint, B.A., *Experimental observations in support of the dynamic-segregation theory to explain the reactive-element effect.* Oxidation of Metals, 1996. **45**(1-2): p. 1-37.

123. Zhu, L., et al., *Oxidation of a novel chromium coating with ceo2 dispersions.* Oxidation of Metals, 2004. **62**(5-6): p. 411-426.

124. Noden, J.D., C.J. Knights, and M.W. Thomas, *Growth of austenitic stainless steels oxidised in carbon and oxygen bearing gases.* British Corrosion Journal, 1968. **3**(1): p. 47-55.

125. Zhou, H.G., J. Qu, and M. Cherkaoui, *Stress-oxidation interaction in selective oxidation of cr-fe alloys.* Mechanics of Materials, 2009(In Press).

126. Kawamura, K., et al., *Diffusion-coefficient of yttrium ion in $ycro_3$.* Journal of the Electrochemical Society, 1995. **142**(9): p. 3073-3077.

127. Yamazaki, Y., et al., *Volume and grain-boundary self-diffusion in a high-purity fe-50 mass % cr alloy.* Physica Status Solidi a-Applied Research, 2002. **189**(1): p. 97-105.

128. Hammer, J.E., *The oxidation of materials for interconnects in solid oxide fuel cells*. 2002, University of Pittsburgh: Pittsburgh.

129. Horiguchi, K. and Y. Shindo, *Experimental and theoretical results for bending of a soft ferromagnetic plate in a transverse magnetic field.* Acta Mechanica, 2003. **162**(1-4): p. 185-194.

130. Delaunay, D., A.M. Huntz, and P. Lacombe, *Mechanical stresses developed in high-temperature resistant alloys during isothermal and cyclic oxidation treatments - the influence of yttrium addisions on oxide scale adherence.* Corrosion Science, 1980. **20**(10): p. 1109-1117.

131. Hutchinson, J.W. and Z. Suo, *Mixed-mode cracking in layered materials*, in *Advances in applied mechanics, vol 29*. 1992. p. 63-191.

132. Bose, K., P.A. Mataga, and P.P. Castaneda, *Stable crack growth along a brittle/ductile interface - ii. Small scale yielding solutions and interfacial toughness predictions.* International Journal of Solids and Structures, 1999. **36**(1): p. 1-34.

133. Stroosnijder, M.F., et al., *The influence of yttrium ion implantation on the oxidation behaviour of powder metallurgically produced chromium.* Surface & Coatings Technology, 1996. **83**(1-3): p. 205-211.

134. Chevalier, S., et al., *The reactive element effect on thermally grown chromia scale residual stress.* Materials Science and Engineering a-Structural Materials Properties Microstructure and Processing, 2003. **343**(1-2): p. 257-264.

135. Chevalier, S., et al., *Effects of a reactive element on isothermal and cyclic oxidation of chromia-forming alloys: Sem/edx, tem and sims investigations.* Materials at High Temperatures, 2000. **17**(2): p. 247-255.

136. Pint, B.A. and K.B. Alexander, *Grain boundary segregation of cation dopants in alpha-al_2o_3scales.* Journal of the Electrochemical Society, 1998. **145**(6): p. 1819-1829.

137. Zurek, J., et al., *Growth and adherence of chromia based surface scales on ni-base alloys in high- and low-po(2) gases.* Materials Science and Engineering a-Structural Materials Properties Microstructure and Processing,

2008. **477**(1-2): p. 259-270.

138. Chevalier, S., et al., *Segregation of neodymium in chromia grain-boundaries during high-temperature oxidation of neodymium oxide-coated chromia-forming alloys.* Oxidation of Metals, 2000. **54**(5-6): p. 527-547.

139. Czerwinski, F. and J.A. Szpunar, *Controlling grain-boundary diffusion in oxide-films by reactive element addition.* Canadian Metallurgical Quarterly, 1995. **34**(3): p. 243-249.

140. Atkinson, A., R.I. Taylor, and A.E. Hughes, *A quantitative demonstration of the grain-boundary diffusion mechanism for the oxidation of metals.* Philosophical Magazine a-Physics of Condensed Matter Structure Defects and Mechanical Properties, 1982. **45**(5): p. 823-833.

141. Park, J.H., W.E. King, and S.J. Rothman, *Cation tracer diffusion in cr_2o3 and cr_2o_3-0.09 wt-percent y_2o_3.* Journal of the American Ceramic Society, 1987. **70**(12): p. 880-885.

142. Gifkins, R.C., *Grain-boundary participation in high-temperature deformation - an historical review.* Materials Characterization, 1994. **32**(2): p. 59-77.

143. Chen, Y. and C.A. Schuh, *Geometric considerations for diffusion in polycrystalline solids.* Journal of Applied Physics, 2007. **101**(6).

144. Zhou, H.G. and M. Cherkaoui, *A finite element analysis of the reactive element effect in oxidation of chromia-forming alloys.* Philosophical Magazine, 2009. **In Press**.

145. Bennett, I.J., J.M. Kranenburg, and W.G. Sloof, *Modeling the influence of reactive elements on the work of adhesion between oxides and metal alloys.* Journal of the American Ceramic Society, 2005. **88**(8): p. 2209-2216.

146. Bennett, I.J. and W.G. Sloof, *Modelling the influence of reactive elements on the work of adhesion between a thermally grown oxide and a bond coat alloy.* Materials and Corrosion-Werkstoffe Und Korrosion, 2006. **57**(3): p. 223-229.

147. Tien, J.K. and F.S. Pettit, *Mechanism of oxide adherence on fe-25cr-4al (y or sc) alloys.* Metallurgical Transactions, 1972. **3**(6): p. 1587-1599.

148. Whittle, D.P. and J. Stringer, *Improvements in high-temperature oxidation resistance by additions of reactive elements or oxide dispersions.* Philosophical Transactions of the Royal Society of London Series a-Mathematical Physical and Engineering Sciences, 1980. **295**(1413): p. 309-329.

149. Zhou, H.G., J. Qu, and M. Cherkaoui, *Finite element analysis of oxidation induced metal depletion at oxide-metal interface.* Computational Material Science, 2009. **(Submitted)**.

150. Heimes, E., R. Hecker, and D. Stover, *Improvement of oxide layer stability by use of chemical surface attack.* Surface & Coatings Technology, 1988. **34**(3): p. 295-309.

151. Saito, Y. and B. Onay, *Improvements of scale adherence on heat-resisting alloys and coatings by rare-earth additions.* Surface & Coatings Technology, 1990. **43-4**(1-3): p. 336-346.

152. Busso, E.P., et al., *A physics-based life prediction methodology for thermal barrier coating systems.* Acta Materialia, 2007. **55**(5): p. 1491-1503.

153. Busso, E.P. and Z.Q. Qian, *A mechanistic study of microcracking in transversely isotropic ceramic-metal systems.* Acta Materialia, 2006. **54**(2): p. 325-338.

154. Karnesky, R.A., et al., *Effects of substituting rare-earth elements for scandium in a precipitation-strengthened al-0.08 at. %sc alloy.* Scripta Materialia, 2006. **55**(5): p. 437-440.

155. Karnesky, R.A., D.N. Seidman, and D.C. Dunand, *Creep of al-sc microalloys with rare-earth element additions*, in *Aluminium alloys 2006, pts 1 and 2 - research through innovation and technology*, W.J. Poole, M.A. Wells, and D.J. Lloyd, Editors. 2006. p. 1035-1040.

156. Pei, M., *Effects of lanthanum doping on the microstructure and mechanical behavior of a snag alloy*, in *Mechanical Engineering*. 2007, Georgia Institute of Technology: Atlanta.

157. Miao, P., et al., *Thermal stability of nano-structured ferritic alloy.* Journal of

Nuclear Materials, 2008. **377**(1): p. 59-64.

158. Arzt, E. and M.F. Ashby, *Threshold stresses in materials containing dispersed particles.* Scripta Metallurgica, 1982. **16**(11): p. 1285-1290.

159. Rosler, J. and E. Arzt, *The kinetics of dislocation climb over hard particles .1. Climb without attractive particle-dislocation interaction.* Acta Metallurgica, 1988. **36**(4): p. 1043-1051.

160. Meyers, M.A. and K.K. Chawla, *Mechanical metallurgy*. 1984, Dislocation mechanics of creep: Prentice-Hall, Inc.

161. Marquis, E.A. and D.C. Dunand, *Model for creep threshold stress in precipitation-strengthened alloys with coherent particles.* Scripta Materialia, 2002. **47**(8): p. 503-508.